University of Stavanger

FACULTY OF SCIENCE AND TECHNOLOGY

MASTER'S THESIS

Study programme/specialisation:	
Engineering Structures and Materials - Mechanical systems	Spring semester 2020 Open / ~~Confidential~~

Author: Magnus Strøm

Programme coordinator: Knut Erik Teigen Giljarhus

Supervisor(s): Vidar Hansen

Title of master's thesis:

Microstructural Analysis of Selective Laser Melted AlSi10Mg

Credits:

Keywords:	
Additive manufacturing Selective laser melting Aluminium Microstructure Residual stress	Number of pages: ……79…………… + supplemental material/other: ……0…… Nordfjordeid,……………………… 14.07.2020

Preface

This master thesis is submitted as partial fulfilment of the requirements of the Master of Science (MSc) degree at the University of Stavanger (UiS). The work has been carried out at the Faculty of Science and Technology (TEKNAT) in the period February - July. This thesis is considered a completion of the Engineering Structures and Materials degree with specialisation in Mechanical Systems.

I would like to thank Morten Kollerup Bak and Mechatronics Innovation Lab AS for their work and cooperation regarding the manufacturing process and the thesis definition and guidance. In addition, Biljana Pejova for her help analysing residual stresses in this thesis.

I would like to thank Wakshum Mekonnen Tucho for his commitment at the laboratory as it was limited access for students during the COVID-19 pandemic. Wakshum carried out all of the experimental work for this project. His work at the laboratories at UiS enabled this thesis to be completed.

Finally I would like to express my gratitude to my supervisor, Vidar Hansen. Vidar played a key role with his guidance and help throughout this peculiar period.

<div align="center">

Nordfjordeid, July 2020

Magnus Strøm

</div>

Microstructural Analysis of Selective Laser Melted AlSi10Mg

Magnus Strøm

Abstract

Selective laser melting (SLM) is a manufacturing method where computer models are built layer by layer using a laser as heat source to melt powder in selected areas. The method allows for creating parts that would be impossible using traditional methods, enabling for weight reduction of parts without compromising structural integrity through topology optimisation. Due to high thermal gradients and the inherent SLM process, a unique macro and microstructure are produced. SLMed AlSi10Mg was examined by microscopy, and mechanical properties were investigated. Two identical sets of parts were built using RF-PS processed powder with process parameters which gave a high value for the energy input per unit length. One of the sets were given a stress-relief heat treatment (300°C for 2h) to reduce residual stress.

The stress relief greatly affected mechanical properties and residual stresses in the specimens. This is attributed to the change in the microstructure as the heat treatment dissolves the fibrous Si network. The hardness was found to be a function of building height for the as-printed vertically printed specimen. Despite the high laser power used during production, no signs of evaporation were found. The results from this study showed that the process parameters used are deemed sufficient as there were low porosity, sufficient overlap between melt pools, acceptable residual stresses and satisfactory results from mechanical testing. The recommended value range for energy input per unit length reported in the literature can hence be questioned.

Contents

List of Figures

List of Tables

Acronyms

AM Additive manufacturing.

CAD Computer-aided design.

EBM Electron beam melting.

EBSD Electron backscatter diffraction.

EDS Energy dispersive X-ray spectroscopy.

FFF fused filament fabrication.

GP Guinier-Preston zones.

HAZ Heat-affected zone.

HW Halder-Wagner.

PBF Powder bed fusion.

QBSD Back-scattered detector.

RF-PS radio frequency plasma spheroidisation.

SEM Scanning electron microscopy.

SLM Selective laser melting.

SSSS Supersaturated solid solution.

STL Stereolithography.

TEM Transmission electron microscopy.

WH Williamson-Hall.

1 Introduction

Additive manufacturing (AM) has evolved from being limited to rapid prototyping and non-bearing components to building commercially viable components used in the aerospace, automotive and medical industry. [1, p. 3][2]. The development and commercialisation of technology are partly because of the demand for high-strength and light-weight parts by the mentioned industries. However, due to micro-cracking issues, the use of AM parts still is limited. [3] On-site production of critical parts is also possible with AM which can reduce lead time and contribute to lessening the need for physical inventory which can be costly and is in accordance with Lean Manufacturing method that many companies have adopted.

Simulation-based design and topology optimisation can reduce the weight of parts without compromising structural integrity and thus help reduce the energy needed to propel vehicles, for example. The Powder bed fusion (PBF) technique allows for recycling of the unmelted metal powder. It can be used several times with only the work needed to prepare for re-use is sieving. [4]

There is a large selection of AM methods using different layer deposition technique and materials. Selective laser melting (SLM) is a powder bed fusion additive manufacturing method where a metallic powder layer is melted by laser to create parts. SLM allows for unprecedented geometric freedom that expands the horizon of companies that require high strength to weight ratio parts. Such parts can even have internal cavities if desired. Also, this manufacturing technique builds parts near net-weight, which reduces the post-processing needed and waste.

On the other hand, the building of the part itself from SLM is a time-consuming process and can be expensive. Although AM can have these undesired characteristics, the total cost can be reduced despite high manufacturing cost. Looking at the medical industry where corrective surgeries and post-surgery rehabilitation significantly increase the total cost of treatment, individually custom-made implants or prostheses can reduce the need for such treatments. Also, auxiliary tooling and practice models help staff enhance their understanding of a situation. [5][6] This is just one area AM can disrupt what thought of as normal procedures.

Aluminium is the most abundant metals on the surface of the Earth and one of the most important export commodities for Norway. Pure aluminium itself is not considered a strong metal, but by adding a small percentage of an alloying element, the strength can be increased tenfold. The alloying elements may also allow for precipitation hardening. Combined with its high conductivity, excellent corrosion resistance and its potential for recycling make it a material with properties for good longevity.

Compared to subtractive methods (e.g. milling, turning), AM does not use more material than is absolutely necessary (disregarding support structures/heat sinks). This reduces waste during the production in two ways: (1) when using subtractive methods, the workpiece dimension has to be at least as large as the dimension of the finished product. The

excess material of the workpiece is going to waste during manufacturing. (2) The energy and time used for removing this excess material is also a waste. AM usually can avoid these two unnecessary steps.

However, AM has drawbacks that can not be neglected. The high production cost may not be so surprising due to the techniques being relatively new, but it is expected that the cost will be reduced as the technique matures. The slow manufacturing process and difficulty to scale production is a downside of AM. Larger series can in most cases be made significantly faster with casting and sometimes also subtractive methods. The material also needs to be suited for the manufacturing method. This limits the material choices for AM. When deciding what manufacturing method is to be used for the production of a component, many parameters have to be considered, and even several manufacturing techniques may be viable.

Processing aluminium using SLM is difficult because of the high laser reflectivity, and low laser absorptivity of aluminium make it so that a large amount of energy is required to melt the metal powder completely. [7] The unmelted powder can cause pores in the part which consequently reduces density. [8] Because of this, a process parameters in the SLM process are crucial to ensure complete powder melting. The inherently low weight of aluminium causes difficulties dispersing the powder evenly on the bed.

Extensive studies have been done on the mechanical properties of SLMed AlSi10Mg. [9][10][11][12][13][14] In this study hardness measurements will be performed to investigate mechanical properties as there is a correlation between hardness and yield strength of a material. [15][16] Tensile testing is expensive and is destructive. The hardness tests are therefore considered as an inexpensive alternative method for measuring yield strength.

Residual stresses have not been receiving the same attention as mechanical properties, but there have been studies on residual stress in SLMed AlSi10Mg [2][17][18] and on other alloys in SLM [19][20]. Residual stresses are found in SLM parts because of the high temperature gradients and repeated heating and cooling cycles.

The most common heat treatments for the AlSi10Mg alloy is precipitation hardening and stress relief. [12][21] Precipitating meta-stable phases strengthens and increases the hardness of the material. [14][22] Studies have also been done on how the building direction affects the mechanical properties. [21][22] Due to the fine cellular microstructure of AlSi10Mg parts built by SLM they have higher as-built tensile strength compared to cast AlSi10Mg. [9][14][23]

Objectives of the thesis
This thesis investigates two twin sets of SLM built AlSi10Mg specimens. One set is to be heat treated, and one set is to be investigated in its as-printed state. The AlSi10Mg powder provided by TEKNA was processed by radio frequency plasma spheroidisation. It is desirable to examine the microstructure before and after heat treatment and the effect the heat treatment has on residual stress and mechanical properties. The specimens are also built in different direction to see how the building direction also affects the above mentioned characteristics.

The thesis is a cooperation between the University of Stavanger and Mechatronics Innovation Lab AS in Grimstad. Material powder and fabrication into specimens is a result of the work from Mechatronics Innovation Lab AS.

The specimens are to be examined by optical microscopy, scanning electron microscopy, transmission electron microscopy, Vickers hardness testing, EDS and X-ray diffraction.

Four research questions have been developed:

i. How does heat treatment affect the microstructure and consequently mechanical properties?

ii. How is the chemical composition of the powder compared to the printed specimens? Has there been any evaporation? How is the chemical composition of the different areas in the specimen?

iii. Can the repeatedly heating when building with selective laser melting cause formations of precipitates or alloying clusters? Is it possible that some of the alloying elements go into solution from the repeated heat cycles?

iv. How are the residual stresses before and after heat treatment?

The aim is that the results from the experimental work will extend the knowledge of selective laser melting of the AlSi10Mg alloy for Mechatronics Innovation Lab AS.

2 Theory

2.1 Selective laser melting

SLM is an additive manufacturing method based on powder bed fusion technology. A part set to be manufactured by additive methods are usually designed with a Computer-aided design (CAD) software and converted into a Stereolithography (STL) file. The STL is then sliced in layers (cross-sections) with equal height. For SLM, a layer of metal powder is then spread evenly across a pre-heated platform, and a laser selectively scans the desired areas to melt the powder. The irradiated powder is melted by the energy provided by the laser and later solidifies and fuses layers together. It is important that the laser exposure is sufficient, so it penetrates slightly into the previous layer allowing complete fusion. Complete fusion of layers reduces directional properties as one can see in fused filament fabrication (FFF) technology. [1, p. 21] The platform is then lowered by the height of one layer, and a new layer of powder is replenished. These steps are repeated until the part is completed. Powder not affected by heat can be sieved and recycled. This reduces material waste during production. Subtractive methods (e.g. milling and turning) subtracts material to make parts which produce chips (i.e. waste). This waste can be recycled, but it is more demanding compared to sieving powder from an SLM process because it needs to be processed.

Powder particle size used for SLM usually is the range of 15 to 70 μm. AlSi10Mg powder normally consists of 20 - 63 μm particles. [24] Aluminium powders have poor flowability due to low weight which makes it challenging to spread powder evenly across the build platform. [25] Layer thickness varies between 30 μm and 60 μm.

An SLM process is performed in a chemically controlled atmosphere to reduce the formation of oxides during melting and solidification. Other powder bed fusion techniques, e.g. Electron beam melting (EBM) require good vacuum in the order of 10^{-3} Pa to achieve high quality using a different thermal source. [3] The vacuum reduces the chance of oxides in the specimen significantly as the highest quality argon gas still contain more oxygen compared to vacuum. However, SLM is far less affected by the atmosphere since it uses photons and not electrons. Therefore, the SLM can get away with filling the chamber with a chemically inert gas which is less expensive than creating a vacuum. [26]

2.1.1 Scanning strategy

There are many different scanning strategies for SLM. The main goal of these strategies is to increase density and reduce anisotropy. The direction of scan tracks can either be unidirectional or bidirectional, meaning the scan tracks only move in the positive x-direction or both positive and negative x-direction, respectively, as illustrated in Fig. 1A and B. Island-shift is a scanning strategy where the cross-section is divided into smaller areas ($\sim$25 mm^2). This is illustrated in Fig. 1 D. These areas help reduce the vector length [27]. For each layer, these

islands are moved a small amount transversely in both x and y-direction (Fig. 1 E). The shift is done to ensure that no two layers are identical (prevent pattern repetition). The scanning direction is rotated for each layer. Such rotation is illustrated in Fig. 1 E. This figure shows a 90° rotation for each layer, but this is not suitable for a cubic system like aluminium. A 67° is a patented layer rotation standard given by PBF machine manufacturer EOS. 67 is a prime number which makes the pattern repetition so rare that it is expected to be negligible.
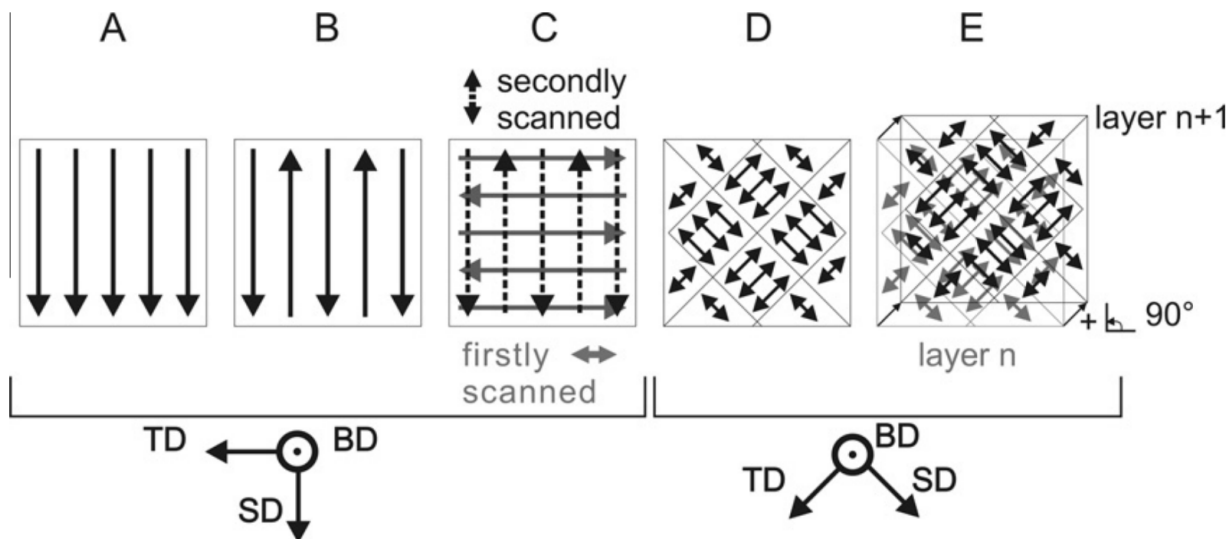
Figure 1: Scanning strategies for SLM. The transverse (TD), scanning (SD) and building direction (BD) are indicated. A is unidirectional. B is bidirectional. C shows bidirectional scans in both x and y direction. D illustrates dividing areas into islands. E illustrates rotation and island-shift between layers. [27]

Due to aluminium's high thermal conductivity, partially melted powder particles will adhere to the surface of the part, which affects the surface roughness. Therefore, it is generally preferred to scan the volume first, then the borders to achieve a smoother surface finish. This prioritisation allows the heat from scanning the border to dissipate into the already solidified volume, reducing the partially melted powder particles adhered to the surface.

2.1.2 Selective laser melting of aluminium

Every machine producing SLM parts have different settings parameters for the different materials, meaning that knowledge gained from applying parameter changes in one machine will not necessarily be transferable to a machine made by another manufacturer. For example, the amount of energy delivered to the material is dependent on the spot size. An SLM machine using 100 W laser with a 25 μm spot size will not deliver the same energy as a machine using the same power with a larger spot size. Tab. 1 shows the different machine parameters needed for making parts with the highest relative density for each machine and material used.

Machine used	Investigated range				Optimised values				Energy density	Relative
	P (W)	v (mm/s)	h (mm)	t (mm)	P (W)	v (mm/s)	h (mm)	t (mm)	(J/mm^3)	density (%)
Realizer SLM-50	100	250-1000	0.05-0.25	0.04	100	500	0.050	0.04	100	99.8
Concept Laser M2	100-200	700-2000	0.075-0.12	0.05	175	1025	0.098	0.05	34	99.7
Concept Laser M1	-	-	-	-	200	1400	0.105	0.03	45	99.4
Reinshaw AM250	-	-	-	-	200	570	0.130	0.03	108	99.9
Trumpf TrumForm LF130	-	-	-	-	250	500	0.150	0.05	67	>99
SLM-250 HL	-	-	-	-	350	1140	0.170	0.05	36	N/A

Table 1: Overview of studies on different machines in which process parameters optimised for SLM of the AlSi10Mg alloy. P is laser power, v is scan speed, h is hatch spacing, and t is layer thickness. The (-) means that a parametric study was not presented. Table adapted from Aboulkhair et al. [3]

Using aluminium alloys in an SLM process can cause some problems due to material properties. Aluminium has high reflectivity and high thermal conductivity, causing it to be hard to process in an SLM manufacturing environment. However, a small solidification range due to the near-eutectic composition makes AlSi10Mg one of the easier aluminium alloys to use for SLM processes.

Pre-alloyed aluminium powder contains alloying elements that are added to enhance the mechanical properties of the already light-weight and corrosion resistance aluminium. The most common elements added to an aluminium mixture are magnesium, zinc, silicon, manganese and copper. Adding magnesium to an Al-Si alloy allows for strength increasing precipitates to occur given the proper thermal stimulation. [23] In the aerospace industry aluminium alloys have had a profound effect due to its light-weight and strength. [28] However, light elements such as magnesium and aluminium can evaporate causing pores and consequently reduce density if the boiling point is exceeded. [3]

An evaluation of single scan tracks of SLM AlSi10Mg by K. Kempen et al. manifested that the laser energy per unit length E' (J mm^{-1}) could be defined as: [7]

$$E' = \frac{E}{L} = \frac{P}{v} \tag{1}$$

where E is laser energy (J), L is scan track length (mm), P is laser power (W), v is the scan speed (mm s^{-1})

Melt pool volume increases and viscosity decreases when E' is too high. E' is controlled by the laser power and the scan speed, as shown by Eq. 1. When E' is too low, the melt pool is distorted, and may result in an insufficient connection to the anterior layers.

Increasing scanning speed causes the molten pool width to decrease and its length to increase. A smaller circumference-to-length ratio of the molten pool is related to a more unstable behaviour. [29]

When E$'$ is too high the laser melting transitions from conduction mode to keyhole mode, i.e. the laser transmits a sufficient amount of energy to vaporise the melt pool. Conduction and keyhole mode can be seen in Fig. 2. Penetrating vapour cavities form deep inside the melt pool and if unstable these can collapse, leaving small pores at the bottom om the melt pool — these pores reduce density. [7]
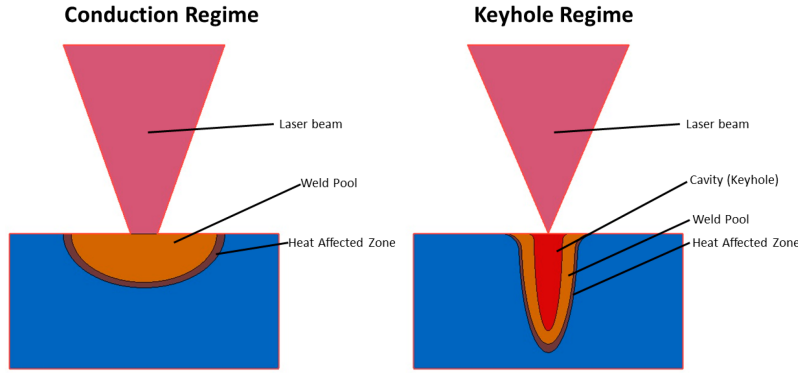
Figure 2: Conduction and keyhole mode laser welding. [30]

The optimal density for AlSi10Mg was achieved by having an energy input per unit length in the range of 140 – 160 J m^{-1} to keep the melt pool stable. [7] When E$'$ was very high or low, the density was reported to be inadequate. For a high laser power, high laser speed is needed and vice versa. It is worth noting from a manufacturing point of view that if maximum capacity is to be utilised, high laser power and speed is to be used.

There are four main parameters for the melt pool to ensure a sufficient connection between layers. [7]

(i.) Uninterrupted scan tracks prevent pores and irregularities. The areas surrounding the start and end of the scan track will experience a different heat dissipation compared to the middle part of the scan track. The difference in heat is by areas in prior the start point and anterior the endpoint are cooler since the laser has not travelled over these areas. Therefore, pores and irregularities can occur at the start and end of the scan track due to incomplete melting of powder.

(ii.) The laser is required to output sufficient E$'$ to penetrate slightly into the underlying layer to ensure that there is a well-established bonding between layers. Fig. 3 illustrates a single scan track on top of a complete layer. The single scan track has a circular shape with the bottom part penetrating into the previous layer.

(iii.) The height of the scan track in relation to the previous layer must be at least half of the track width in order to build robust parts. When the height is too low, the resulting surface will be uneven and have a wave-like appearance, but this can be compensated by compressing the track overlaps.

(iv.) High density and accuracy are obtained by having a connection angle (see Fig. 3) between the scan track and the previous layer close to 90°. If the connection angle is higher than 90°, the adjacent tracks must have a larger overlap to compensate for the reduction in height.
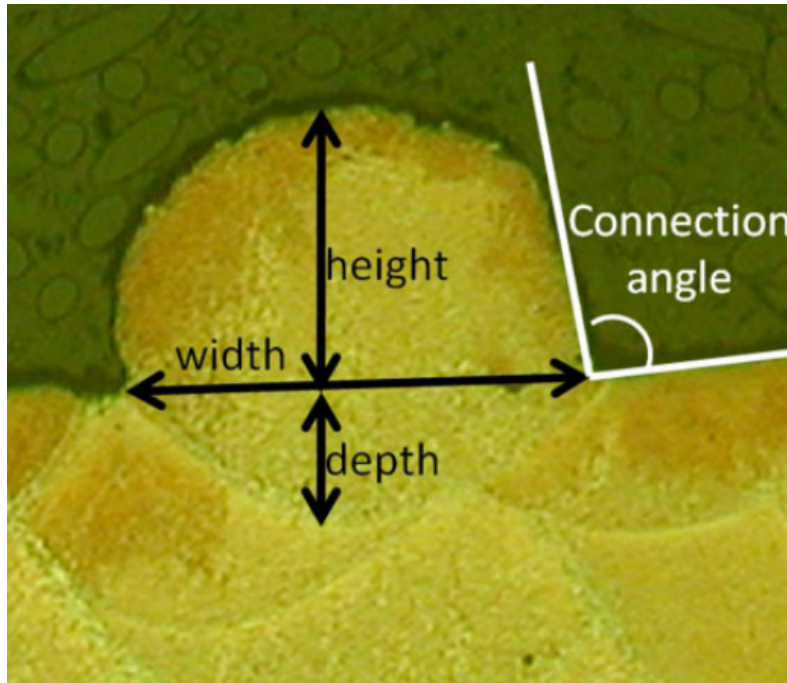
Figure 3: Single scan track on a multi-track layer. [7]

Insufficiently melted powder at the melt pool boundaries causes pores of irregular shapes and poor overlap connection between scan tracks. Oxides can also be formed in these areas. [25] At these melt pool boundaries, the solidification time is longer leading to a coarser microstructure compared to the centre of the melt pool.

A thin oxide film may arise on the scan tracks when SLM aluminium. If the laser power is not sufficient to completely melt these oxides, such films meet and they can form a pore which decreases the density. Such pore formation can be seen in Fig. 4 and need to be avoided to manufacture high-density parts. [25]
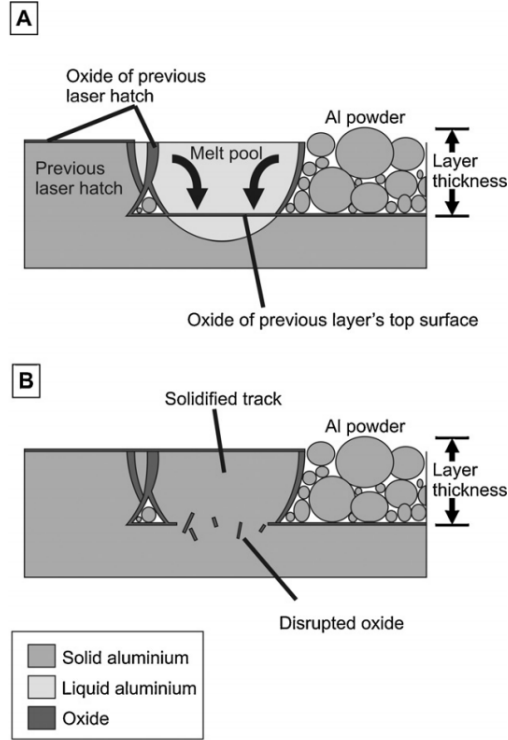
Figure 4: Formation of oxides in PBF. [25]

2.1.3 Microstructure of SLMed AlSi10Mg

The microstructure of as-printed SLM Al-Si alloys have a fine cellular-dendritic characteristic due to the high thermal conductivity of aluminium which causes a rapid cooling. [27][13][10] The centre of the solidified melt pool has smaller equiaxed grains compared to the grains at the melt pool boundary. At the boundary, the grains have a more irregular shape, and are coarser. [8] The outer region retains an elevated temperature which makes the solidification more time-consuming. They experience this elevated temperature because the outer region of the melt pools are more affected by the repetitive thermal cycles by the laser when it is passing by for melting the adjacent tracks.

The nature of the SLM process with repeated thermal cycles from laser scanning makes the melt pool have directional cooling and rapid solidification, which affects the final microstructure of the part and consequently the mechanical properties. [13] The fibrous Si network gives the SLMed AlSi10Mg alloy its good as-built hardness characteristic. AlSi10Mg built from SLM can have approximately 30% higher Vickers hardness than high pressure die casted (HPDC) AlSi10Mg. [27]

The melt pool growth rate (R, m/s) and thermal gradient (G, K/m) decide the solidification structure. The mode of solidification (in other words: if the solidification is cellular, columnar dendritic, and equiaxed dendritic) is determined by the ratio G/R. The size of the solidification structure is dictated by the product of G and R. [31, p. 165] A finer cellular or

dendritic structure is attained by shorter solidification time, i.e. a higher cooling rate. [31, p. 163] The relationship between the temperature gradient G and the growth rate R is summarised in Fig. 5.
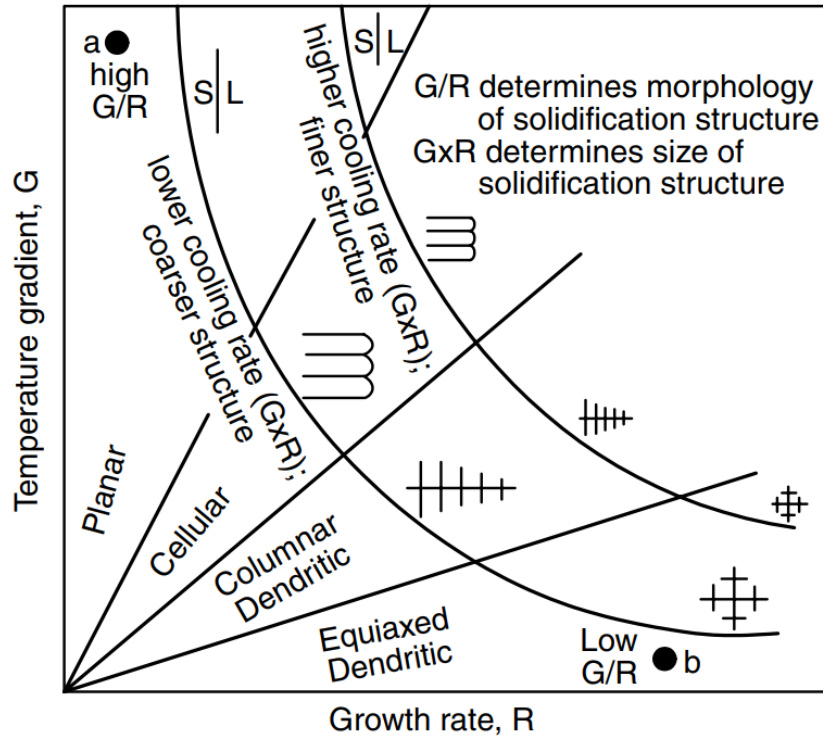
Figure 5: Temperature gradient and growth rate. [31, p. 166]

In a study performed by Rosenthal et al. in the ALSi10Mg SLM built parts (with stress relief heat treatment at 300°C for 2h) a variations in the grain size were observed, but solidification structure was unchanged in the sample. Meaning that the ratio G/R was close to constant, but the product of G and R was altered. [13]

The study by Rosenthal et al. also showed that samples built in the horizontal direction had a higher elongation at ultimate tensile strength. [13] Failures from the vertical built samples manifested mainly as ductile with a dimple structure. The failure originates from weak interlayer connection. The difference in the fracture surface of the horizontally built and vertically built were dissimilar. This indicates that there is anisotropy in parts built by SLM. The horizontally built samples had intralayer failure which lead to higher values for elongation. [13]

The build direction, either it be horizontal, vertical or at 45 degrees, does not matter for the microstructure after T6 heat treatment. [22] This is because after the microstructure is homogenised, the dendrites, laser traces and Heat-affected zone (HAZ) are dissolved.

At the end edges of scan tracks, heat can accumulate if the laser is direction is bidirectional due to the laser passing through the same area in a very short period of time. Keyhole mode welding occurs in these areas causing pores. [27] Outside the melt pool, Si has an increased diffusion rate in the heat-affected zones. This causes the microstructure to have the characteristic cellular-dendritic structure.

Long scanning vectors in the same direction for every layer (no rotation) gives a strong (100) texture along the direction of the scan. A weaker (110) texture can also occur along the same direction. [27]

Larger oxide particles are also to be expected in SLM aluminium parts, consequently reducing density. Despite the SLM process is carried out in a chemically inert atmosphere (usually argon gas) there can still be some trace amounts of oxygen. This is enough to make such oxide particles in the part. The laser power should be high enough to break through the oxide film on top of each layer to avoid the presence of oxides. Executing the SLM process with a high energy (>150 W) laser ensures the absence of oxides and results in a part with high density. [27]

2.1.4 AlSi10Mg powder

In an SLM manufacturing process, input material properties with adequate powder specification are paramount to be certain that printed components have the desired properties. Metallurgical powder is suited for additive manufacturing if they are spherical, dense, free from satellites (smaller particles attached to larger particles), high flowability and high packing density. These properties can be obtained by utilizing radio frequency plasma spheroidisation (RF-PS).

Spheroidisation of particles improves flowability, which is the ability of loose particles to move by flow. The powder packing density is increased due to the spherical shape of the particles. The powder morphology determines how well the powder will be deposited in uniform layers. Spheroidisation eliminates internal cavities and fractures that the particle might have and changes the internal surface morphology. Powder purity is also enhanced. [32]

Utilizing RF-PS technology allows for creating metallurgical powder with near-perfect spherical shape. Such an apparatus to using RF-PS consists of a plasma torch, a cooled chamber and a collector for powder. Firstly a stable plasma is generated using argon as sheath and centre gas. [33] Particles are then carried through the plasma where they melt and form droplets. 30 to 60 grams of feedstock is fed into the plasma region per minute with a reactor pressure of 100 kPa (atmospheric pressure). Liquid particles condensate and take a spherical form when re-solidifying. [34]

Different powder producers will give different powder characteristics, e.g. irregular particles, elongated particles, and particles with satellites. These differences greatly affect the density of the built part. Aboulkhair et al. [35] demonstrated that two different powders

from different producers yielded different densities using the same parameters for both powders. The difference in measured density was quite significant, which exhibit the importance of powder. Pre-sintering can improve the density to the point where parts built with powder from different manufacturers are indistinguishable. [35]

Powder bed fusion technique can limit the waste from manufacturing. Sieving and reusing un-melted powder can yield over 95 % recycling efficiency according to Ardila et al. for the IN718 alloy. [4] The powder properties do not change much after reusing up to 14 times. Morphology, i.e. sphericity, defects, and satellites, was almost unchanged. The particle size distribution was close to unchanged, but there were some particle lumping. O'Leary et al. also reported an increase in particle size after repeated recycling. [36] This indicates that there might be a limit for how many times powder can be recycled without affecting the quality of the produced part. However, there are concerns that oxides form during recycling processes. Ardila et al. reported an unchanged material composition, but further investigation is needed to validate these results. [4]

After an SLM process, the leftover powder is collected and sieved to filtrate unsuited particles. During the transferring and sieving process, the powder is exposed to air, and thus the possibility of oxides forming is substantially increased. There are two types of powder that can be retrieved from the leftover powder: heat-affected powder which has been either partially melted or heated and "non-affected powder" which has not been thermally affected. The latter is acceptable for recycling by sieving. The microstructure of fresh and sieved powder is illustrated in Fig. 6.
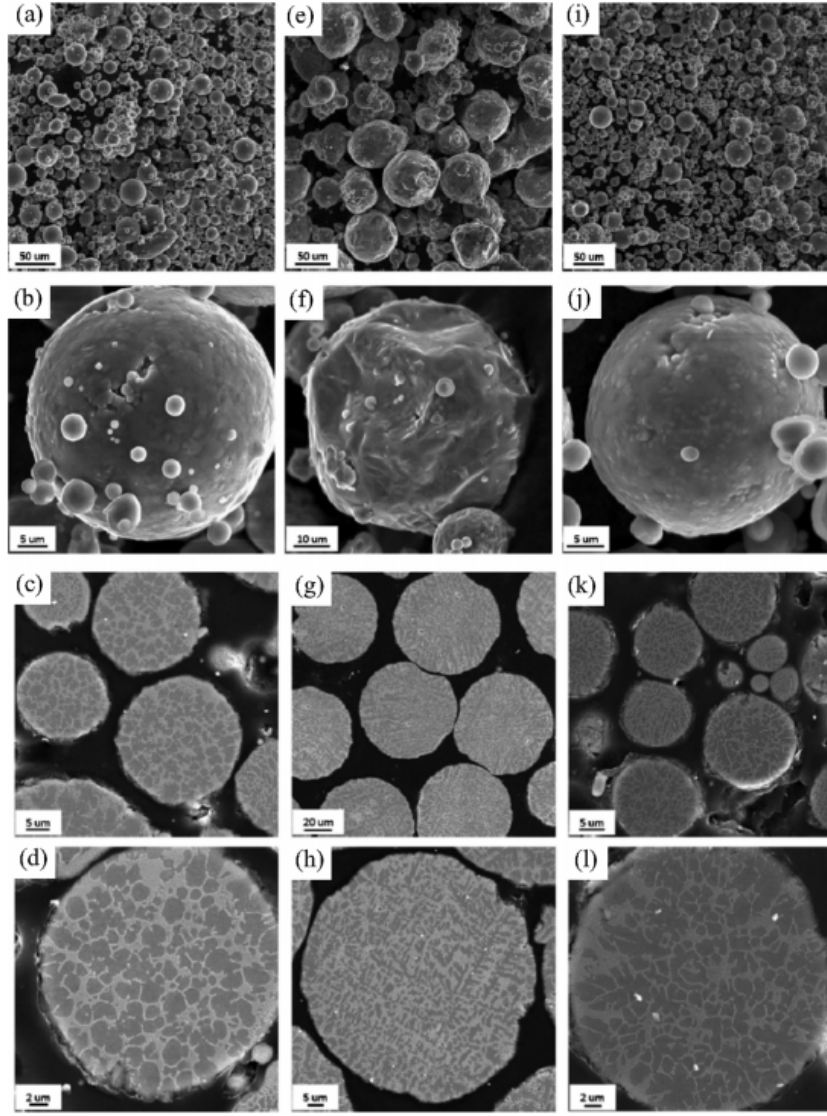
Figure 6: Morphology and microstructure of fresh AlSi10Mg powder (a-d), laser spatter (e-h) and recycled AlSi10Mg powder (i-l). [3]

2.2 Aluminium

Norway is one of the largest producers of primary aluminium in the world trailing other nations like Russia, China, India, Canada, Australia and the United Arab Emirates. [37] Aluminium is one of the most important export commodities for Norway, and up to 90% of produced aluminium is exported. [38] While developing the first aircraft, the Wright brothers used aluminium for their crankcase. The aluminium made the engine unmatched in power to weight ratio which was crucial for making the engine light enough and with sufficient power to generate lift.

Primary aluminium is made from refining bauxite, a sedimentary rock abundant in tropi-

cal and subtropical regions, such as Guinea, Australia and Brazil. [37] Aluminium refinement is a tremendously energy-consuming process where an estimated 20 - 40 % of the cost of aluminium comes from electric power. [39] In the United States, about 5% of the total electricity generated is used for producing aluminium. [40] The high cost of producing primary aluminium promotes recycling. It only takes 5% of the energy to make primary aluminium to recycle it, and about 75% of all aluminium ever produced is still in use today. Aluminium's recycling capability makes it a provident material in an economic and climate perspective.

Face-centred cubic metals like aluminium have a high toughness at low temperatures and are formable and ductile. [41, p. 12] Pure aluminium itself is not very strong (roughly 7-11 MPa yield strength) but alloying in a small percentage of other elements a yield strength above 600 MPa can be achieved. [42] These alloying elements give aluminium the opportunity of heat treatment. Precipitation hardening is the most effective method for increasing material strength in aluminium alloys. [28, p. 70] There are two requirements for the alloying elements:

i. The solubility of the alloying element in solid state must be a positive function of temperature. In other words, the solubility in solid state must be higher at elevated temperatures.

ii. When heat treating, the precipitates need to fully or partially cohere to the aluminium matrix. The precipitate gives little effect if there is no relationship with the crystal structure of the surrounding matrix. [40]

One of the challenges producing aluminium parts with SLM is the difference in the melting point of alloying elements. Some elements have a melting point above 2000 °C, which is relatively high compared to aluminium (660 °C) and magnesium (650 °C). The difference in melting point can make the ones with low melting point temperature evaporate and consequently lead to low density due to pores. The chemical final composition of the built part will also be different from the composition of the powder if evaporation takes place. [3]

2.2.1 Strengthening mechanism

There are five mechanisms for strengthening aluminium alloys: grain size control, solid solution alloying, second phase formation, strain hardening and precipitation or age hardening. [41, p. 10]

Non-heat treatable alloys get their strength through stresses residing after strain hardening. For such alloys, the hardness and strength increase with increased cold work, but the ductility is decreased. This is due to the dislocations that arise within the material. For heat treatable alloys, the strength comes from the formation of coherent precipitates. An alloy is heat treatable if the alloys consist of one phase at elevated temperatures and several

phases at room temperature.

These heat treatable alloys are noted by TX. The T meaning thermally treated to produce stable tempers and X is a digit that indicates which type of treatment the alloys has been put through. For cast or extruded aluminium parts in the 6000-series a strength increase is achieved by what is called a T6 heat treatment. The T6 heat treatment consists of solution heat treating and a precipitation heat treating called artificial ageing.

According to Hall-Petch the relationship between the yield strength and the grain size can be expressed as:

$$\sigma_y = \sigma_o + kd^{-1/2} \tag{2}$$

Where σ_y is the yield strength; σ_O is the friction stress and is a value given from where the slope intercepts on the stress axis. This describes the stress needed in a single crystal without grain boundary to move dislocations. k is an also material constant representing the slope of the graph on the yield stress plotted against the grain size. d is the average diameter of the grains. This relationship between stress and diameter size is used to calculated the required grain size to obtain a given strength. However, this method is only applicable for metals with a grain size between 1 mm and 1 μm. [28, pp. 77-78]

2.3 Defects in aluminium alloys fabricated by SLM

2.3.1 Porosity

Porosity is one of the more regular defects seen in parts made by SLM, no matter what material is studied. [3] Pores can be caused by entrapped gas that is absorbed by the melt pool, later when the melt pool is solidifying the solubility of the element decreases thus are diffused out of solution. Incomplete melting of powder can also leave a pore in the part which reduces the density. In aluminium, this is a common issue because Al has a high laser reflectivity and low laser absorptivity, which makes it challenging to melt the powder completely. Aluminium is also susceptible to oxidation which causes porosity.

Pores can be categorized in two ways for aluminium parts built by SLM: metallurgical pores and keyhole pores. Both are heavily dependent on scanning speed. [8] Metallurgical pores are most prominent at lower scanning speeds, and at high scanning speeds (>500 mm/s) keyhole pores are formed, as illustrated in Fig. 7. [8] Metallurgical pores, also known as hydrogen pores, are small (<100 micrometres) and are spherically shaped. Hydrogen pores forms at low scanning speeds caused by hydrogen in either the chamber or the powder. The hydrogen can originate from moisture in the chamber or hydrogen gas entrapped in the powder. The solubility of hydrogen in liquid aluminium is at least 22 times higher than in the solid phase. [43] This means that when the aluminium solidifies, the hydrogen has to

diffuse out of the aluminium if the hydrogen content is greater than the hydrogen solubility in the solid phase. [44]

Keyhole pores are irregularly shaped and are larger size (>100 micrometres) compared to metallurgical pores and can span across several layers. Keyhole pores are parameter-dependent and can form when there are incomplete powder melting and incomplete filling in the melt pool. Incomplete powder melting can occur at higher scanning speeds causing a phenomenon called balling. [8] At high scan speeds, the melt pool may become unstable, causing liquid droplets to be splashed out of the melt pool resulting in irregularities on the powder bed surface. Subsequent layers can be uneven as a result of balling due to poor dispersion of powder and inhomogeneity. The microstructure surrounding a keyhole pore is different compared to the adjacent microstructure. This difference in microstructure arises from the thermal conductivity being lower due to the pore being filled with gas and not solid material. Unmelted powder in pores are often challenging to detect in microscopy since the sample preparation will most likely remove unmelted particles during etching and polishing.
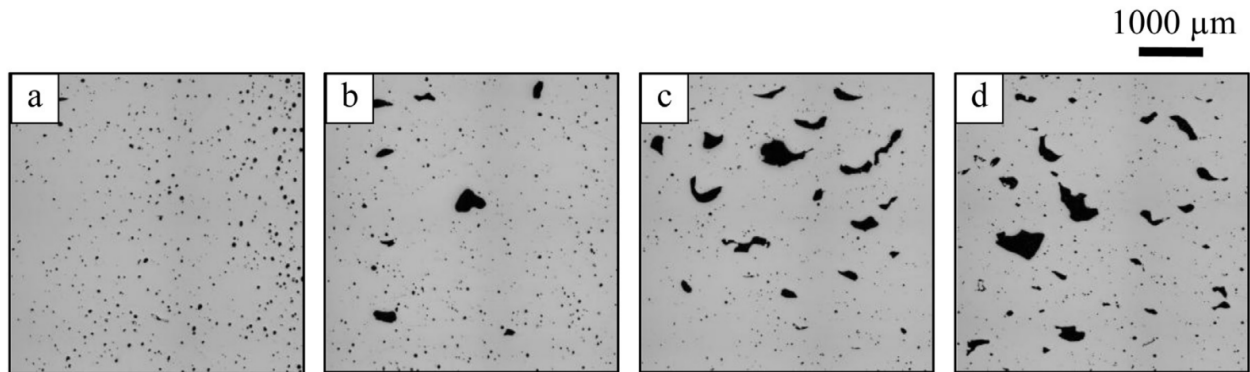
Figure 7: Formation of pores at different scanning speeds: (a) 250 mm/s, (b) 500 mm/s, (c) 750 mm/s, and (d) 1000 mm/s. Work done by Aboulkhair et al. [8]

Gaps between adjacent scan tracks can occur when the hatch spacing it to wide in relation to the spot size. [8] Thus the density is decreased if there is an insufficient overlap of scan tracks, and the intralayer bonding is reduced. An increased hatch spacing would decrease building time, but it would require a smaller layer thickness to ensure proper connection between the intralayer and the interlayer. The optimal hatch spacing values vary with the other parameters, but a value 0.7 of the spot size is satisfactory in most cases. [8] Hatch spacing can also be larger than the spot size for some materials. This is viable when the heat dissipation is sufficiently high to generate a larger melt pool than the spot size.

Porosity can be reduced by using appropriate scanning strategies. There are many strategies, for example, the double scan strategies (twice in the same direction (2X), scanning once in x-direction and once in y-direction with different hatch spacing for each scan (XY 2HS), scanning once at half power followed by one scan at full power (pre-sinter) and scanning once scan across the area with a second scan in-between adjacent scan tracks (overlap). The resulting pore formation at different speeds can be seen in Fig. 8. It is possible to eliminate

all keyhole pores at a scanning speed equal to 500 m/s using the pre-sintering scan strategy. As a consequence of the substantial use of laser energy caused by such a strategy, the formation of metallurgical pores to increased. [8] It is suggested to use smaller hatch spacing, creating layers that are homogeneous and continuous due to slower cooling.

Figure 8: Scanning strategies and resulting pores. [8]

2.3.2 Other defects in SLM

SLM parts are subjected to large amounts of residual stresses coming from fast cooling rates that occur during the SLM pr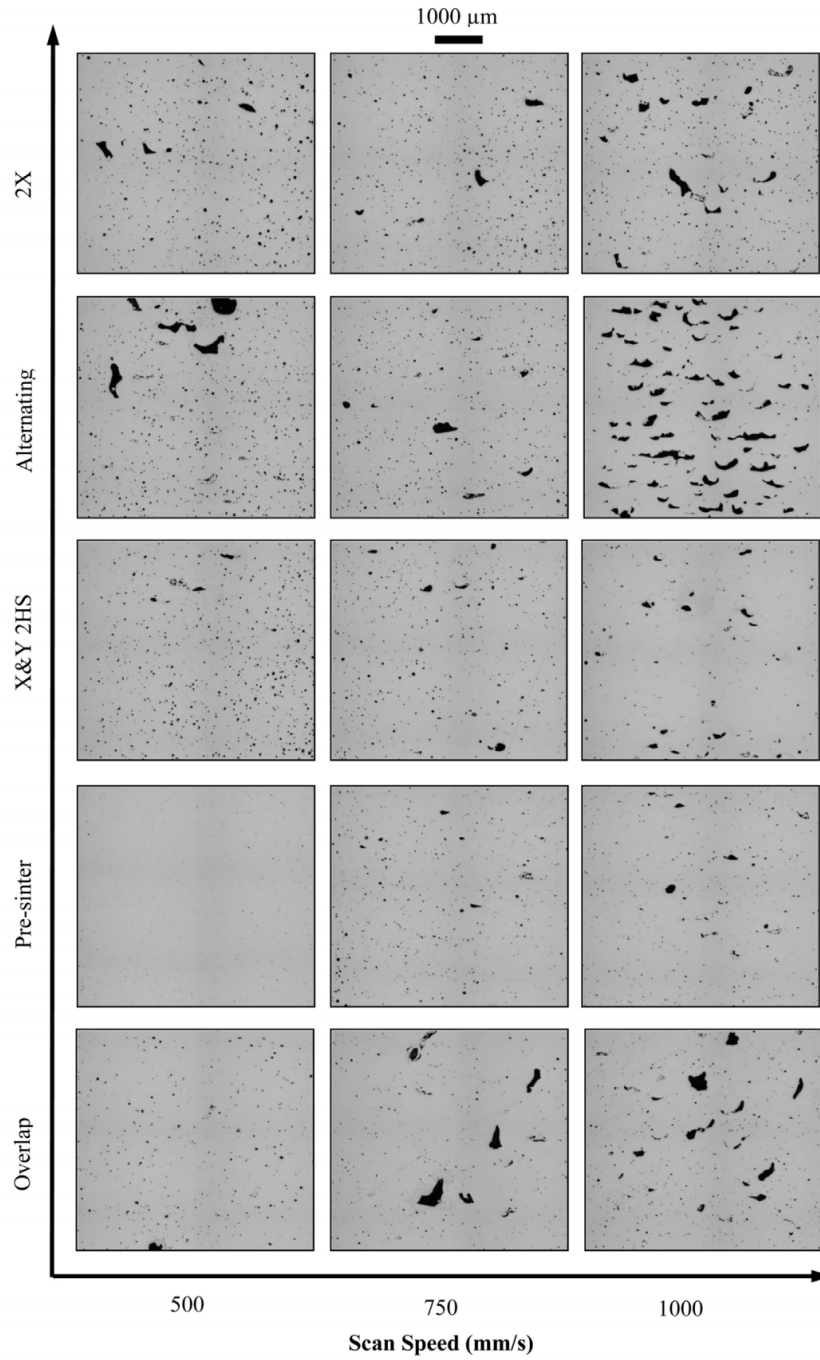ocess. Distortion can occur during removal of the SLM part from the build-plate or during processing which will lead to the build failing. A form of distortion called flaking can happen if there is insufficient bonding between layers, the substrate, or the support structure. The insufficiently bonded layer will start to peel. Park et al. exhibited an increased probability of flaking if the substrate was another material than what the powder was when avoiding using support structures by using replaceable substrates. [45] Heating the substrate can significantly reduce or completely eliminate distortions for aluminium components. [46]

Laser spatter are small droplets of molten metal that are ejected from the melt pool. Such droplets may occur at high laser power and low scanning speeds, and oxidise while airborne and are classified as defects if they land somewhere on the powder bed that is to be used for fabrication. Such spatter have a rougher surface and can be larger than fresh AlSi10Mg powder, and is illustrated in Fig. 6 (e-h). Such inclusions can contaminate the part by being trapped and be difficult to re-melt when processing subsequent layers.

Cracking can occur in aluminium parts built by SLM due to the rapid solidification rate, and pores can act like a notch making the material susceptible to cracking. [47][48]

2.4 Hardness

Hardness is the capability of a material to resist localised plastic deformation. [49, p. 174] Hardness measurements can give an indication of a material's deformation behaviour with inexpensive and non-destructive. [50, p. 292] Hardness testing can be divided into three distinct methods: (1) scratch hardness, (2) indentation hardness and (3) rebound hardness. Scratch hardness is often done on glass material to decide the grade of quality of, e.g. a smartphone screen. Rebound hardness is performed on elastomeric by measuring the bounce of a known object (hammer or ball) from a fixed height onto the material. However, for this study, the indentation hardness is of interest.

Indentation hardness tests are carried out by indenting the surface of a metal by applying a force to an indenter for a given time period which leaves an imprint in the surface. The geometry of the indentation is measured, and the hardness value is calculated from that in various ways depending on the test used.

Softer metals will give/have deeper indentations and lower hardness number. The most prevalent used testing methods are Brinell (HB/BHN/HBW), Rockwell (HRA/HRB/HRC) and Vickers (HV/DPH). The latter method is the one used in this study. These methods use different material and shape for the indenters, and the indenter must be harder than the metal that is being subjected to the test. It is possible to convert the hardness value from one method to another. However, there are some issues because hardness is vaguely defined

mechanical property that is dependent on what method is used. When doing conversion material, procedure and temperature need to be taken into consideration. [49, pp. 174-178]

There is a correlation between hardness and yield strength of a material. [15][16] Tensile testing is expensive and time-consuming and is inherently destructive. The hardness tests are therefore considered as an alternative method for measuring yield strength. Hardness tests are semi-destructive and simple.

2.5 Precipitation hardening

Precipitating alloying elements as coherent particles from the solid solution is the most common strength increasing method for heat treatable aluminium alloys. [42, p. 148] Precipitation is possible when the solubility of the alloying element is higher at elevated temperatures as this allows for the formation of a second phase. When the temperature is decreased, the solubility falls, and the host matrix rejects the alloying element. Atoms conglomerate into precipitate particles inducing high lattice strains and thus increasing strength. [28, p. 80]

The procedure is performed in three stages. The first stage called solution heat treatment is done by homogenisation by heating the alloy to an elevated temperature where the second phase goes into solution. The temperature should be below the eutectic temperature to avoid local melting, usually in the range of 450 - 500 °C. [28, p. 80]

The material is then cooled depending on the alloy system. This is the second stage. Quenching in water is the most used method as it rapidly cools most aluminium alloys. To attain a Supersaturated solid solution (SSSS), which is required for ageing, the cooling rate must be high enough to avoid diffusion and precipitation of particles from the secondary phase from coming out of solution. If the cooling rate is not sufficient, coarse and non-homogeneous particles will precipitate and be unavailable for strengthening. [51, p. G-39] SSSS is a single phase in solid solution with a non-equilibrium structure, and if left at room temperature, precipitation of hardening particles may occur naturally in a process called natural ageing. The secondary phase is metastable in the solid solution, meaning it is in internal equilibrium, but its energy is above the stable state.

The last stage is to heat the alloy again to a temperature in the range of 160 - 220 °C with a process called artificial ageing. [28, p. 80] The artificial ageing allows the formation of secondary phase precipitation at a controllable level where the temperature and hold time decides the microstructure. For these precipitates to achieve its hardening purpose, they are required to be coherent in the matrix. The material is then allowed to cool while retaining the fine dispersion of precipitates. It is crucial to stop the ageing process before the coherence is broken to achieve peak hardening. If the ageing process is not stopped at the appropriate time, the precipitates will reach its equilibrium phase, and thus peak hardness is not attainable. The material is said to be over-aged if this takes place. It is worth noting that if a precipitation hardened alloy is used in a high-temperature environment, these precipitates can grow or completely redissolve back into solution if the temperature is sufficiently high.
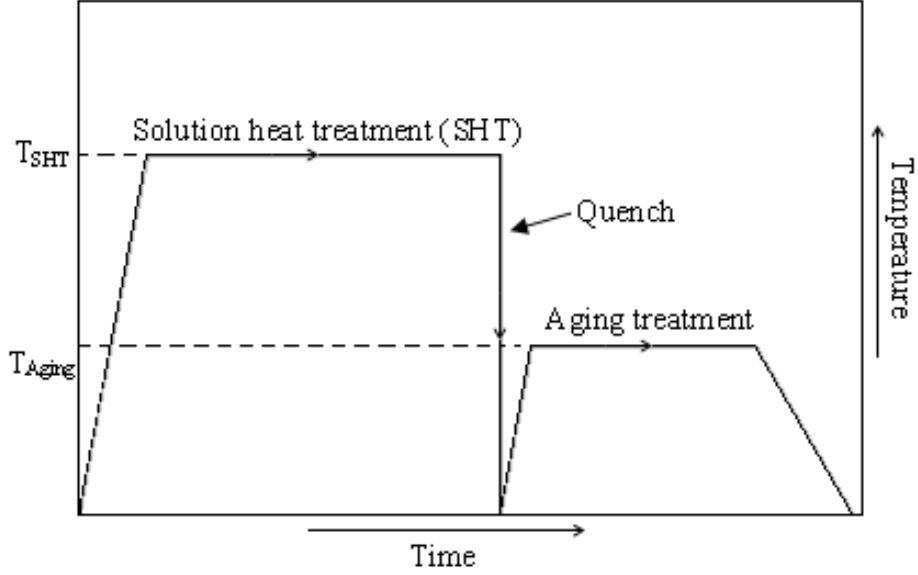
Figure 9: Diagram showing the steps of precipitation hardening. [52]

These fine particles prevent movement of dislocations in the aluminium matrix by creating a grain boundary between phases. This boundary hinders the slip of dislocations. A fine dispersion of precipitates is required to yield high strength in the alloy. If the precipitates are more numerous and thus small, the hardening is most effective. [53] When a dislocation reaches a particle, it either must go around or cut through. This hinders the movement of the dislocation, consequently strengthening the material.

The hardness of a aluminium is directly correlated to its yield strength. The yield strength can be calculated by the following formula [54]:

$$\sigma_y = \sigma_i + \sigma_{ss} + \sigma_p \tag{3}$$

Where σ_y is the yield strength of AlMgSi alloys, σ_i is the strength contribution from the pure aluminium, σ_{ss} is the contribution from the alloying elements, and σ_p is the strength contribution from precipitates.

A decrease in mechanical performance when the heating rate was low has been reported in the literature. [53] The low heating rate allowed precipitates to have more time for growth and dissolution consequently lowering the amount of precipitates and the mechanical properties.

20

2.6 Phase transformations of AlSi10Mg

Precipitation of the various phases occur in a commonly accepted sequence for the ternary AlSiMg alloy system: [55]

$$SSSS \rightarrow GP\ I\ zone \rightarrow GP\ II\ zone/\beta''(needle) \rightarrow \beta'(rod) \rightarrow \beta(Mg_2Si)$$
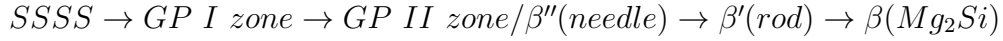
After quenching the supersaturated solid solution, the solubility of Mg and Si decreases. Small Si clusters are diffused out of the solution. Afterwards, Mg clusters are formed and then some co-clusters containing both Mg and Si. Vacancies in the lattice assist the atomic diffusion and clustering of the alloying elements. The co-clusters have a Mg/Si ratio close to 1. [55]

The formation of Guinier-Preston zones (GP) follows after the formation of clusters. GP zones consist of a large number of clusters (up to 10^{18} per cm^3) of the alloying elements, forming 10 - 50 nm long and only one or two atomic planes thick clusters as illustrated in Fig. 10. These zones are coherent with the host matrix and hinder dislocation slip because of the high lattice strain induced. [28, pp. 80-82] Lattice strain is illustrated in Fig. 12 (a).

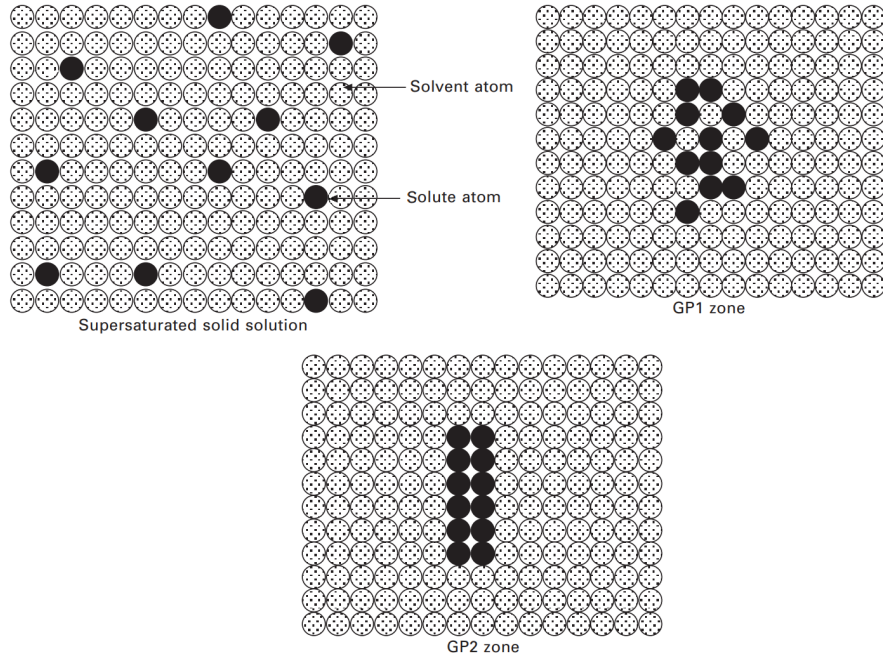Figure 10: Formation of GP zones during ageing. Figure from adapted from: Introduction to aerospace materials. [28, p. 82]

The next step in the age-hardening sequence is the formation of metastable precipitates with a needle-like shape. Such precipitates are referred to as β'' and are oriented along the three (100) directions with a size of 4 nm x 4 nm x 50 nm (see Fig. 14. Peak material

strength is attained when the β'' phase is predominant. [55][28, p. 84] The precipitates size increases during the ageing process, which gives a smaller particle spacing and thus inducing higher lattice strains. In the transition from coherent to incoherent particles, the cutting stress and Orowan stress are highest, and at the point they intersect is peak hardness, as shown in Fig. 11. At this point the dislocations struggle to cut through and bow around the precipitates, pinning the dislocation.
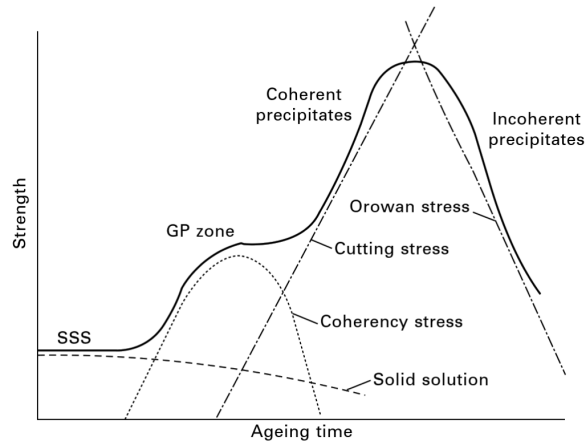

Figure 11: The successive stages of the hardening mechanism in the age-hardening process. [28, p. 81]

In GP zones and the β'' phase, Mg and Si are replacing Al atoms. The arrangement of the atoms is in a string-shape with the sequence: Mg-Si-Mg-Mg-Si-Mg. The diameter of Si and Mg is 0.235 nm and 0.32 nm, respectively. This string of Si and Mg replaces six Al atoms which have a diameter of 0.286 nm. The GP II zone is often referred to as β''. [56]

Continued age-hardening causes β'' particles to grow and transform into hexagonal rod shaped β' particles. These are larger in size (20 x 20 x 500 nm^2).

Eventually β' will transform into the large, plate-shaped, equilibrium state, β, Mg$_2$Si. [56] Coherent precipitates change their crystal structure so that they no longer are continuous with the lattice planes of the host matrix. These precipitates are second phase particles with their own crystal structure and are entirely independent of the host as shown in Fig. 12 (b). This phase has a higher Mg/Si ratio compared to the β' phase. This phase has a known structure and compound formula of Mg$_2$Si. [56] The composition for the most common precipitates in Al-Si-Mg alloys are listed in Tab. 2.

Incoherent precipitates can still enhance material performance as they hinder dislocation slip by promoting Orowan hardening. Dislocations are obstructed since they cannot move across the precipitates because of the change in the crystal structure. Dislocations must loop around the precipitates, hardening the material by a induced stress field as can be seen in Fig. 13. If a new dislocation were to move towards the precipitates with the Orowan loops,

it would first interact with the loops slowing down the dislocation because of the stress bow.

Phase	Composition
GP-zone	Mg_2Si_1
β''	Mg_5Si_6
β'	Mg_9Si_5
β	Mg_2Si

Table 2: Element composition of precipitates. [53]

For many alloy systems, incoherent particles are as sufficient as coherent particles at hindering dislocation slip due to the higher lattice strains and promotion of Orowan hardening. [28, p. 86] Orowan mechanism is most effective when there is a high density of tightly packed particles. Strength increase from the bowing mechanism can be expressed as:

$$\tau_B = \frac{Gb}{L - 2r} \tag{4}$$

Where τ_B is the strength increase from the bowing mechanism, G is the shear modulus, b is the burgers vector, L is the spacing between precipitates (from centre to centre), r is the radius of the precipitates. In other words, the denominator is effectively the particle spacing. [57] The strengthening mechanism is a function of the particle radius. Therefore, the strengthening mechanism is decreased as the particles get larger.
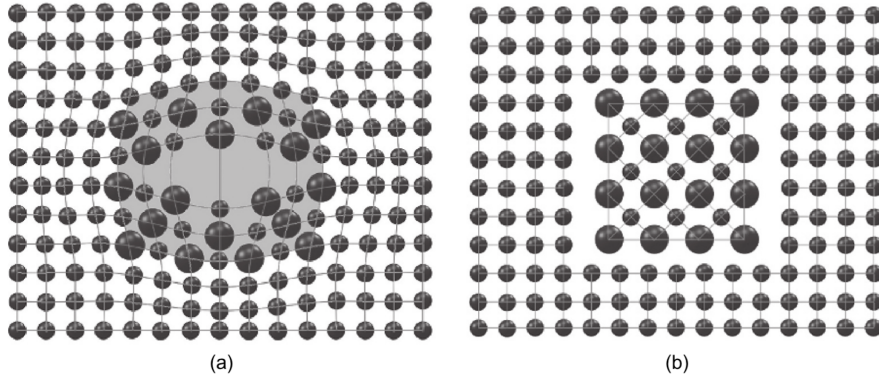
Figure 12: (a) Coherent precipitate structure and (b) incoherent precipitate structure. [28, pp. 84-85]
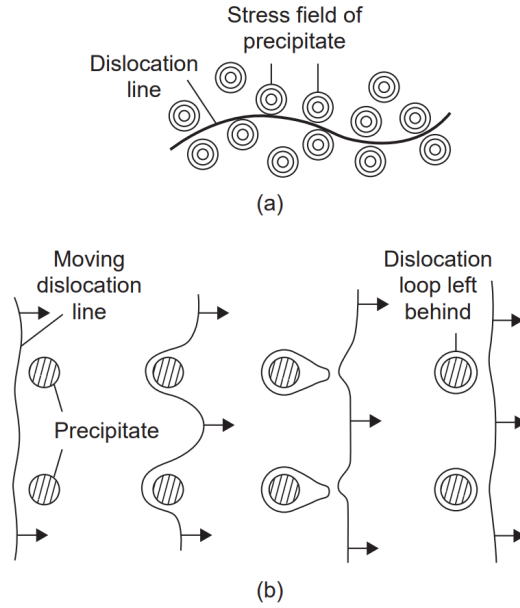
Figure 13: Orowan looping. [50, p. 396]

Figure 14: A low magnification micrograph of β'' precipitates. Needles are visible along the three (100) direction. The dark spots are particles directed in the viewing direction. A larger white spot is visible in the centre of the image. This is a β' directed in the viewing direction. [56]

2.7 Residual stresses

Residual stresses are stresses that reside in the material after it has reached equilibrium within its environment. Such stress can be both wanted or unwanted, depending on the situation. In most cases, residual stresses are not desired. [20] However, compressive residual stresses will for some parts (e.g. fan blades and glass) increase load and scratch resistance. For structural components, tensile residual stresses can be detrimental as the stress promotes crack growth which leads to fatigue failure. Residual stresses can also result in unwanted deformations in the intended part shape. In welding, this is a significant concern because of the heat, causing localised expansion. As the temperature in the weld decreases the different areas cool at different rates which may result in residual stress. In cast parts, residual stresses from uneven cooling are also seen. Tensile stress is noted as positive and conversely, compressive stress negative. [49, p. 423]

Residual stresses arise from three predominant reasons and are characterised after at what scale they affect the material. [58] Macro-residual stresses have an impact on the material over larger distances. Micro-residual stresses affect grains or grain boundaries and vary from one grain to another. Residual stresses can also affect the material at the atomic level.

Type I is macro-residual stress resulting from uneven cooling. A part cooling from an elevated temperature will experience varying cooling rates throughout the part. This is prominent in thicker cast parts but is also seen in parts made with SLM process as the areas where there are overlapping scan tracks will retain an elevated temperature.

Type II is micro-residual stress developed within grains as the crystal structure changes. Phase transformations occur as a part is heated and cooled in the fabrication and post-processing processes. The volume will change in line with the temperature. The crystal structure of steel changes as martensite (TBC) is formed from austenite (FCC). Because of the change in the crystal structure, austenite is denser than martensite, and this leads to residual stresses.

Type III is residual stress caused by mechanical processing and affects the stress at the atomic level within the grain. During fabrication, a part can experience a variety of mechanical processes such as bending, drawing, rolling and extrusion. These processes create plastic deformations which generate residual stresses.

2.7.1 Residual stresses in additive manufactured parts

Residual stresses in SLMed parts are of interest because of the non-uniform plastic deformation during heating and cooling cycle, high temperature gradients and thermal expansion. Scanning parameters, temperature treatment, support structures and material chemical composition affect residual stresses in SLMed parts. [17][18].

Type I and type II are the most prominent in parts produced with SLM. This is due to

the nature of the process where there is repeatedly heating of the material, and phase transformations may occur. [20] Type I residual stress arise in SLM parts because of large thermal gradients in the melt pool. In aluminium alloys, a steep temperature gradient develops due to the high thermal conductivity and rapid heating by the laser beam of the upper surface. Material strength is reduced at elevated temperatures, and elastic compressive strains arise due to the underlying material restricting the expansion of the heated top layer (see Fig. 15. As the melt pool solidifies, the volume decreases, causing thermal contractions. The top layer is plastically compressed when the material's yield strength is surpassed. Without mechanical constraints, the part bends away from the laser beam. [20]. Type II residual stress come from different phases in the material, but has less impact on the material's strength. [20]
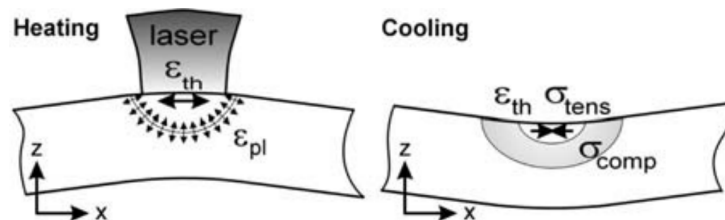

Figure 15: Temperature gradient mechanism. [20]

For SLMed parts, a low temperature heat treatment is recommended to reduce residual stresses, which may induce microcracks and distortions. Such stress reliefs reduce the ultimate tensile strength and yield strength but the elongation to failure is slightly increased. [21]

2.8 Analytical methods

2.8.1 Electron microscopy

Transmission electron microscopy (TEM)
TEM is a microscopy technique which utilises the short wavelength of the electron compared to optical microscopy which uses photons. The wavelength of electrons is 1/100000 of the wavelength of visible light, which gives TEM images a very high resolution. Samples that are to be investigated in a transmission electron microscope are required to be thinned down to a thickness of less than 100 nm. The acceleration voltage decides if the electrons are able to transmit through the sample. The higher the accelerating voltage, the thicker specimens the electrons can penetrate and vice versa. TEM operate at 60-300 kV accelerating voltage.

Scanning electron microscopy (SEM)
Unlike TEM, which uses electrons that are transmitted, SEM utilises electron scattering (elastic and inelastic) to study samples. SEM does not have an as high resolution as TEM, but it has a greater field of view.

Back-scattered detector (QBSD):
High energy primary electrons are accelerated out of an electron gun in which interact with the atoms in the specimen. The electrons are backscattered (reflected) out of the specimen

26

by elastic scattering. Heavier elements (high atomic number) backscatter more electrons than light elements (low atomic number), and hence the areas with heavier elements appear brighter in the image. Heavier elements are exerting a greater force to elastically scatter the electrons compared to a light element. The contrast generated by different elements can be used to determine areas where there are elements with either low or high atomic number.

Energy dispersive X-ray spectroscopy (EDS):
EDS is an analytical technique to determine the elemental composition of a sample. When an electron from the emission gun inelastically interacts with an electron in the specimen, the secondary electron is kicked out of its position, and an electron from an outer shell will go down to the lower energy state and radiate X-ray with a characteristic wavelength. These X-rays are converted to voltage signals, and an EDS spectrum can be created. The peaks in a spectrum tell how much of each element there are in the sample.

Electron backscatter diffraction (EBSD):
EBSD is a characterisation technique used to study the crystal orientation, phase or structure in the sample.

2.8.2 Optical microscopy

Optical microscopy, also known as light microscopy, uses lenses to magnify visible light (380-750 nm). Optical microscopy is an inexpensive method to study the macrostructure of a material.

2.8.3 Residual stress calculation

Residual stresses can be measured with a variety of different methods. They can be destructive, semi-destructive and destructive or based on diffraction, strain relaxation or other methods. However, they all have to be calculated from measured values. There is no known method of directly measuring residual stress.

X-ray diffraction measures residual stress by analysing the distance between crystallographic planes. If there is residual stress in a material, the spacing between planes will vary from when it is in a stress-free state. If there is tensile residual stress present in a part, the lattice spacing is increased in the planes parallel to the stress direction, and conversely, the lattice spacing perpendicular to the tensile residual stress will decrease. This is shown in Fig. 16.

If the crystallite is inhomogeneously strained (see Fig. 17, the Bragg's angle, λ, is changed, causing broadening of the diffraction peaks will occur. Precipitates, vacancies layer faults and dislocations cause inhomogeneous strain in the crystallite.
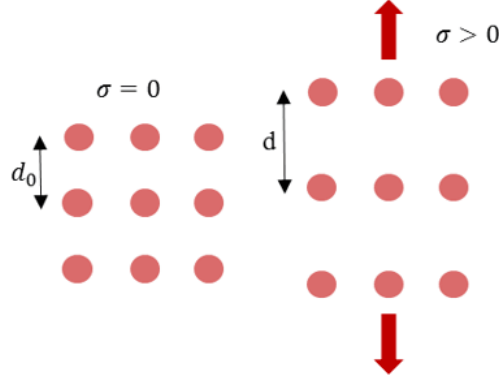
$$\lambda = 2dsin\theta \tag{5}$$

Figure 16: Lattice structure without residual stress (left) and with residual stress (right). [59]

Eq. 5 is Bragg's law where λ is the wavelength, d is the lattice distance, θ is the diffraction angle.
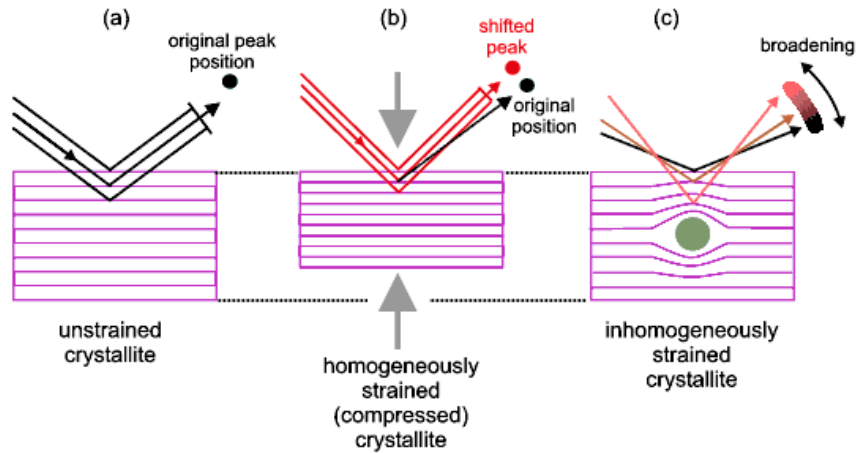

Figure 17: Inhomogenous crystallite strain. [60]

Williamson-Hall approach:
Calculating strain by the Williamson-Hall (WH) plot method: Based on XRD data the broadening of the peaks, $\beta(\theta)$, is due to the combined effect of size and micro strain broadening.

$$\beta(\theta) = \frac{K \cdot \lambda}{d \cdot \cos\theta} \qquad \text{Size broadening} \qquad (6)$$

Where K is a dimensionless shape factor, λ is the X-ray wavelength, d is the crystallite size and θ is the Bragg angle.

$$\beta(\theta) = 4\epsilon\frac{\sin\theta}{\cos\theta} \qquad \text{Micro strain broadening} \qquad (7)$$

Where ϵ is the strain and θ is the peak position in radians.

Combining Eq. 6 and Eq. 7 and multiplying with $\cos\theta$ gives:

$$\beta(\theta) \cdot \cos\theta = \frac{K \cdot \lambda}{d} + 4\epsilon\sin\theta \tag{8}$$

Eq. 8 represents a straight line (y=ax+b). The first part on the right-hand side of the equation is where the slope intercepts on the y-axis, and the second part is the slope of the line. $\beta\cos\theta$ can now be plotted on the y-axis against $\sin\theta$ on the x-axis. The slope of the plot is the strain. ϵ is a dimensionless quantity and gives no other information than ration between two lengths. The WH method is considered to be the superior method of calculating strain for this study because it uses the diffraction angle (2 θ) which combines the effect of size and strain broadening. [61]

Halder-Wagner approach:
The Halder-Wagner (HW) method is used for the determination of d and ϵ by an alternative equation to the WH method.

$$\left(\frac{\beta^*}{d^*}\right)^2 = \frac{K}{d} \cdot \frac{\beta^*}{(d^*)^2} + (2\epsilon)^2 \tag{9}$$

Where β^* is the integral breadth of the reciprocal lattice point and d^* is the lattice spacing for the reciprocal cell given in Eq. 10 and Eq. 11 respectively.

$$\beta^* = \frac{\beta\cos\theta}{\lambda} \tag{10}$$

$$d^* = \frac{2\sin\theta}{\lambda} \tag{11}$$

Eq. 9 can be rearranged to:

$$\left(\frac{\beta\cos\theta}{\sin\theta}\right)^2 = \frac{K\lambda}{d} \cdot \frac{\beta\cos\theta}{\sin^2\theta} + 16\epsilon^2 \tag{12}$$

Similarly to the WH method, Eq. 12 has the form of a straight line. $(\beta\cos\theta/\sin\theta)^2$ can be plotted against $\beta\cos\theta/\sin^2\theta$. The slope of the resulting line is $K\lambda/d$ and the y-intercept is $16\epsilon^2$. Data for reflections at high diffraction angles are given less weight than low and intermediate angles. High diffraction angles are often less reliable; thus, the HW method has an advantage over WH method. Unlike the WH method, the HW method does not include a constant which is preferred. [62]

2.8.4 Hardness testing

Vickers hardness testing (also called diamond pyramid hardness testing) is a microindentation method that indents the metal with a pyramid-shaped indenter (see Fig. 18). The

indenter is pressed into the surface of the metal, leaving an imprint which is measured using a microscope. The applied load is in the range of 1 g to 1000 g, which is much lower than Brinell and Rockwell. The measured values are put into Eq. 16 to get the hardness number. The test specimen is required to have a properly prepared surface finish to prevent scratches and dents from disturbing the measurements from being accurately measured. The measurements are nowadays automated by indenter apparatus being connected to a computer with an image analyser. [49, p. 177]

$$d = \frac{d_1 + d_2}{2} \tag{13}$$

$$A = \frac{d^2}{2sin(136°/2)} \approx \frac{d^2}{1.8544} \tag{14}$$

$$HV = \frac{F}{A} \approx \frac{1.8544F}{d^2} \tag{15}$$
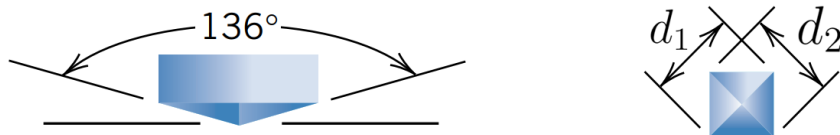
$$HV = \frac{1.8544F}{d^2} \tag{16}$$

Figure 18: Vickers diamond indentation. [49]

3 Experimental details

Mechatronics Innovation Lab A/S in Grimstad provided and performed heat treatment of the specimens used in this study. This spring, laboratory access was limited due to COVID-19 restrictions. Following this, a few employees suddenly had the responsibility of performing experimental work for many students. Senior engineer Tucho at the IMBM laboratories at UiS carried out all of the experimental work and contributed substantially to this chapter.

3.1 Production of SLM specimens

Two twin sets of test specimens were built where each set consisted of three specimens. The specimens were built in an SLM280 2.0 machine from SLM Solutions. One set was to be investigated in the as-built condition (no heat treatment) and on set to be investigated after a heat treatment. Each set contained three specimens:

- One rod built in the vertical direction (normal to x-y plane) (10x10x200mm)

- One rod built in the horizontal direction (parallel to the x-y plane) (10x200x10mm)

- One cube built in perpendicular to x-y plane (30x30x200mm)

The two test rods were to be used for Vickers hardness testing, optical microscopy, SEM and TEM. The cube was made for cutting into thin plates for X-ray diffraction and additional hardness testing.

RF-PS AlSi10Mg powder was provided by TEKNA. The chemical composition is given in Tab. 3. Process parameters for SLM 280 is listed in Tab. 4. The contour of the part was scanned first, then the volume. Each layer was rotated 67°. The parts were built on a 150°C pre-heated building platform. For one set of the twins, a low-temperature heat treatment was performed at 300 °C for two hours then furnace cooled.

Al	Si	Mg	Mn	Cu	Ni	Sn
>88	9-11	0.20-0.45	<0.45	<0.10	<0.05	<0.05

Table 3: AlSi10Mg powder composition chemical in wt.%. [63]

Figure 19: Printed specimens. From the left: cube for residual stress analysis and hardness testing, vertical rod and horizontal rod. The round box contains AlSi10Mg powder used for SEM imagery and residuall stress analysis. Photo credit: Mechatronics Innovation Lab AS

Parameter	Value
Laser power	350 W
Scanning speed	1150 $mm\ s^{-1}$
Spot size	75 - 80 μm
Layer thickness	50 μm
Hatching Distance	170 μm
Shielding gas	Argon

Table 4: Process parameters for the SLM 280 machine from SLM Solutions.

3.2 Specimen characterization

Before grinding and polishing the printed samples were cut into pieces (see Fig. 20), with an abrasive cutting machine, Struers Disctom 10, using diamond-rimmed wheels. Theses pieces were again further sliced for grinding and polishing using Struers Accutom-2. The samples were labelled with a number corresponding to where on the specimen they were cut from and with two letters. The first letter indicates if the sample was as-printed (A) or heat treated (H) and the second letter indicates if it was the vertically printed (V) or horizontally printed (H) specimen. For example, a sample from the bottom part of the vertically printed heat treated specimen would be labelled "HV5". The cubes were cut in thin slices to be

examined by XRD and labelled bottom, middle or top. Material from the bottom, middle and top of the cubes were also extracted for hardness testing.
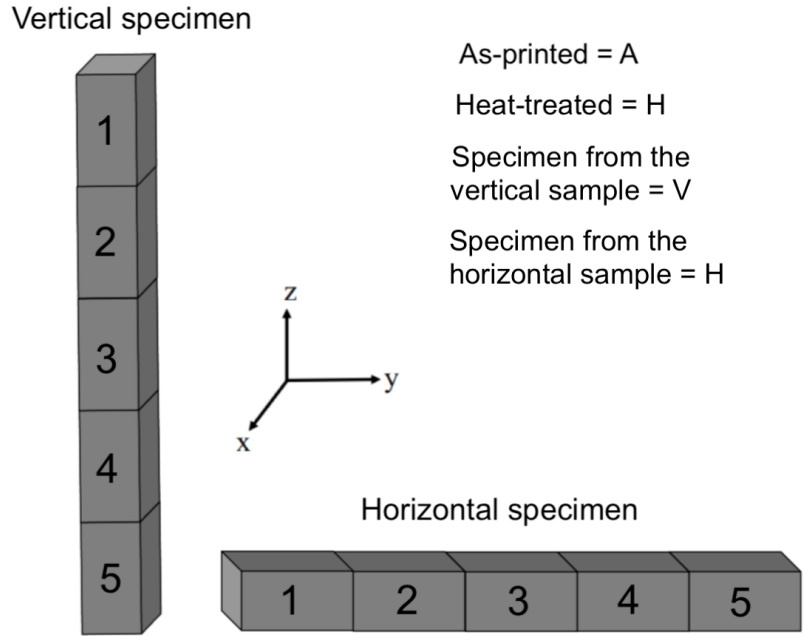

Figure 20: An illustration of how the specimens were divided into sections.

3.2.1 Optical microscope

Optical micrographs were recorded using OLYMPUS GX53. Samples were grinded with 220, 320, 500 and 1200 carbide grits. Followed by polishing with 9 μm, 3 μm, and 1 μm diamond suspension on polishing clothes. Finally samples are finished with chemo-mechanical polishing with OPS (oxide polishing suspension). The samples were etched with 1g NaOH + 100 ml distilled water for 2 minutes by immersion.

3.2.2 SEM

The microstructure of the samples was studied with Gemini SUPRA 35VP, equipped with EDAX Energy Dispersive X-ray Spectroscopy (EDS) detector. Sample preparation for investigation with SEM consisted of mechanical grinding, followed by fine polishing and finally, ultra-polishing with OPS colloidal silica.

Step	Surface/abrasive	RPM	Load	Applied time	Coolant
1	320 grit SiC paper	300	25 N	Until plain	Water
2	9 μm MD-Plan cloth	150	40 N	5 min	Diamond
3	3 μm MD-DAC cloth	150	35 N	3 min	Diamond
4	MD-Chemomet cloth	150	30 N	2 min	Colloidal Silica (OPS), then adding water before time ended by 20s

Table 5: Polishing procedures.

3.2.3 TEM

A JEOL-2100(LaB$_6$ filament) electron microscope operating at 200 kV was used for TEM. It was equipped with EDS and annular bright and annular dark-field detectors. For TEM observations, thin foils were prepared. First by thinning down mechanically to a thickness of about 100 micrometers, and then punched 3 mm disks from the foils. These disks were then electropolished using a dual jet polishing system, Struers TENUPOL-5 operated at 20 V and -27 °C in an electrolyte solution of 70 % methanol, 20 % glycerol, and 10 % perchloric acid.

3.2.4 Hardness testing

Hardness tests were performed using a Vickers Struers DuraScan testing machine using 0.2 kg HV loads with a dwell time of 10 seconds. The samples tested were polished according to the requirements for Vickers hardness testing. The interval between each indentation is 0.5 mm and between 11 and 15 measurements was done for each sample.

4 Results

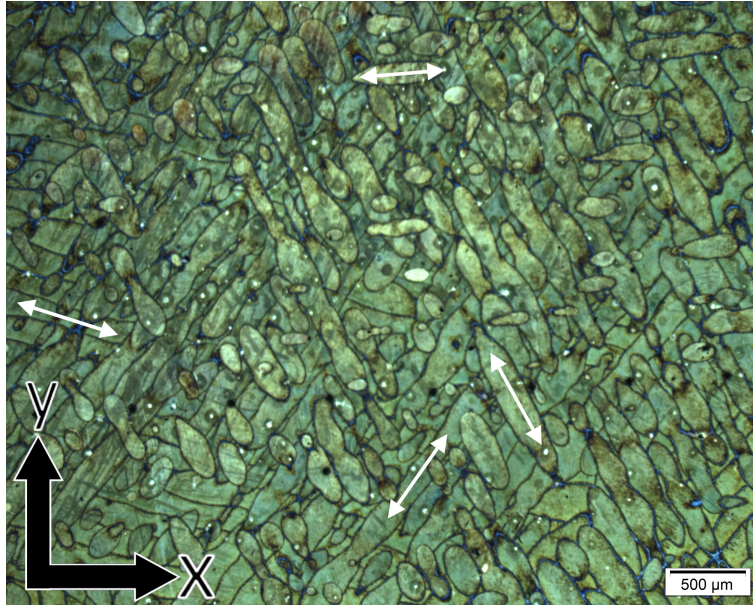## 4.1 Optical microscopy

4.1.1 As-printed vertical

Figure 21: A low magnification image of melt pools in xy-plane of the as-printed vertical specimen.

Arrows indicate four scanning directions on the xy-plane in Fig. 21. Each direction represents a deposited and melted layer. Several layers can be observed, and some of the melt pools appear nearly circular. This is a result of the polished surface not being parallel to the fabrication plane, and the cross-section is not perfectly aligned with the centreline of the melt pools. There is also a variation in depth and shape of the melt pool as they are not always continuous. Thus the images may not represent the actual geometry of the melt pools.

Fig. 22 (a) is a magnified section from Fig. 21. White spots can be observed all over the image in Fig. 22 (a) and on the magnified image in Fig. 22 (b). The spot has a large bright center with some adjacent smaller spots. The chemical composition can not be determined from these images. Coarser microstrucutre along the edge of the melt pool are observed in Fig. 22 (b).

The angle between two melt pools was measured to be 64° as shown in Fig. 23 for the as-printed vertical specimen. This value is set to be 67 °as a SLM process parameter when producing samples. The deviation from the measured angles to the process parameters can come from polishing not being normal to the z-direction. In other words, the edges of the cross-section of a melt pool vary as the diameter is changed. A deviation can also arise from uneven dispersion of powder before melting
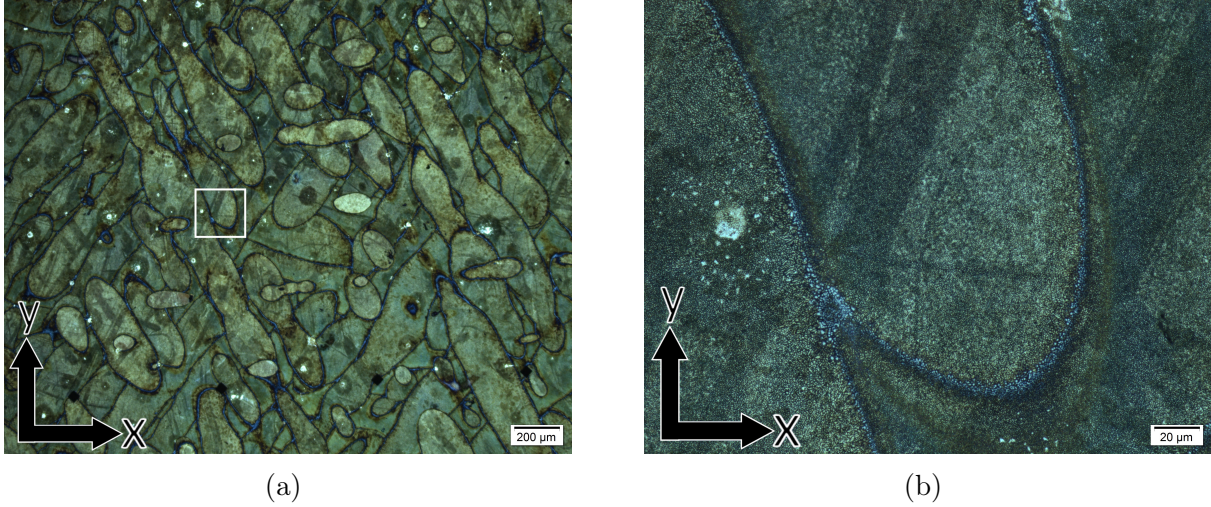
Figure 22: Optical images of the as-printed vertical specimen normal to the building direction. (b) is the magnified image indicated by white box in (a).
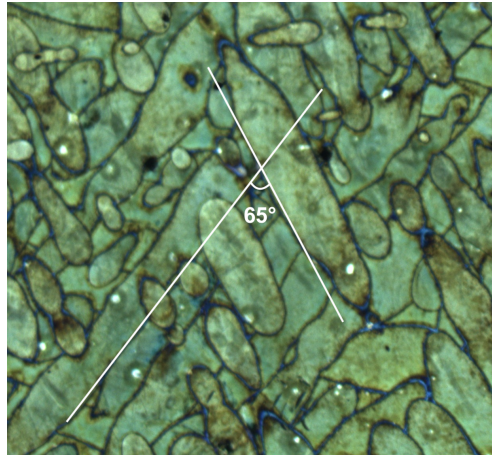

Figure 23: Angle measurement between two melt pools for the as-printed vertical specimen.

4.1.2 As-printed horizontal

The microstructure of the cross-section of the melt pool appears a half-cylindrical shape with some melt pools in the longitudinal direction. Such half-cylindrical shapes form when the laser traverses across the powder bed. As shown in Fig. 24, the half-cylindrical shapes form a fish-scale-like pattern with some longitudinal melt pools. Due to high image compression, some of the optical micrographs have low image resolution. Low resolution makes it difficult to distinguish microstructure, but melt pools are visible.

Fig. 25 shows epitaxial growth towards the subsequent layer. These grains grow towards the centre of the melt pool above. Such epitaxial growth can be seen in the bottom right corner and top area of Fig. 25. A fine microstructure can be seen at the bottom of the top melt pool. Some dendritic microstructure can also be observed.
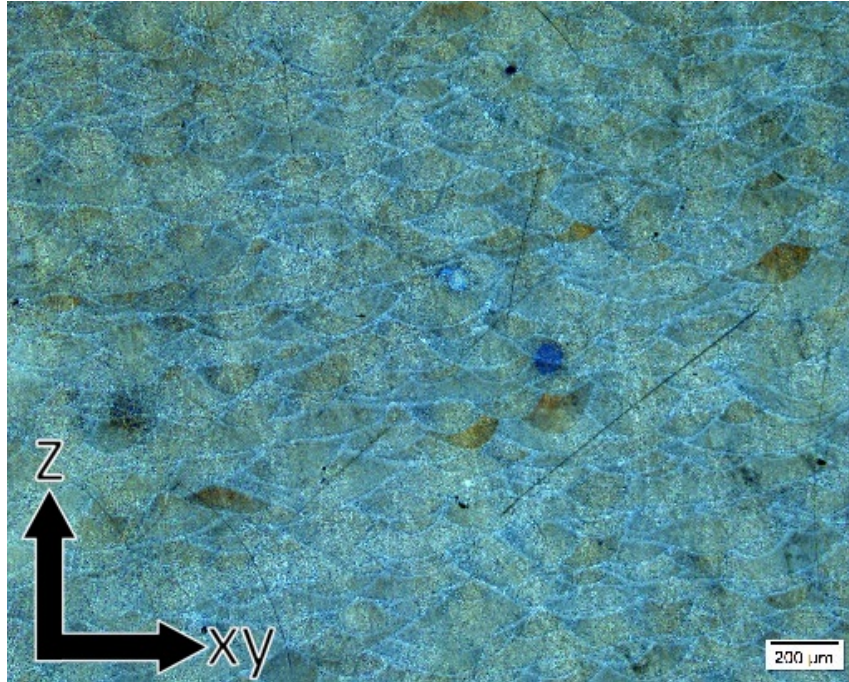
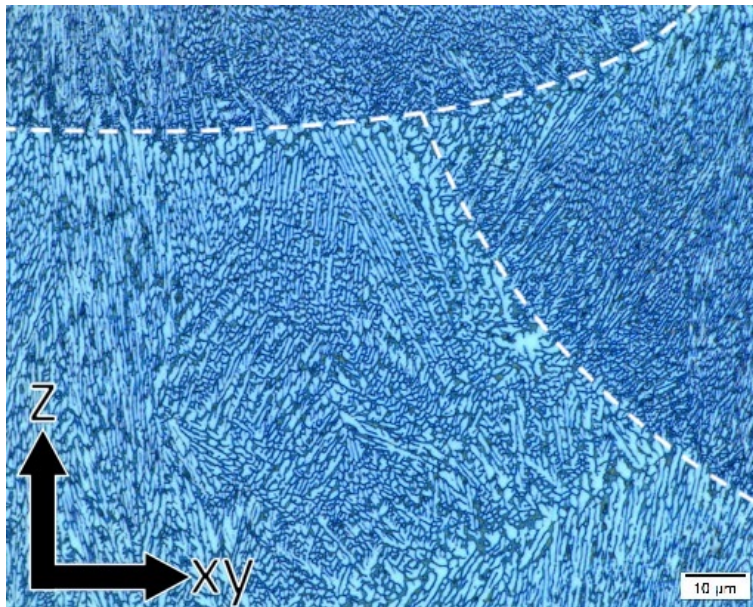Figure 24: Optical micrograph of the as-printed horizontal specimen.

Figure 25: Optical micrograph of epitaxial growth in the as-printed horizontal specimen. The dashed lines indicate melt pool boundaries.

At the intersection indicated by the white box in Fig. 26 (a), coarser grains are observed. This region is repeatedly heated from the laser as it moves twice in the layer scanned in the oblique y-direction and then twice again in the subsequent layer. The cyclical heating in this region elevates the temperature over a more considerable period of time, allowing grains to grow.

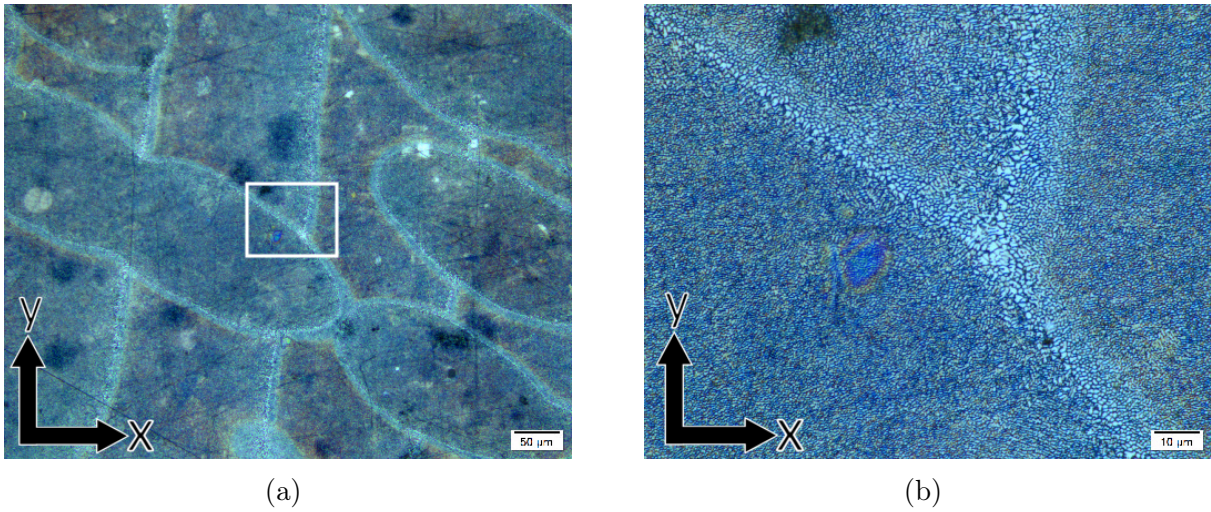(a)   (b)

Figure 26: Coarse microstructure at the intersection between two layers seen in the xy-plane. (b) is a magnified image of the white box indicated by (a).
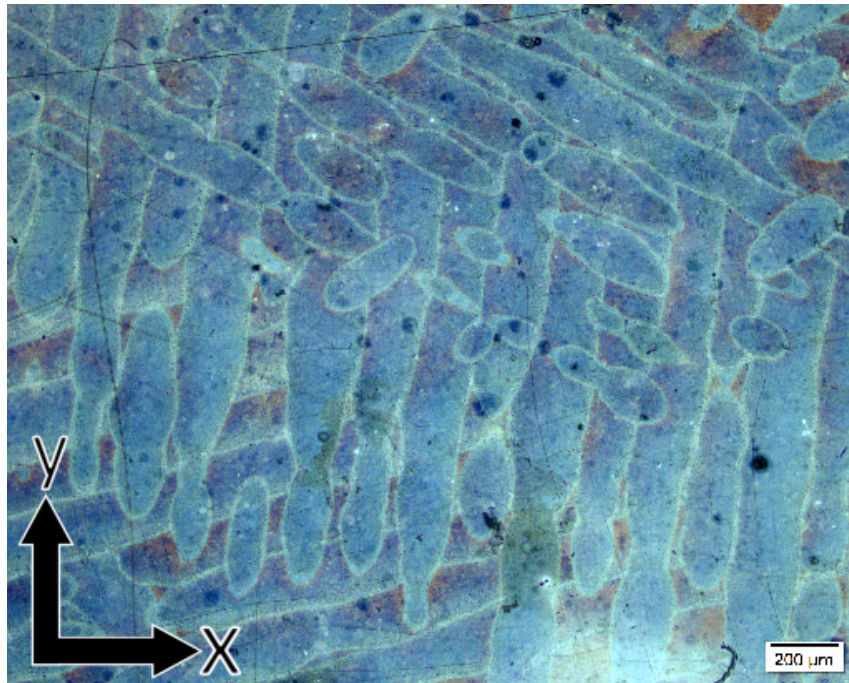

Figure 27: Melt pool overview of the as-printed horizontal specimen in the xy-plane.

An overview of melt pools in the slightly tilted y-direction is shown in Fig. 27. For the almost vertical melt pools, the laser travelled in positive and negative y-direction while moving to the negative x-direction. The laser moved in the negative x-direction (in the xy-plane). This can be determined because the adjacent track overlaps the left-hand side of the melt pools.

4.1.3   Heat treated vertical

A low magnufication image of the typical scan track pattern is shown in Fig. 28.
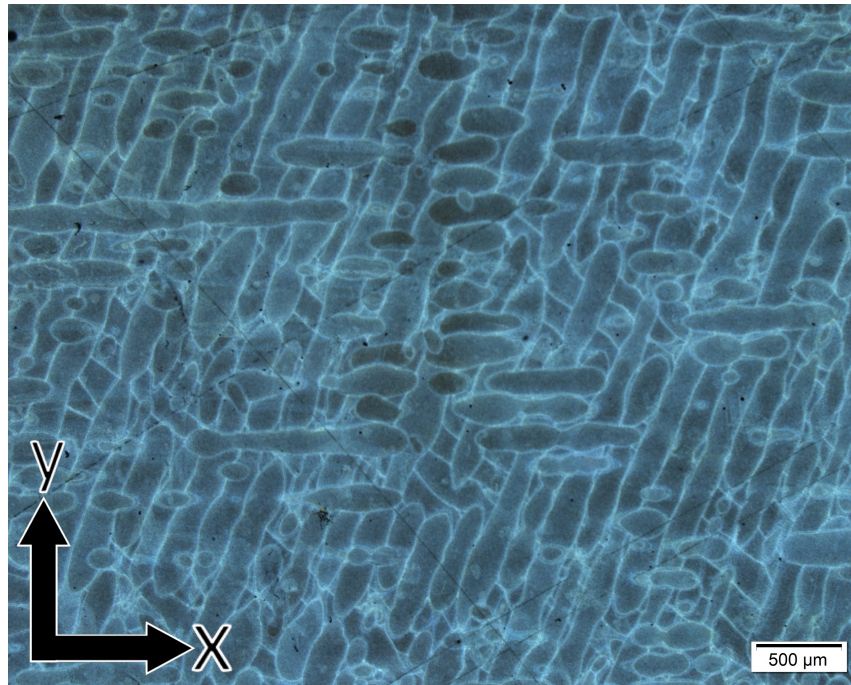

Figure 28: Low magnification optical micrograph of the heat treated vertical specimen.

Fig. 29 show the melt pool boundaries. At this magnification, it is difficult to determine the microstructure. Nevertheless, it appears as the heat treated specimen has a coarse microstructure at the melt pool boundaries and grains are also larger where there are several melt pool boundaries close to each other as observed in the as-printed specimens.

Angle measurements between melt pools were performed as illustrated in Fig. 30 (a) and (b). The measured angle is 69°for both of the measurements.
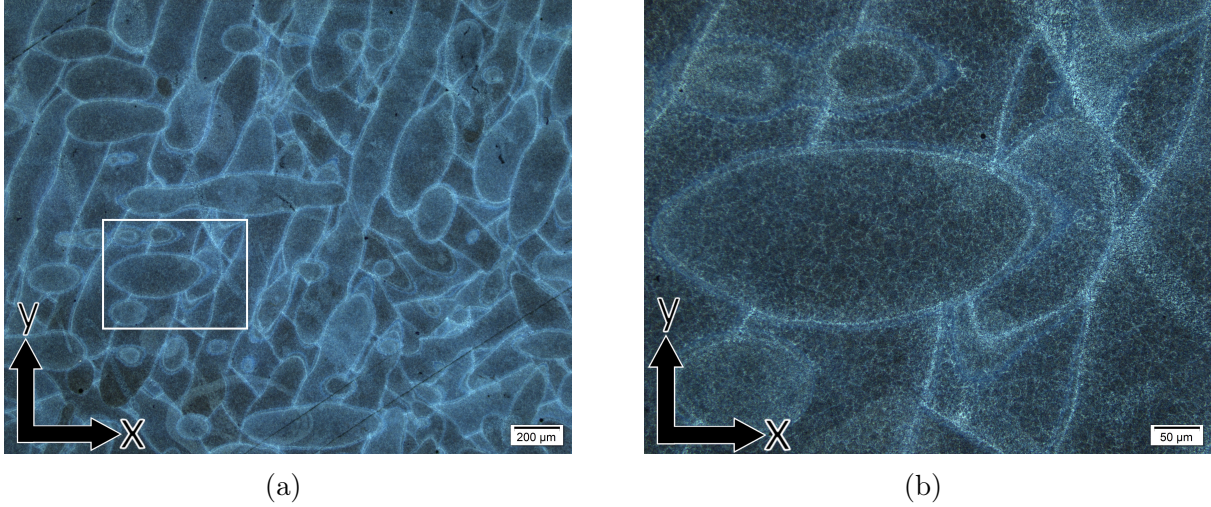
Figure 29: Optical micrograph of the heat treated vertical specimen showing melt pool boundaries. (b) is a magnified image of the white box indicated by (a).
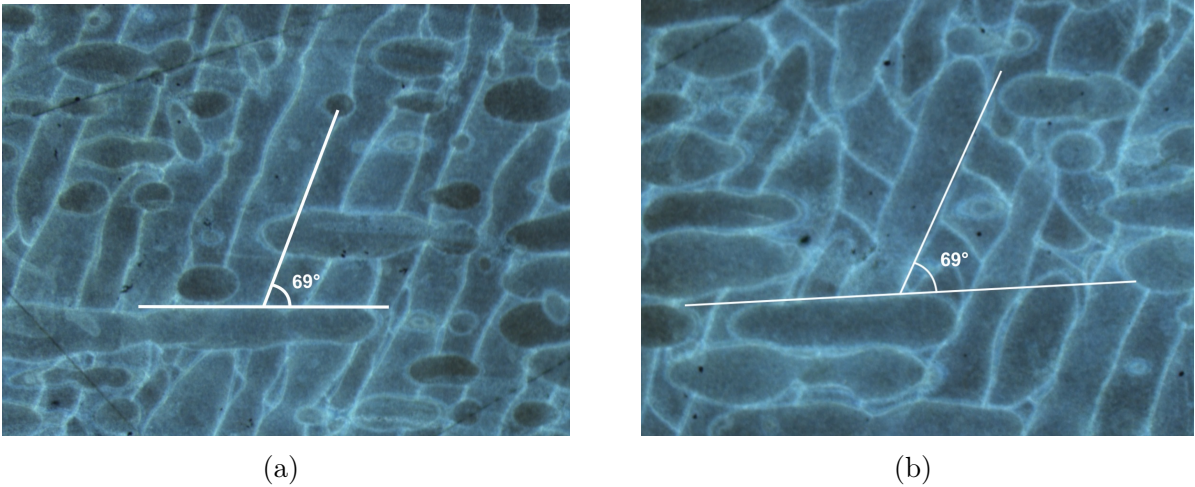

Figure 30: Melt pool angle measurements of the heat treated vertically printed sample.

4.1.4 Heat treated horizontal

Some epitaxial growth and dendritic structure can be seen in Fig. 31 (b). However, due to the low magnification it is difficult to determine.

Fig. 32 shows the melt pools overlapping each other even though the the hatch spacing is greater than the spot size. This shows that the melt pool is significantly larger than the spot size due to high thermal conductivity of aluminium. The heat treated specimens still has a coarser microstructure at the melt pool boundaries as seen in Fig. 33.

Fig. 34 shows how the traversal and longitudinal of a cross section of the melt pools. This is evidence of the layer rotation. The layer rotation can be seen in Fig. 35.

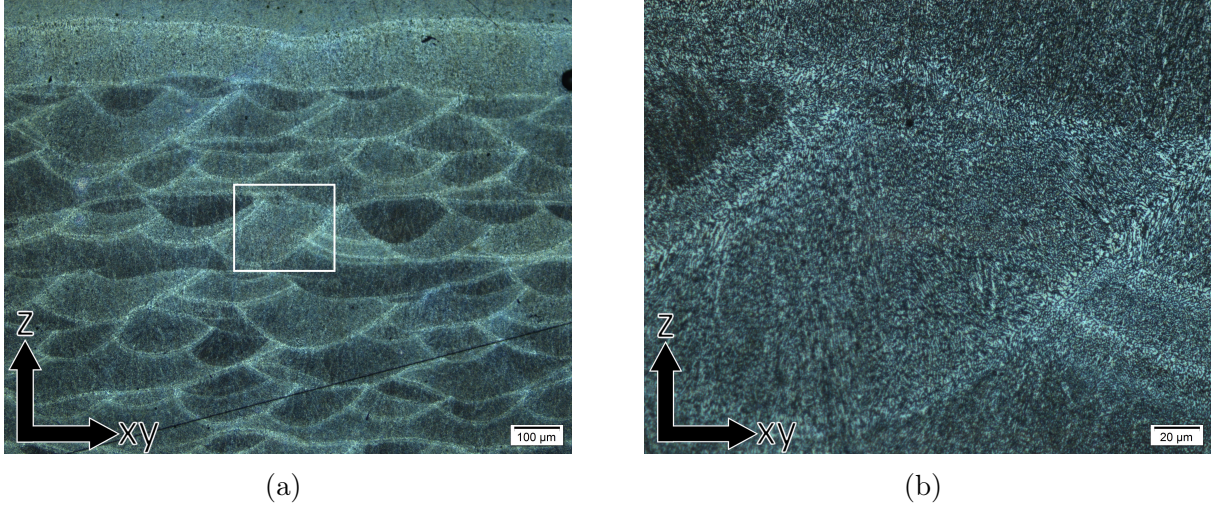(a)   (b)

Figure 31: Cross-section showing the melt pool boundaries. (b) is a magnified image of the white box indicated by (a).
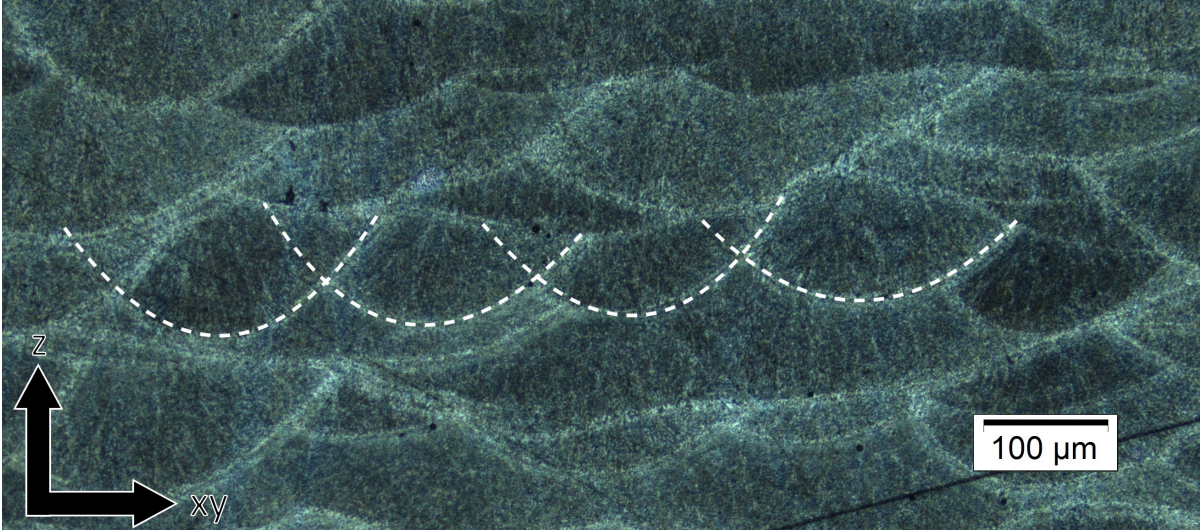

Figure 32: Cross-sectional view of melt pool overlap.

Fig. 36 (b) show a melt pool that has transitioned from conduction mode to keyhole mode melting. The melt pool has penetrated through two layers.

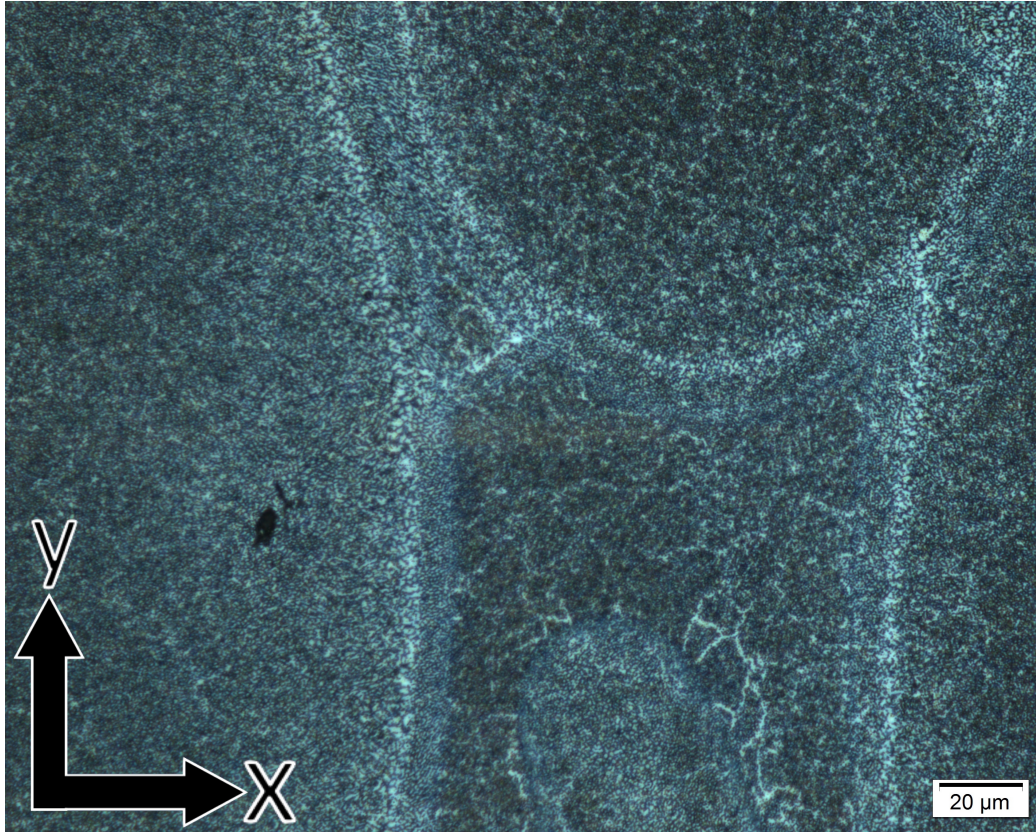Figure 33: Optical micrograph of the melt pool boundaries of the heat treated horizontal specimen.
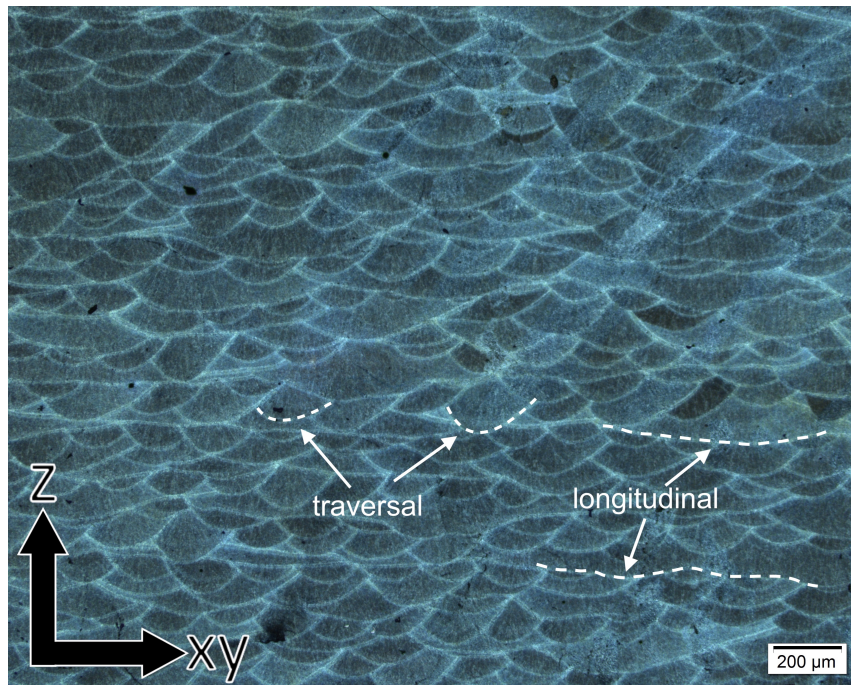

Figure 34: Cross-section of melt pools showing traversal and longitudinal melt pools.
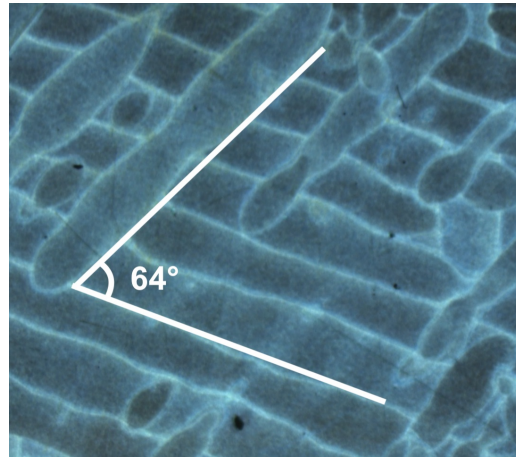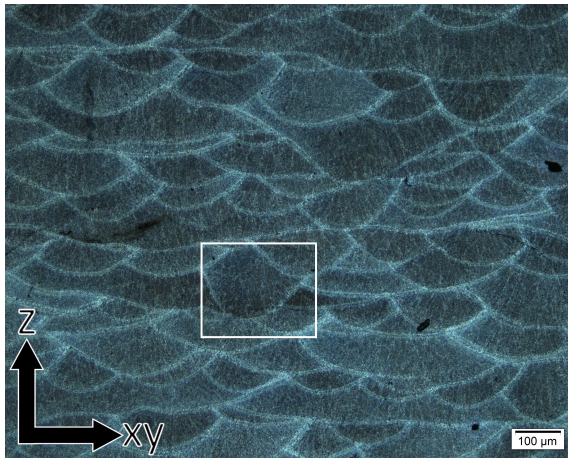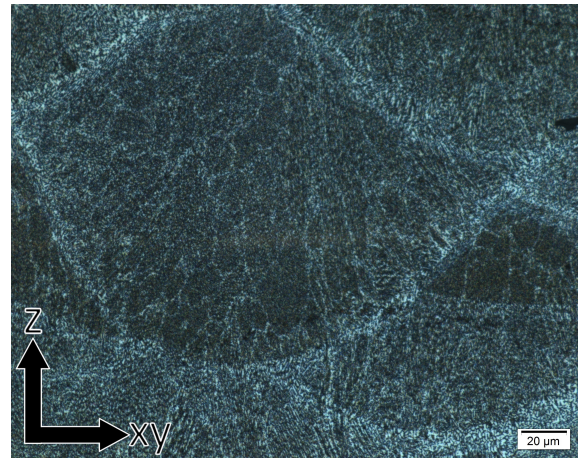
Figure 35: Melt pool angle measurement of the heat treated horizontally printed sample.

(a)

(b)

Figure 36: Conduction mode melting in the heat treated horizontal specimen. (b) is a magnified image of the white box indicated by (a).

4.2 SEM

Unfortunately, no SEM images of the heat-treated specimens were recorded due to the restrictions of the laboratories.

4.2.1 AlSi10Mg powder

Fig. 37 shows an SEM image of the RF-PS produced AlSi10Mg powder. The powder particles are spherically shaped with a smooth surface with little representation of irregularly shaped particles. The white arrows point at particles that have collided with liquid powder during powder fabrication. Such splat can occur as a molten particle meets a solidified particle, collapsing and covering the solid particle. Many of the larger powder particles have smaller particles (satellites) attached to them. Such satellites are undesired as they reduce flowability.
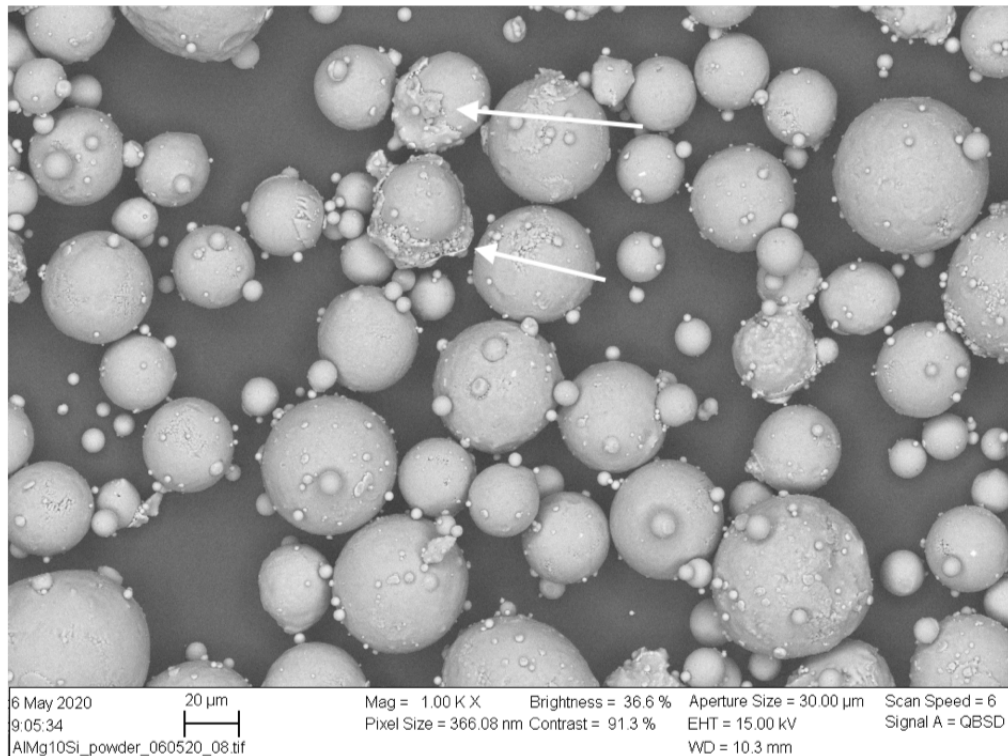
Figure 37: Low magnification SEM image of AlSi10Mg powder.

There is a difference in the size of the powder spheres, as shown in Fig. 38. The larger particles are measured to be up 61 μm in diameter. Many smaller particles in the single-digit range can be observed, but no measurements of the smaller particles nor a particle size distribution have been performed in this study.

Fig. 39 shows a high magnification image of AlSi10Mg particles. It can not be determined from this image if the two larger particles have adhered to each other. Between the two larger particles, many small particles have accumulated. These particles are wedged in between which may come from handling and transportation of the powder.

44
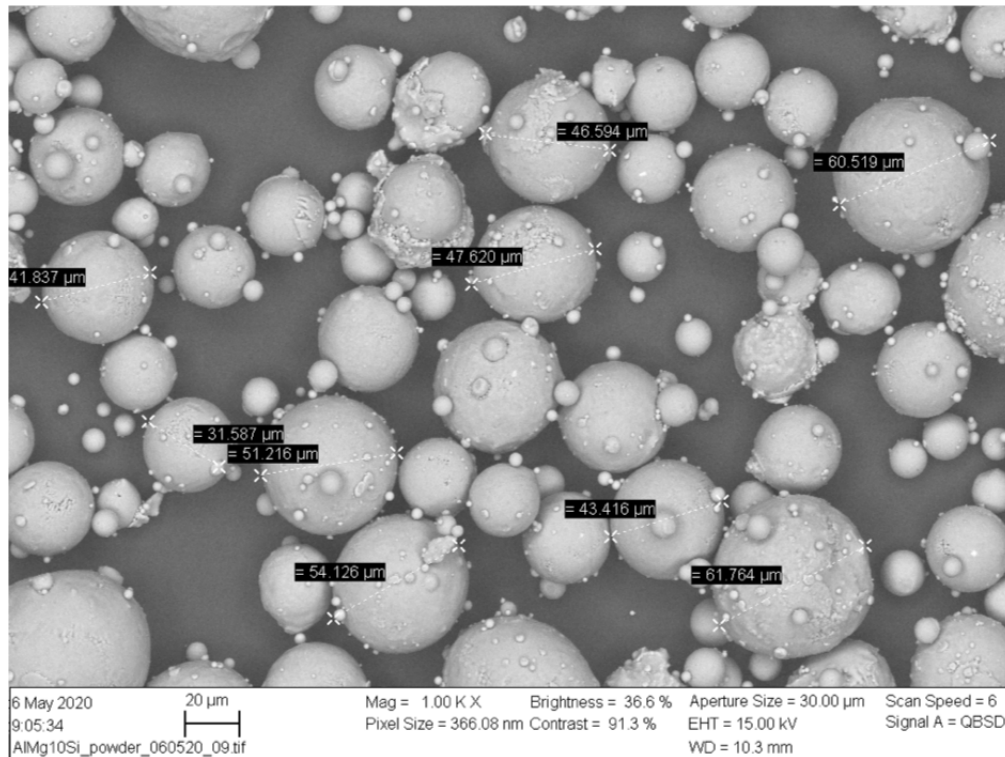
Figure 38: Particle size measurements.
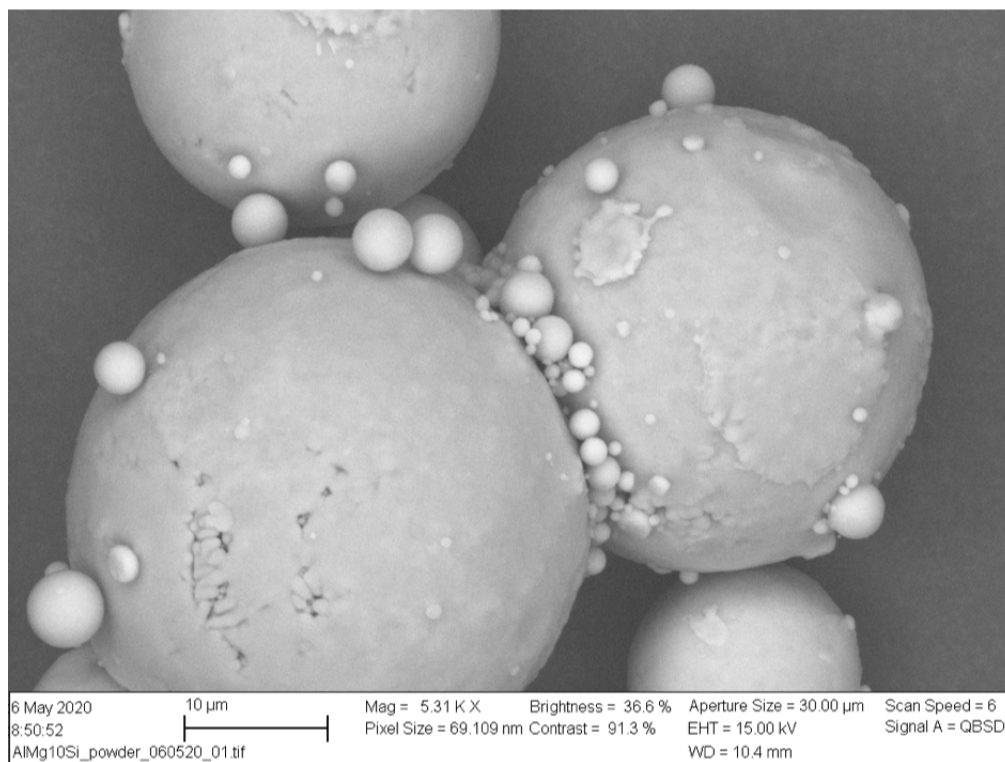
Figure 39: High magnification SEM image of AlSi10Mg powder.

4.2.2 As-printed vertical

A fine cellular-dendritic solidification microstructure of the as-printed specimen is shown in Fig. 40. No apparent signs of melt pool boundaries or heat-affected zones are visible in this specimen. Elongated growth indicating the thermal gradient direction can be observed. Generally, elongated growth are oriented along the building direction.
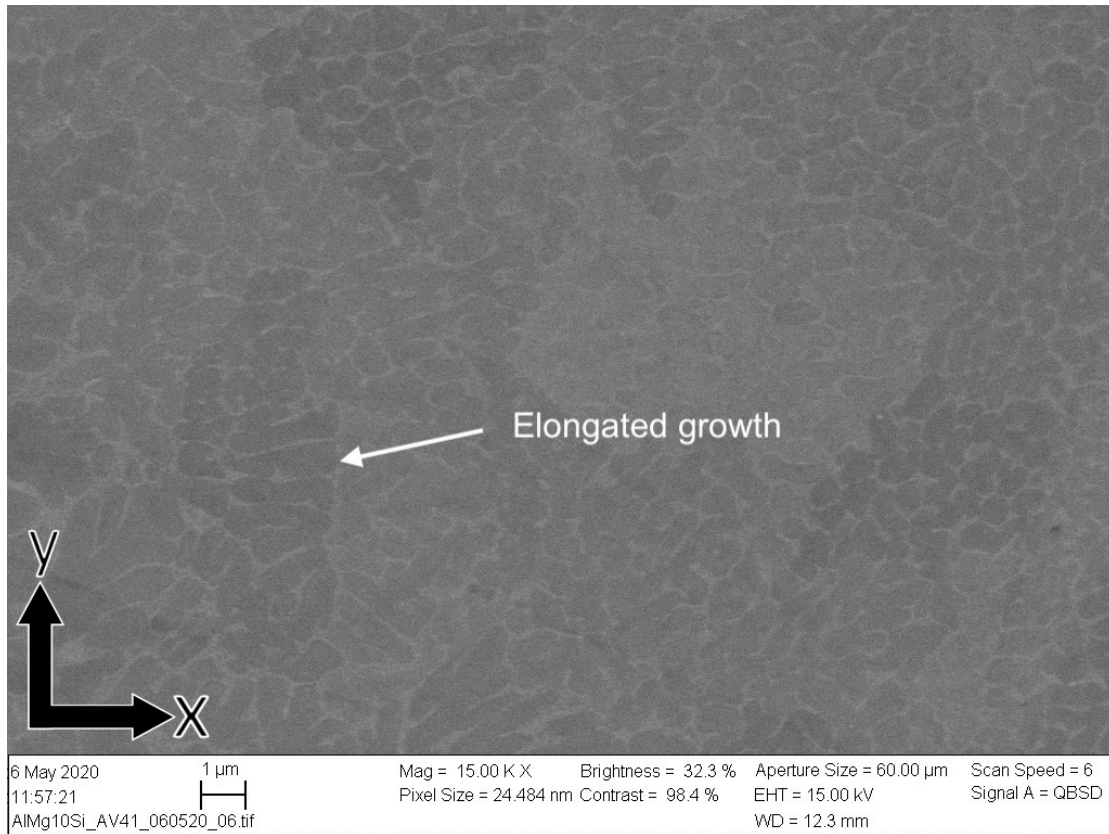
Figure 40: SEM image of the as-printed vertical specimen. Elongated growth are indicated by white arrows.

A small and irregular-shaped pore in the as-printed vertical specimen is shown in Fig. 41. Such a pore likely arise due to unmelted powder, oxides or insufficient overlap of two scan tracks. Oxidized particles or unmelted powder likely got removed by the sample preparations.
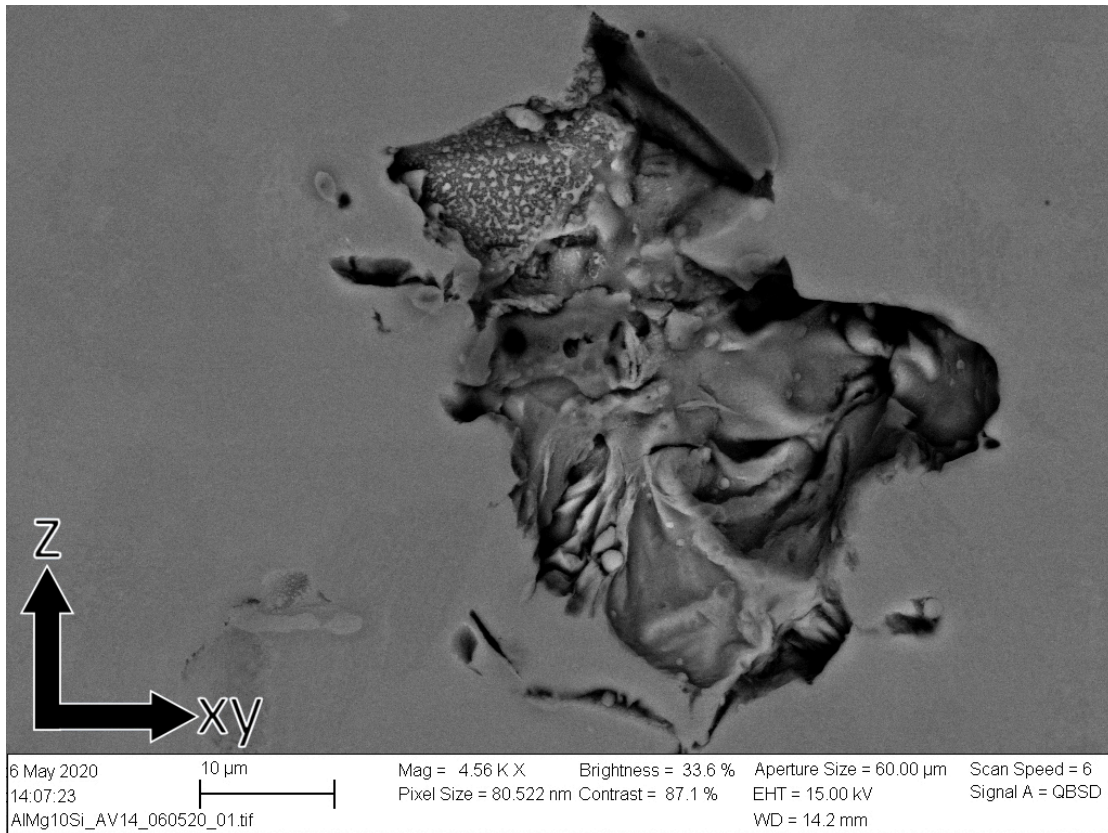
Figure 41: SEM image of an irregular-shaped pore.

4.2.3 As-printed horizontal

Primary α-Al surrounded by a fibrous network of eutectic-Si is shown in Fig. 42. The cell boundaries are made up of eutectic Si and primary aluminium in an alternating fashion. The image resolution is too low to distinguish this alternating pattern clearly but the contours can be observed.
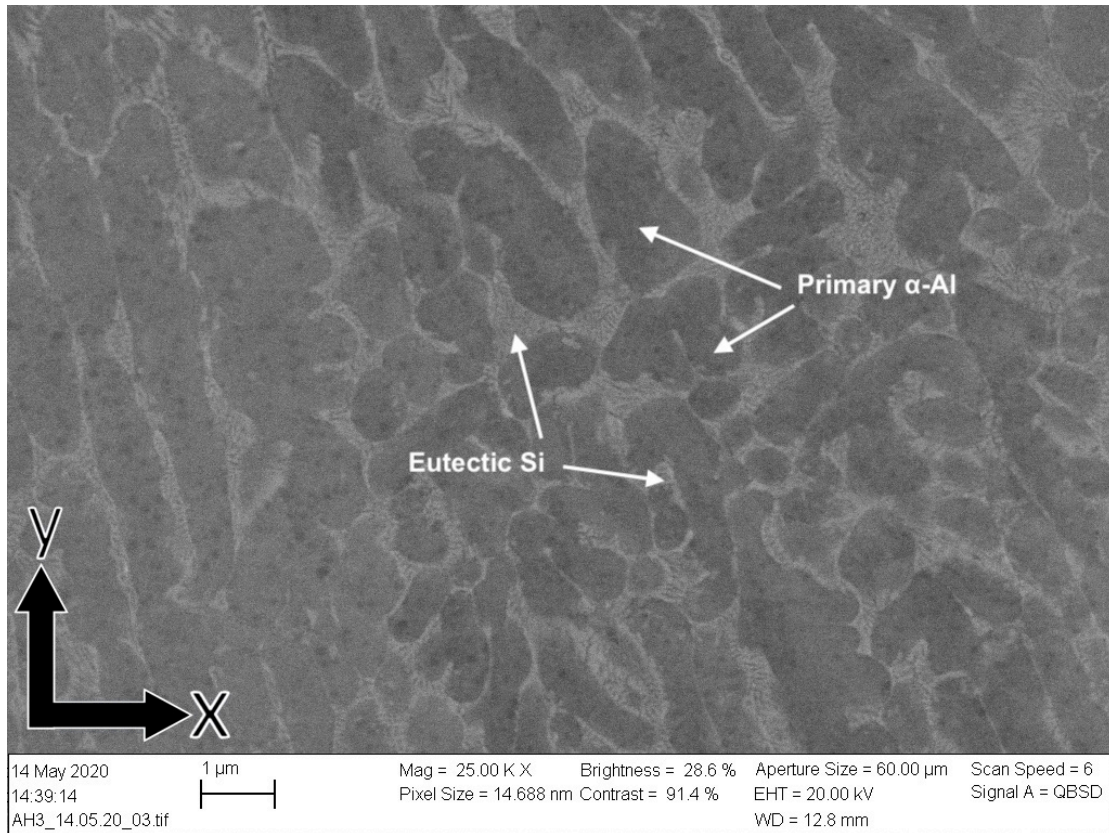
Figure 42: SEM image showing celluar microstructure of the as-printed horizontal specimen. Eutectic Si and primary α-Al shown by arrows in the normal to z-direction.

Fig. 43 (b) shows a spherically shaped pore at the bottom of the image. A bright contrast environs the pore. This indicates that a spherically-shaped particle containing heavier elements may have caused such a pore. Fe elements have diffused from the particle into the surrounding area, and the particle may have been removed during sample preparation.

A relatively small irregular-shaped pore with evenly distributed smaller spherical pores surrounding it is shown in Fig. 44. The irregular shaped pore does not appear to be keyhole pore or fusion defect as it is too small and lacks the flat characteristic seen in those defects. Incomplete powder melting can be observed within this pore. The red arrow points to a bright spot in the image, which is assumed to be a Fe-particle. It is bright as more electrons are backscattered in this area because Fe has a higher atomic number compared to Al, Si and Mg.
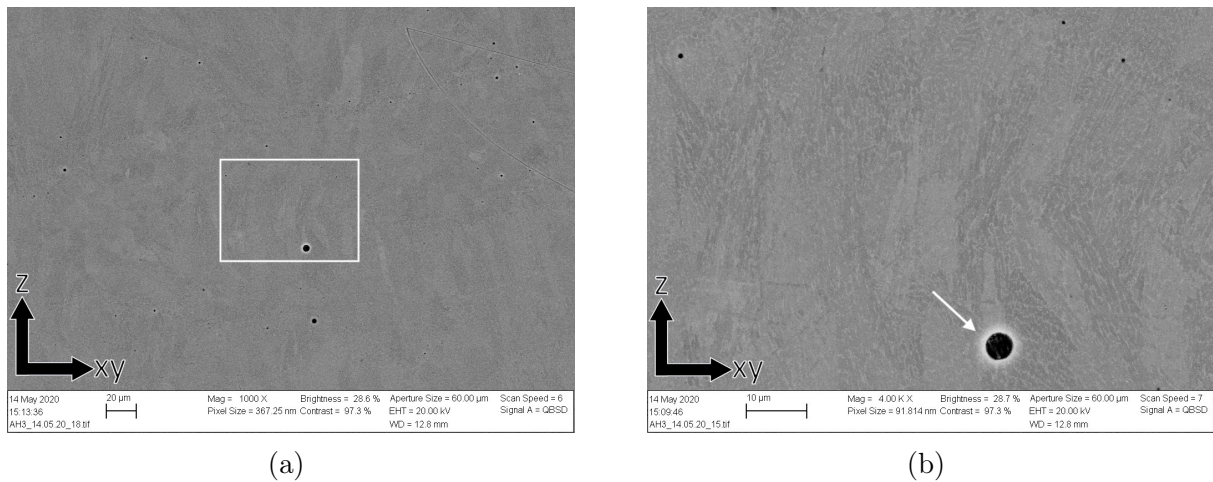
Figure 43: SEM image of a spherical pore in the as-printed horizontal specimen. (b) is a magnified area as indicated by the white box in (a)
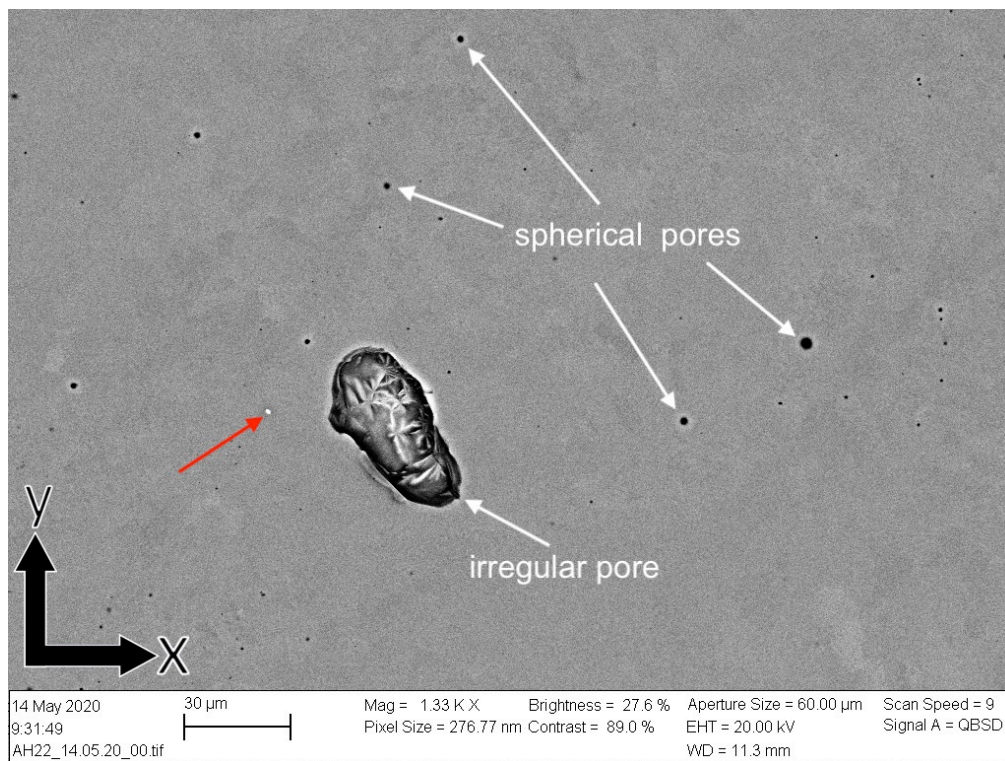
Figure 44: Pores in the as-printed horizontal specimen.

4.3 TEM

It was proved challenging to prepare samples for TEM observations. Several methods were tried and tested, but many turned out the be amorphous. Nevertheless, the TEM images with the highest quality is presented here.

4.3.1 As-printed

The dark areas regions seen in the centre of the peninsula-like shape in Fig. 45 (a) and (b) is eutectic-silicon and the brighter region is pure aluminum. There may also be some aluminium on top or bottom of the dark silicon rich area.

Figure 45: TEM images of the as-printed vertical specimen. (b) is a magnified image of the white box indicated by (a).
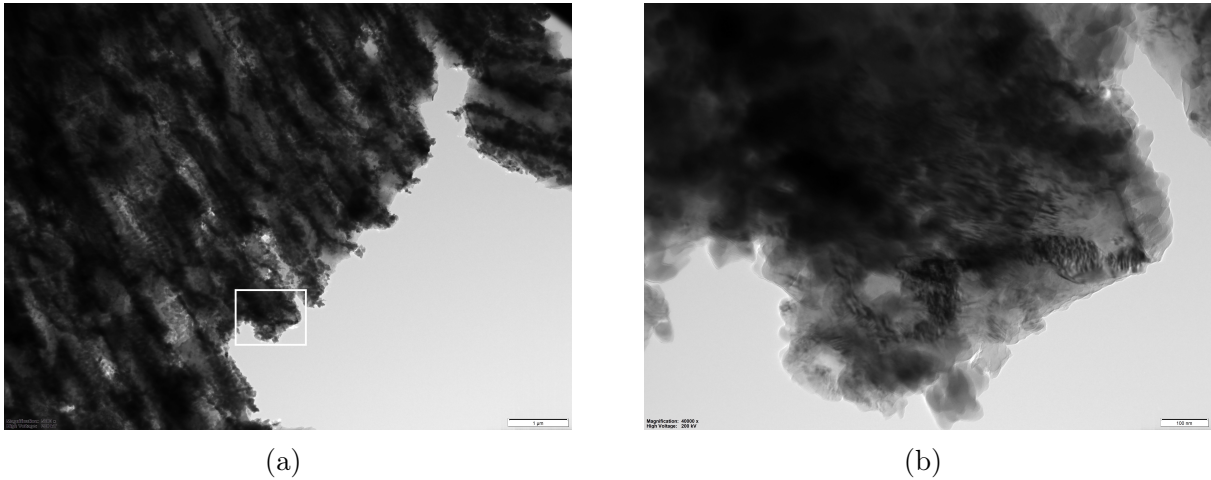
Figure 46: TEM images of the as-printed vertical specimen taken from the middle of the specimen. (b) is a magnified image of the white box indicated by (a).

Some streaks were visible in the specimens, as seen in Fig. 49. These are suspected to be an early stage of GP zones forming. In the same specimen, a diffuse diffraction pattern was observed (see Fig. 50) which indicate a crystalline disorder that may occur when residual stresses are present.
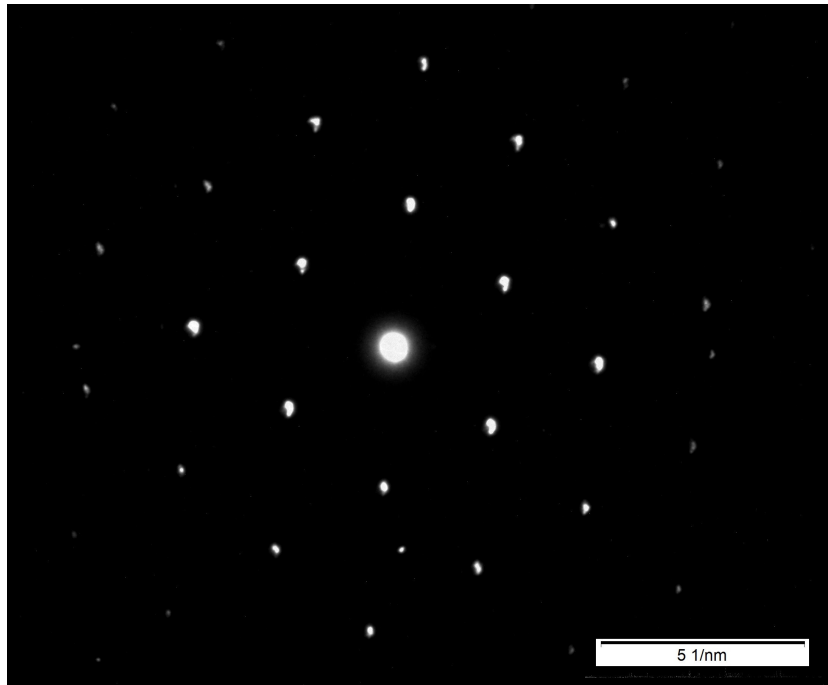
Figure 47: Diffraction pattern from AV3 in the (110) projection.
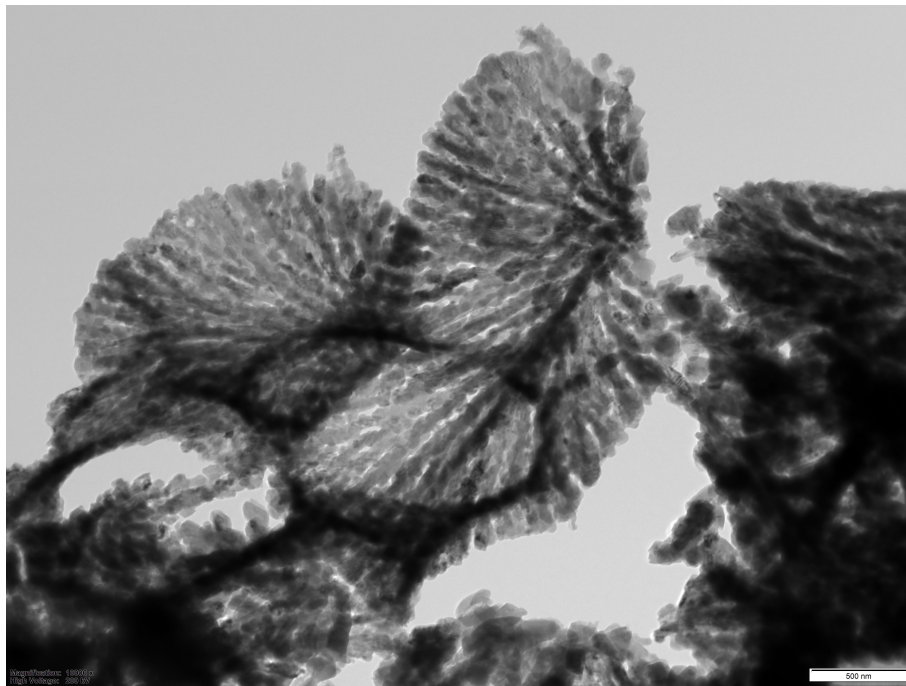
Figure 48: Cell walls visbile in the AV5 specimen.
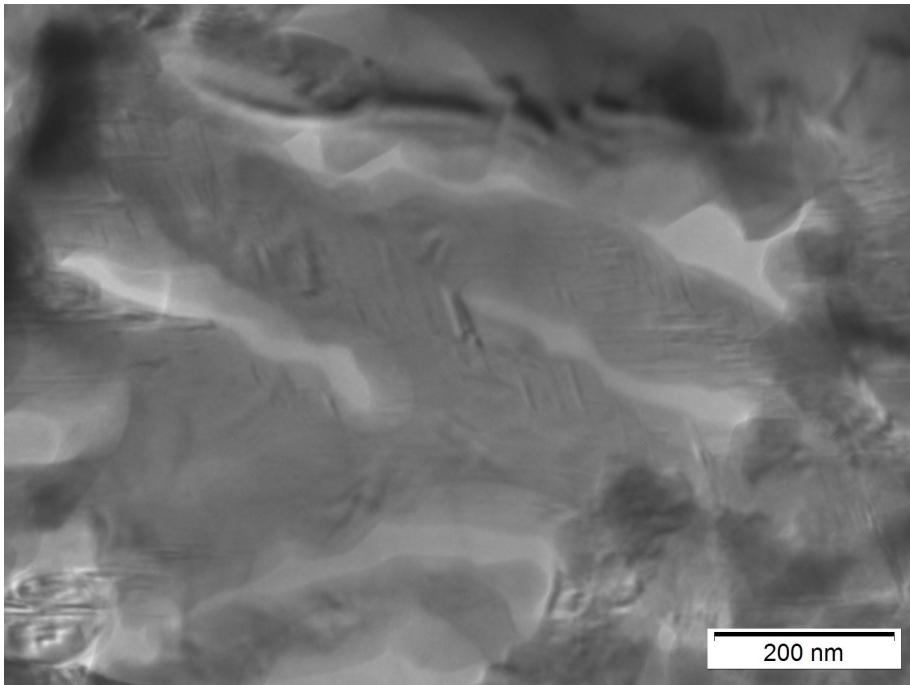
Figure 49: Streaks in the AV5 specimen.
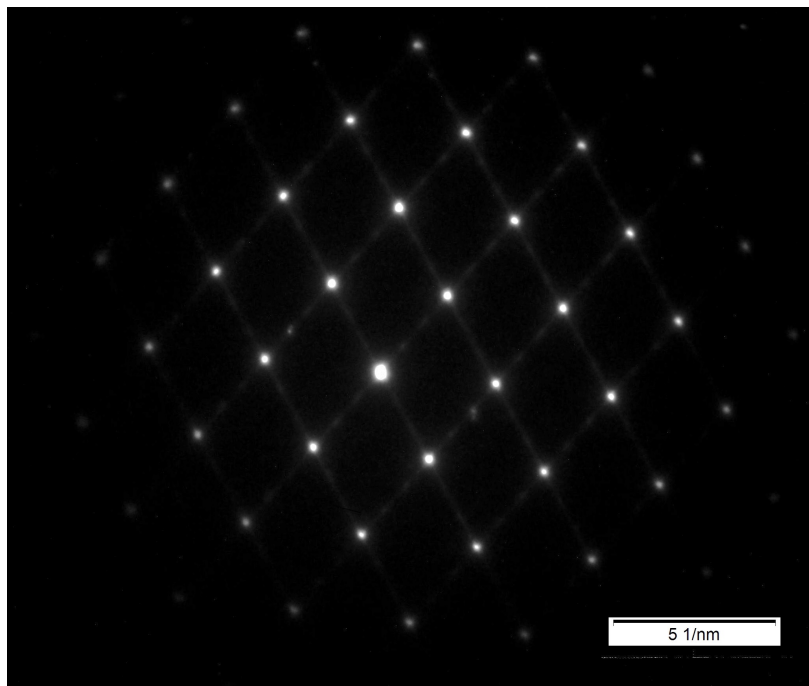
Figure 50: Diffuse diffraction pattern in the (100) projection from the AV51 specimen.

4.3.2 Heat treated

After heat treatment, the fibrous silicon network has been disrupted and the silicon has grown into larger particles. Fig. 51 shows silicon as dark particles and brighter regions which consists of pure aluminium.
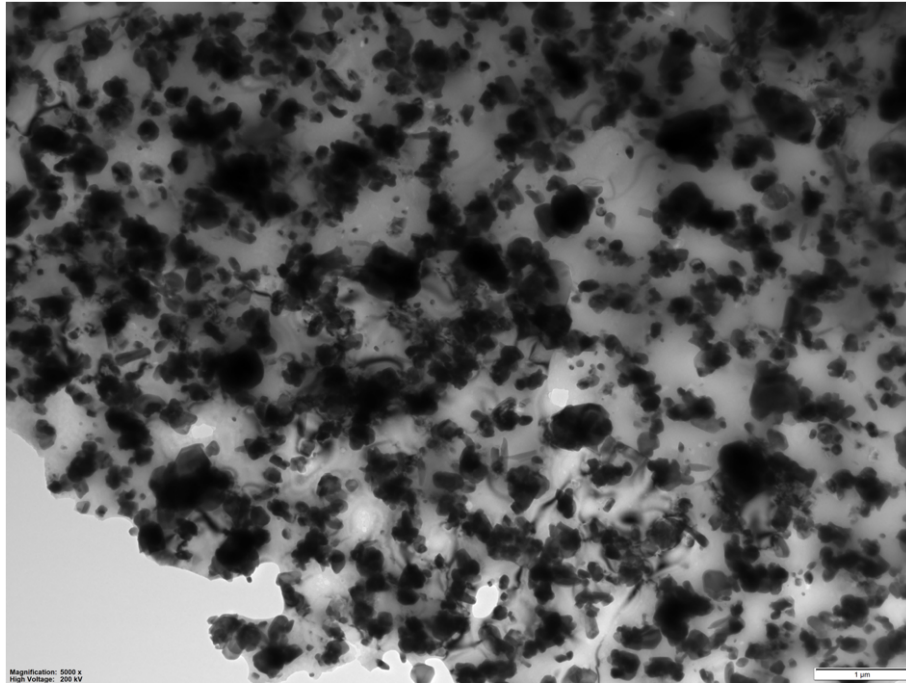
Figure 51: Low magnification TEM image after heat treatment.

Fig. 52 shows the silicon after dissolving from the fibrous network. The dark spherical shapes are eutectic silicon, and the bright is pure aluminium. It is apparent that the silicon has grown into this spherical shape and is not expected to induce any residual stresses in the matrix. The white arrow in Fig. 52 point at what appears to be a Si-particle which may be semi-coherent and therefore contribute to distorting the matrix, leading to residual stresses.

Fig. 53 shows what appears to be pinned dislocations. Fig. 54 is a magnified image of Fig. 53 of the section where the two leftmost arrows were pointed. The dislocations are in a ladder-like arrangement.
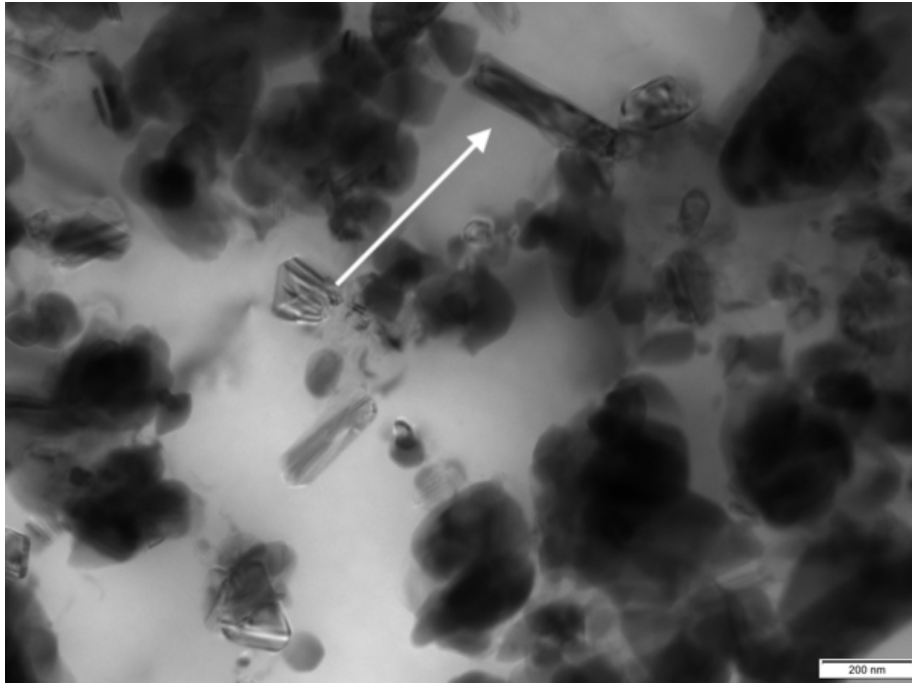
Figure 52: TEM image of heat treated specimen.
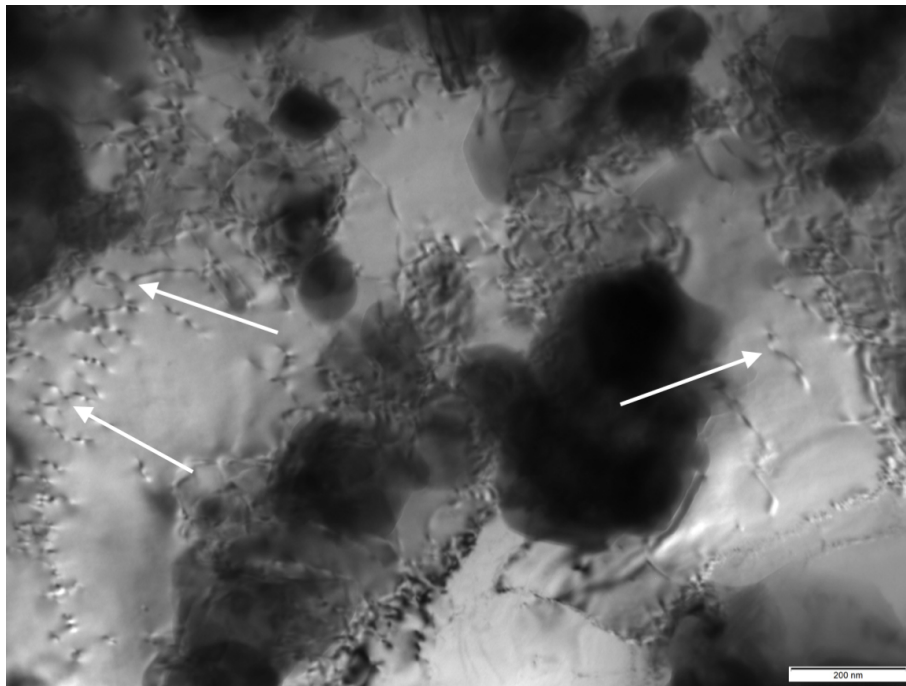
Figure 53: TEM image of dislocations.
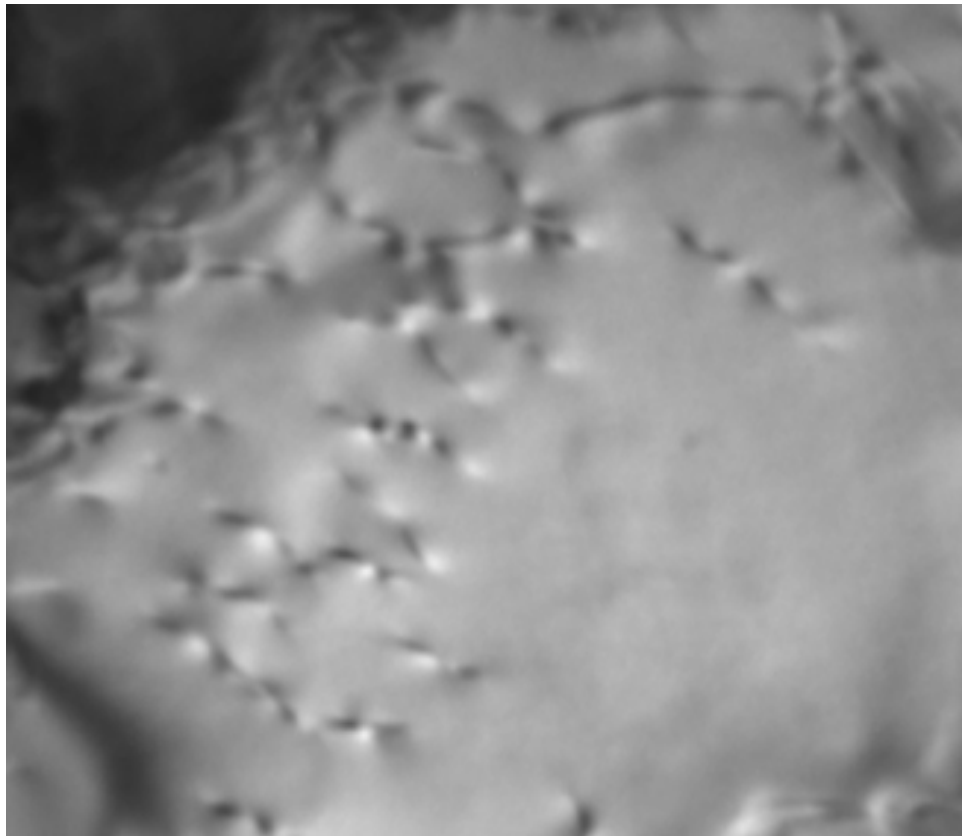
Figure 54: Magnified image of dislocations from Fig. 53

4.4 EDS

EDS analysis was conducted on AlSi10Mg powder, the as-printed vertical specimens and heat treated horizontal specimen.

4.4.1 Powder
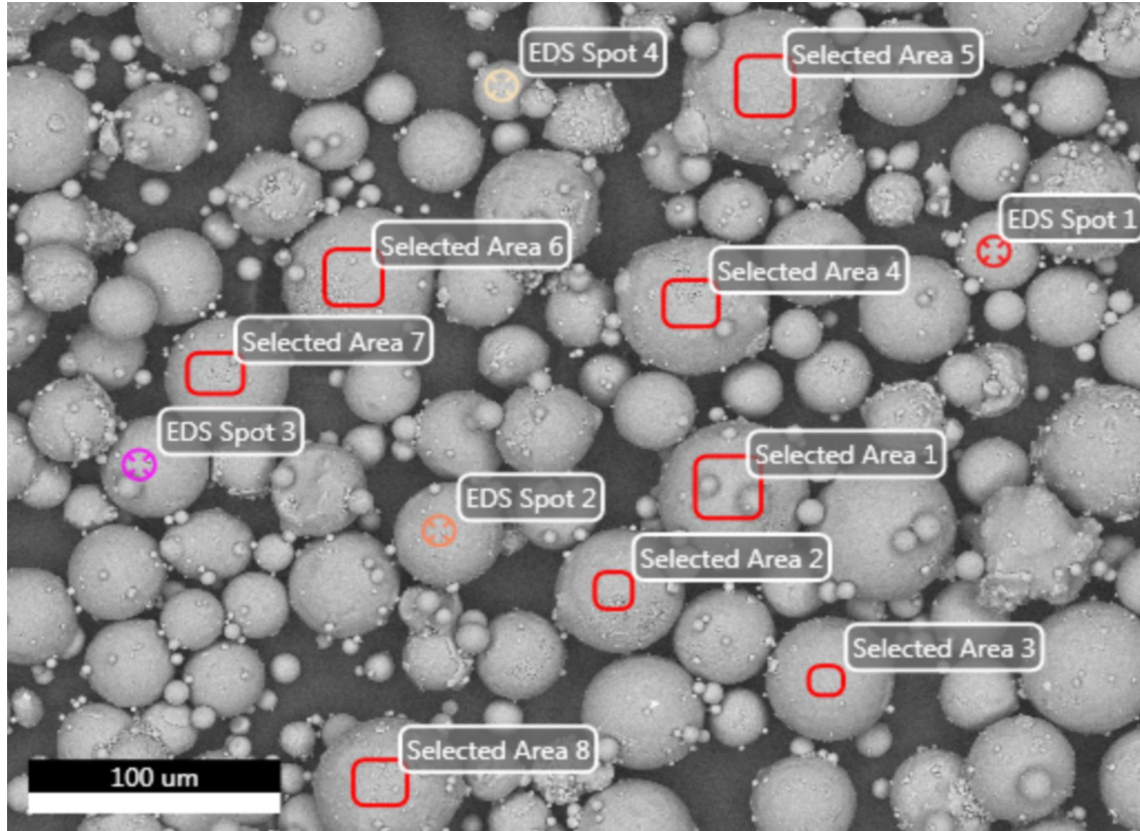
Figure 55: Eight areas and four spots selected for EDS analysis. Results from "EDS Spot 1" and "Selected Area 1 and 5" are presented below.

EDS Spot 1			
Element	Weight %	Atomic %	Error %
O K	0.05	0.09	23.2
Mg K	1.1	1.22	4.98
Al K	91.38	91.51	1.65
Si K	7.47	7.18	8.15

Table 6: EDS analysis result for "EDS Spot 1" from Fig. 55.

The EDS results from the AlSi10Mg powder reveal that the Mg content in the alloy is significantly higher than what is stated in the data sheet where the Mg wt.% is 0.20-0.45. [63]

Selected Area 1				Selected Area 5			
Element	Weight %	Atomic %	Error %	Element	Weight %	Atomic %	Error %
O K	0,32	0,53	16,61	O K	0,25	0,42	19,42
MgK	1,2	1,33	4,7	MgK	1,38	1,53	4,61
AlK	85,88	86	1,71	AlK	88,32	88,38	1,71
SiK	12,61	12,13	7,33	SiK	10,06	9,67	7,59

Table 7: EDS analysis results for "Selected Area 1" and "Selected Area 5" from Fig. 55.

The Mg content vary from 1.1 wt.% to 1.38 wt.% as seen in Tab. 6 and Tab. 7. EDS Spot 1 is relatively rich in Al and Mg and low in Si content. Selected Area 1 and Selected Area 5 has a Si content closer to the expected wt.% as seen in Tab. 7.

Selected Area 1 is an area of a larger particle with two satellites adhered to it. This can be seen in Fig. 55. The EDS results from this area are rich in Si. The EDS from Selected Area 5 is taken at a smoother surface and have a lower Si content. Thus, the EDS results imply that the smaller particles have higher Si content.

4.4.2 As-printed vertical
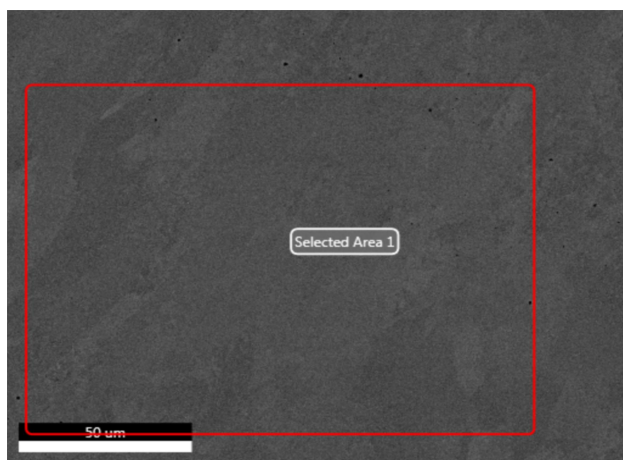
Figure 56: One area selected for EDS analysis from the top part of the as-printed vertical specimen.

Selected Area 1 from Fig. 56, has a high Mg and below eutectic Si content.

The EDS of Area 1 from Fig. 57 are taken on the cell wall. The Si content in this area is high. Close to the eutectic composition of an Al-Si alloy system (12.6 wt.%). The EDS of Area 2 is taken inisde a cell and have a high Al content combined with a lower Si content compared to Area 1.

	Selected Area 1		
Element	Weight %	Atomic %	Error %
O K	0.01	0.02	10.91
MgK	1.20	1.33	2.25
AlK	89.86	90.05	1.52
SiK	8.93	8.59	6.32

Table 8: EDS analysis result for "Selected Area 1" from Fig. 56.
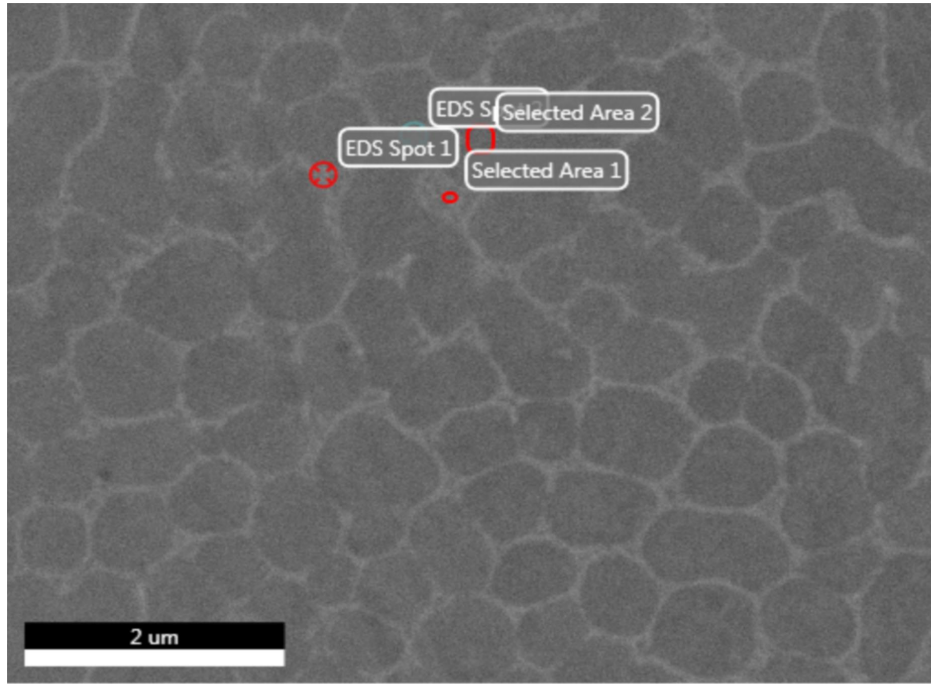
Figure 57: Two areas and two spots selected for EDS analysis. Results from "Selected Area 1" and "Selected Area 2" is included here.

	Selected Area 1				Selected Area 2		
Element	Weight %	Atomic %	Error %	Element	Weight %	Atomic %	Error %
O K	0.20	0.35	15.72	O K	0.12	0.20	15.82
MgK	1.27	1.42	3.60	MgK	1.24	1.37	3.59
AlK	84.48	84.71	1.63	AlK	90.43	90.52	1.59
SiK	14.04	13.52	6.58	SiK	8.21	7.90	7.23

Table 9: EDS analysis results for "Selected Area 1" and "Selected Area 2" from Fig. 57.

4.4.3 Heat treated horizontal

Selected Area 1 and Selected Area 2 from Fig. 58 are taken from the bright area which was previously a part of the fibrous Si network. Selected Area 1 has a close to eutectic composi-
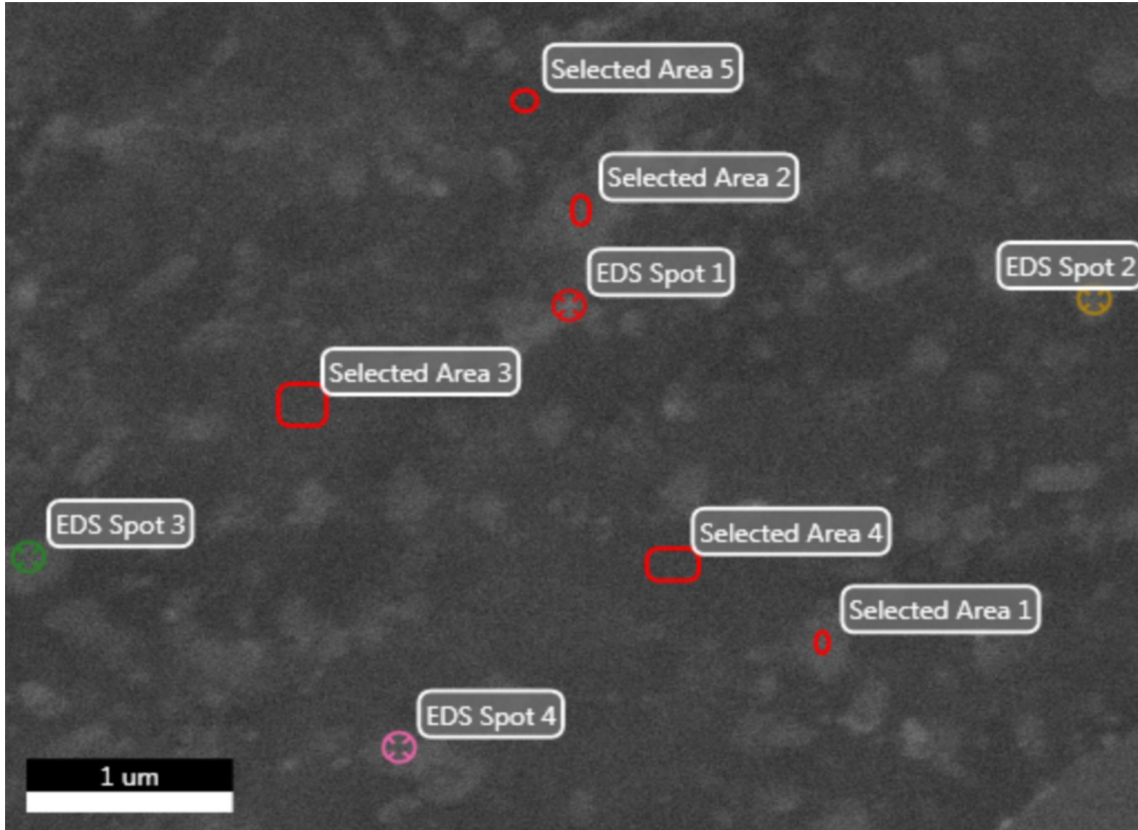
Figure 58: Five areas and four spots selected for EDS analysis. Results from "Selected Area 1 and 2" and "Selected Area 3 and 5" are included here.

tion but Selected Area 2 has a significantly reduced Si content. For Selected Area 4 and 5, the Si content is relatively low.

	Selected Area 1				Selected Area 2		
Element	Weight %	Atomic %	Error %	Element	Weight %	Atomic %	Error %
MgK	1.17	1.31	3.50	MgK	1.15	1.27	3.68
AlK	86.20	86.56	1.35	AlK	91.41	91.59	1.31
SiK	12.56	12.11	7.79	SiK	7.40	7.12	8.51
AgL	0.07	0.02	88.38	AgL	0.05	0.01	96.85

Table 10: EDS analysis results for "Selected Area 1" and "Selected Area 2" from Fig. 58.

Selected Area 3				Selected Area 5			
Element	Weight %	Atomic %	Error %	Element	Weight %	Atomic %	Error %
MgK	1.09	1.21	3.71	MgK	1.13	1.26	3.49
AlK	90.65	90.85	1.30	AlK	90.44	90.65	1.31
SiK	8.24	7.94	8.34	SiK	8.40	8.08	8.33
AgL	0.02	0.00	94.06	AgL	0.03	0.01	99.99

Table 11: EDS analysis results for "Selected Area 3" "Selected Area 5" from Fig. 58.

4.5 EBSD

4.5.1 As-printed vertical

EBSD of the as-printed vertical specimen (AV5) on the xy-surface is presented. The average grain size was measured to be 16.2 μm. Fig. 63 shows the grains that were selected by the were selected by the software. Melt pool borders are visible in the y-direction. Elongated grains can be observed in the direction of the scan track. The majority of grains have a misorientation angle <5°.
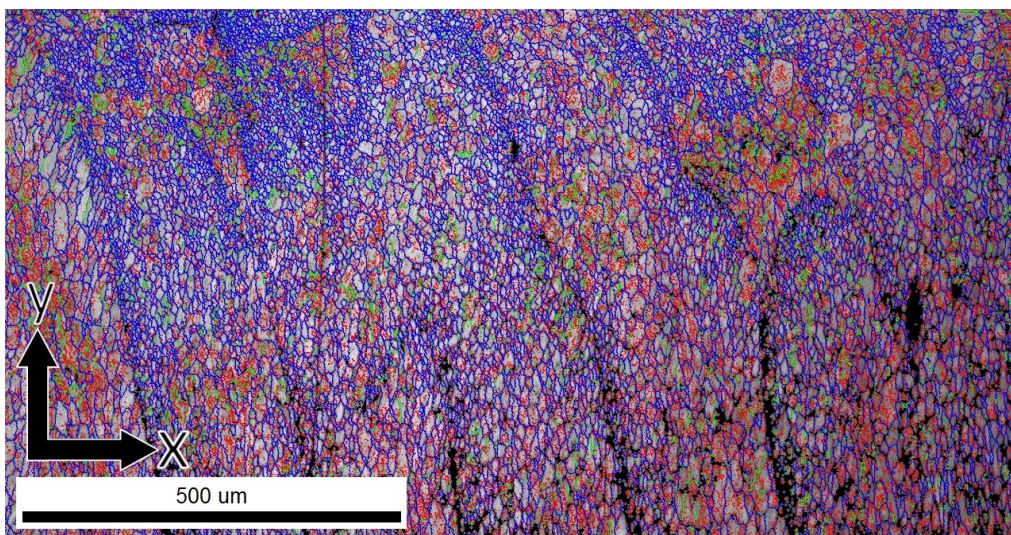
Figure 59: Grain and grain boundary selected software for the as-printed vertical specimen on the xy-plane.
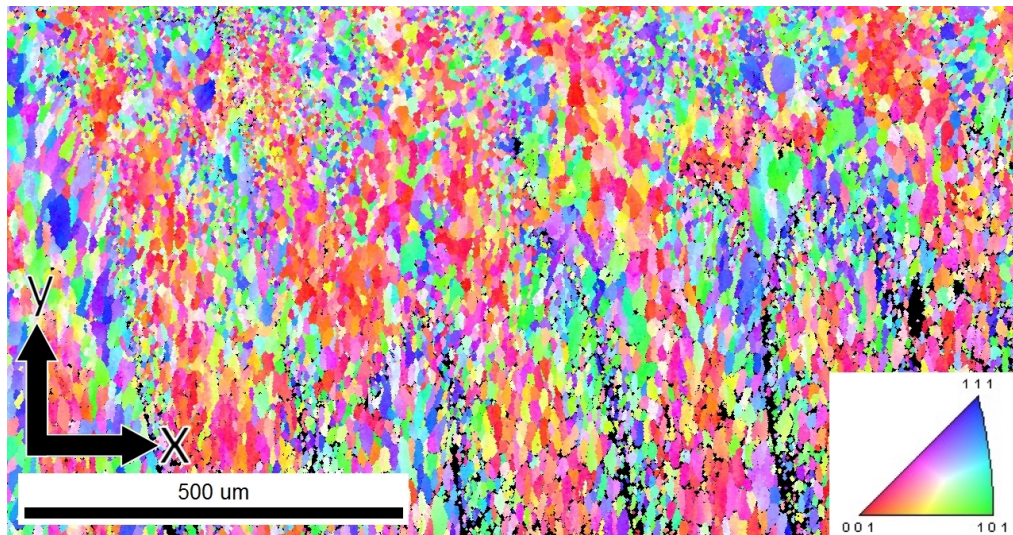
Figure 60: Inverse pole figure orientation map for the as-printed vertical specimen on the xy-plane.

(a)

(b)
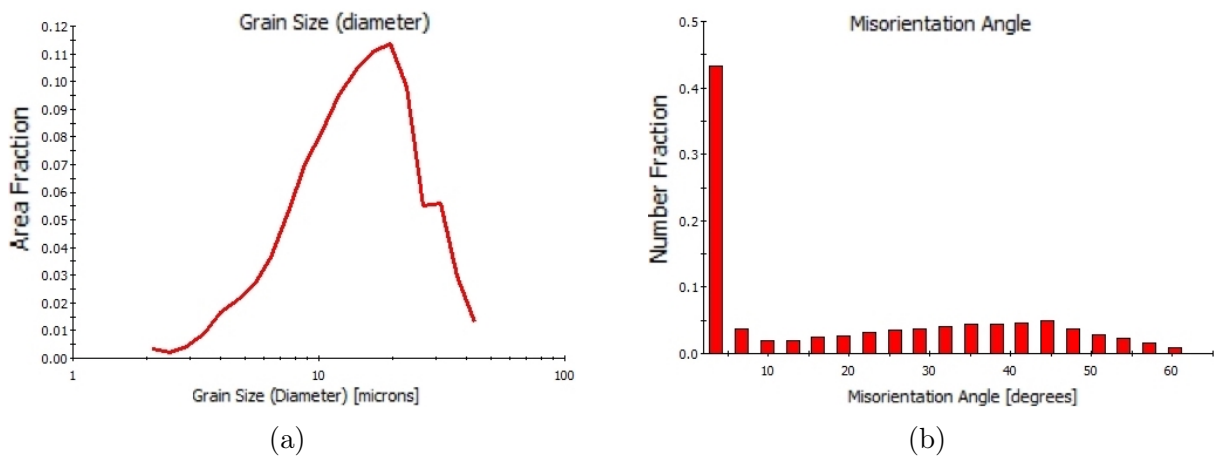
Figure 61: (a) showing grain size distribution. (b) showing misorientation angle.

4.5.2 As-printed horizontal

EBSD of the as-printed horizontal specimen (AH3) on in normal to the z-direction is presented. The average grain size was measured to be 33.2 μm. Fig. 62 shows the grains that were selected by the were selected by the software. Larger grains compared to the vertically printed specimen can be observed. Melt pool borders can not be observed. The majority of grains have a misorientation angle <5°.
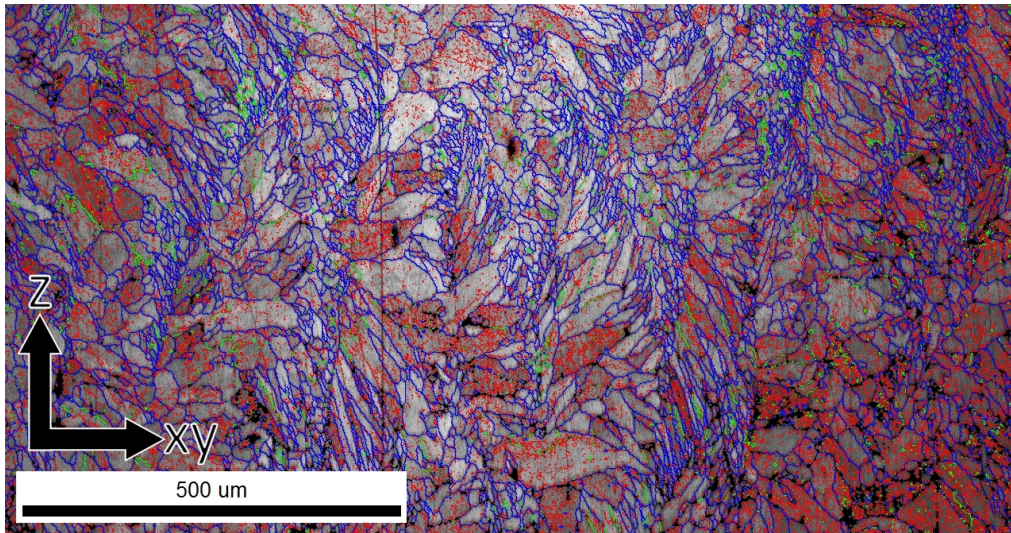
Figure 62: Grain and grain boundary selected software for the as-printed horizontal specimen in normal to the z-direction.
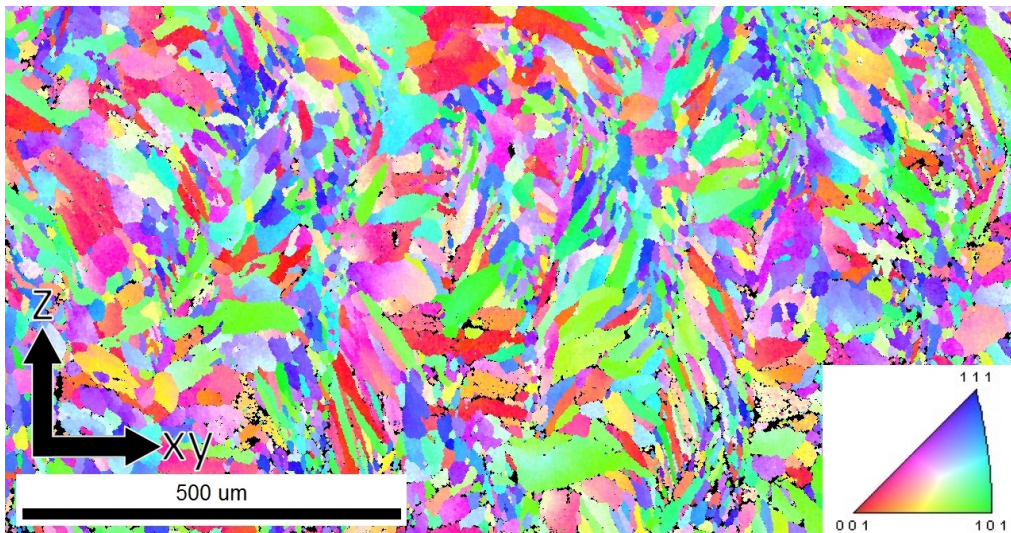
Figure 63: Inverse pole figure orientation map for the as-printed vertical specimen in normal to the z-direction.
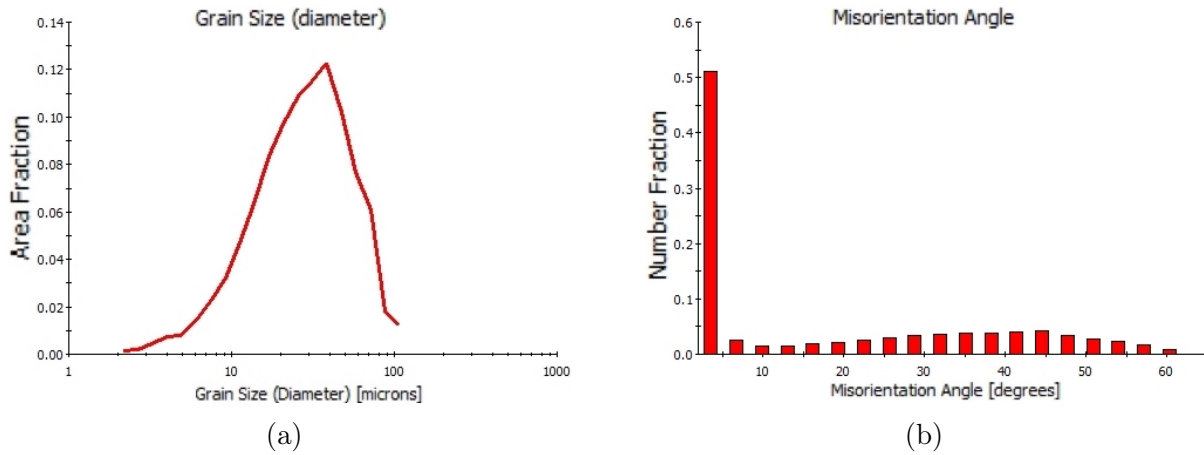
Figure 64: (a) showing grain size distribution. (b) showing misorientation angle.

4.6 Hardness

The hardness for the horizontal specimens is in the range of 121 $HV_{0.2}$ and 145 $HV_{0.2}$. The average hardness measurements for the five speciemns in the horizontal direction have somewhat consistent values. This can be seen in Fig. 65 (a). Fig. 65 (b) illustrates that for the vertical specimens it is evident that there is a reduction in the measured hardness as the printing process proceeds. For the the specimens closer to the bed the measurements range from 131 $HV_{0.2}$ to the highest measured value at 142 $HV_{0.2}$.
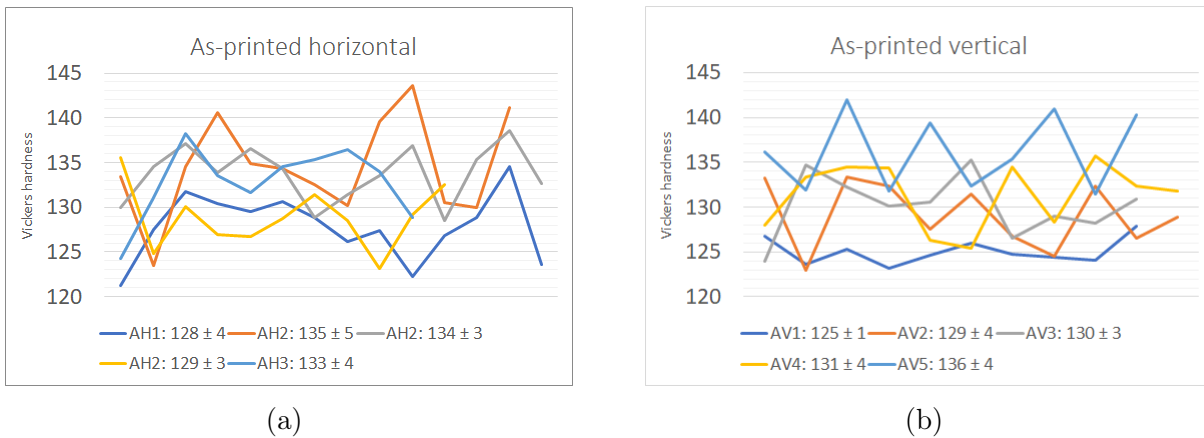
Figure 65: Chart (a) showing the hardness values for the as-printed horizontal specimens and (b) for the as-printed vertical specimens.

After heat treatment there is approximately a 50% hardness reduction. This is a significant drop in hardness to achieve a higher ductility.

There is no significant discrepancy in the hardness of the as-printed cube compared to the as-printed rods. For the heat treated cube, the top and middle part of the sample seem to be slightly harder.
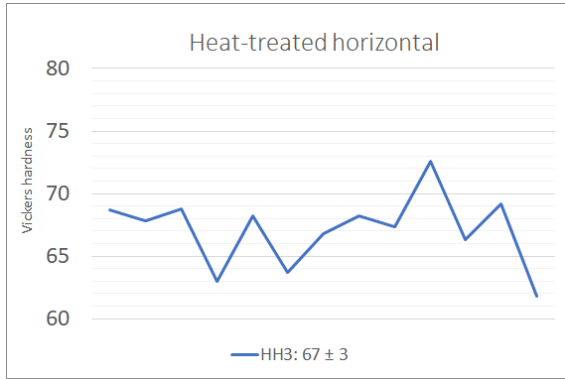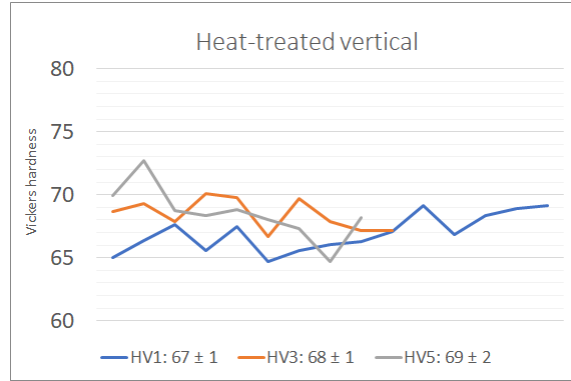
Figure 66: Chart (a) showing the hardness values for the heat treated horizontal specimens and (b) for the heat treated vertical specimens.
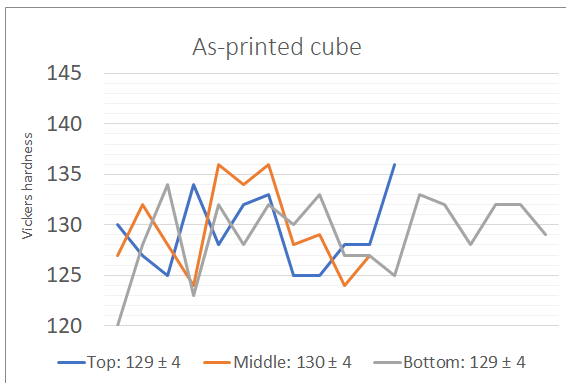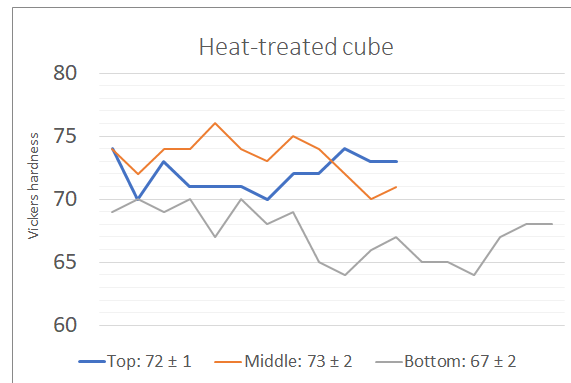
Figure 67: Chart (a) showing the hardness values for the as-printed cube and (b) heat treated cube.

4.7 Residual stress

Sample	a / Å (a_{bulk} = 4.0496 Å)	ϵ (WH)	ϵ (HW)
AlSi10Mg powder	4.050956	6.158854×10^{-4}	6.734666×10^{-4}
As-printed bottom	4.04501	4.678289×10^{-4}	5.822877×10^{-4}
As-printed middle	4.042243	-8.158804×10^{-4}	-7.006919×10^{-4}
As-printed top	4.031591	-7.694709×10^{-4}	-6.809593×10^{-4}
Heat treated bottom	4.044347	3.751201×10^{-4}	4.100740×10^{-4}
Heat treated middle	4.048013	4.559653×10^{-4}	5.045411×10^{-4}
Heat treated top	4.039783	4.002646×10^{-4}	4.494028×10^{-4}

Table 12: Presentation of the strains measured by Williamson-Hall and Halder-Wagner approach.

There are tensile residual stresses in the bottom of the as-printed cube and compressive stresses in the middle and top part of the cube. A negative slope indicates compressive residual stress and positive slope indicates tensile residual stresses for the WH approach. After heat treatment, the calculations show that there no longer are compressive stresses and the stresses has been reduced.
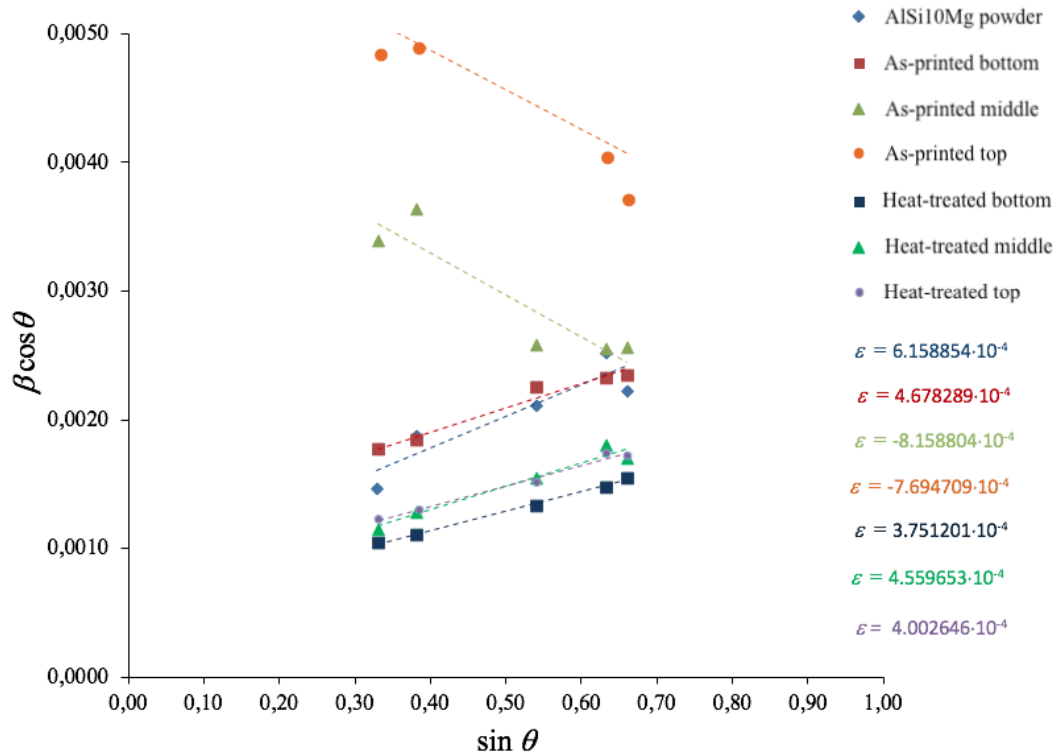
Figure 68: Residual stress calculated using the Williamson-Hall approach.
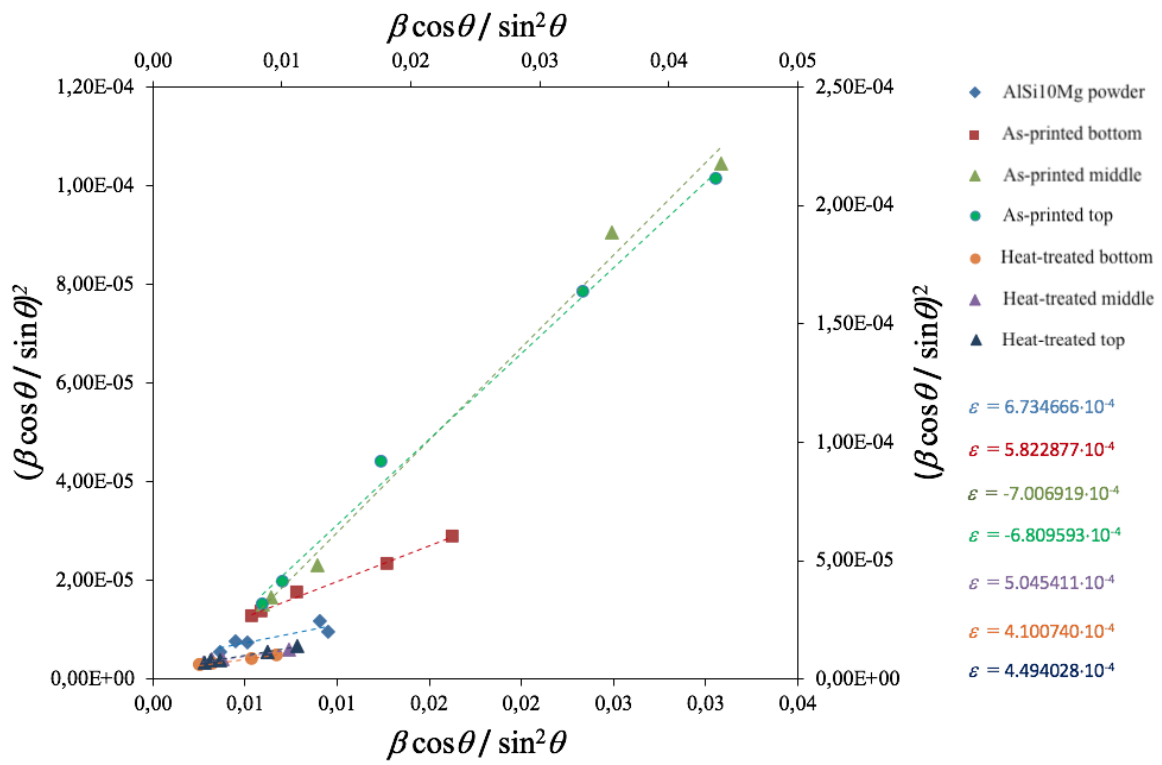
Figure 69: Residual stresses calculated using the Halder-Wagner approach.

5   Discussion

In this chapter, the findings of the experimental work will be considered with the theory in chapter 2. As the experimental work was not performed by the author, the methodology will not be discussed in this chapter. Nevertheless, the process parameters used for building the specimens will be mentioned.

5.1   Macrostructure

The printed specimens displayed the characteristic SLM macrostructure as previously described in the literature [7], [27], [13], [64], [65], where the traversal melt pools have a half-cylindrical shape in a fish-scale-like pattern, and the layers normal to building direction is made up of longer melt pools. The micrographs in the normal to the building direction showed fractioned scan tracks. The reason for this is as explained earlier; the sample preparation is not parallel to the layer. The optical micrographs taken in the cross-sectional view of the melt pools showed a sufficient overlap between the melt pools as seen in Fig. 32. The spot size and hatch spacing is 75 - 80 μm and 170 μm, respectively. The large hatch spacing compared to the spot size would leave a gap between the scan tracks, but due to the high thermal conductivity dissipating heat to the adjacent areas, the melt pools are larger than the spot size. The overlap ensures a good intralayer connection.

The depth of the melt pool is also an important factor to ensure an established interlayer connection. The fish-scale-pattern shown in Fig. 24 and more clearly in Fig. 31 (a) depicts how the melt pools slightly penetrate the layer below. Appropriate penetration through layers are attained at E′ values 140 - 160 J m^{-1}. [7] The process parameters used for building specimens in this study gave an energy input per unit length equal to 304 J m^{-1}. This is well above the recommended E′ values given by Kempen et al. [7] When E′ is too high, the melt pool penetrates too deeply, and element evaporation may take place. However, very few signs of keyhole mode were found in this study, but Fig. 36 depicts a melt pool with a depth greater than two layers which indicates that this scan track has transitioned from conduction to keyhole mode. The recommended value range for E′ reported in the literature can hence be questioned.

Angle measurement was performed on the melt pools in the normal to building direction to measure the layer rotation. The angles vary from 64 to 69°, which is assumed to be sufficient. The discrepancy from the set value of 67° could arise from the measurements being performed on melt pools and not the actual movement of the laser. Therefore it is an indirect way of measuring the angle. Also, the sample preparation might not be perfectly parallel to the layers investigated, but this would only cause very little angle change as the measured melt pools are considered to have a sufficient length for measurements. The stress-relief heat treatment performed had no apparent effect on the structure of the sample on the macro level.

5.2 Microstructure

The microstructure of the as-printed SLMed AlSi10Mg samples showed a fine cellular-dendritic structure with some elongated growth oriented along the building direction. The cell walls consisted of a fibrous network of eutectic Si, as seen in Fig. 42. The rapid and directional solidification leads to the fine microstructure. The borders of the melt pool showed a coarser microstructure. These areas remain at an elevated temperature as the laser remelted these areas when scanning adjacent tracks. The centre of the melt pool reaches the highest temperatures and decreases towards the boundaries. This results in high cooling rates leaving fines cells at the centre of the melt pool.

The microstructure is determined by the thermal gradient G and the growth rate R. The inherently moving heat source in the SLM process gives varying G and R for the melt pool. The centre of the melt pool has the highest thermal gradient and growth rate and conversely at the borders. The morphology of the as-printed solidification structure does not change in the sample, meaning that the G/R is constant. But the size of the solidification structure, the product of G and R, does. The melt pool boundaries can be described as having lower value for the product of G and R.

The cells are characterised as a subgrain structure. A grain is defined as a group of proximate cells grown in the same crystallographic direction. The EBSD showed the grain structure of the as-printed vertically and horizontally specimen in the xy-direction and normal to the z-direction, respectively. The average grain size in the xy-plane was half of the ones in the normal to the z-direction.

OM images of the traversal cross-sections showed epitaxial growth which is reported to occur where the heat flow direction is along the (100) direction of the substrate. The OM images showed less epitaxial growth in the heat treated samples. This microstructure is narrow so they might get disrupted by the heat treatment. Unfortunately, in this study, there were no recorded SEM images received of the microstructure of the heat treated specimens. Nevertheless, the image from EDS results (Fig. 58) showed the disrupted Si network and globular Si particles had formed.

The AlSi10Mg alloy has approximately a eutectic composition of Al-Si system (12.6 wt.%) The spectroscopy results showed the chemical composition at the cell boundaries to be close to the eutectic for an Al-Si alloy system. Inside the cells, the composition was higher in Al and lower in Si content. The Mg content was similar to inside the cells.

Due to the high growth rate and high temperature gradients, a dislocation network was highly expected to be found in the TEM images of the as-printed specimens. However, no dislocation network was found. It is suspected that there are dislocations present and that the sample preparation was insufficient to make them visible in the TEM. However, some dislocations in a ladder-like arrangement were found in the heat treated specimens investigated by TEM. These dislocations seemed to be pinned by what is suspected to be Mg_2Si precipitates. This is difficult to determine at this magnification and without EDS elemental

maps. Nevertheless, the dislocations showed a resemblance to the Mg_2Si pinned dislocations found by Hadadzadeh et al. [66] The movement in the slip plane is hindered as the dislocations struggle to cut through and bow around the precipitates and thus the material strength is increased.

Some narrow streaks were observed in the TEM images, see Fig. 49. It is suspected that these are some early formation precipitates or clusters of the alloying elements as described in chapter 2.6. The streaks were oriented in (100) directions and the diffraction pattern in this projection showed diffuse diffraction. The diffuse diffraction pattern indicates lattice strain, meaning that there are residual stresses present. The formation of the streaks could arise from repeatedly heating of the material, causing some of the Si and Mg to go into solution and later diffuse as the temperature was decreased. These formations are suspected to be hardness increasing as they were found at the bottom of the vertically built specimen (AV5), where the highest hardness was measured.

Si particles with a flat shape were found in TEM images as shown Fig. 52 which had similarities to particles found by Zhou et al. [14] These flat particles are suspected to be semi-coherent and induce lattice strains. The Si particles could be seen in the TEM images to have been growing.

Some smaller spherical and some irregular-shaped pores were found. No large pores (>100 μm) were found. Most of the pores depicted by SEM had a bright area surrounding it, suggesting that heavier elements were present in those areas. The small spherical pores were less than 10 μm in size and are suspected to arise from gas trapped in powder. The EDS results suggest little to none evaporation of Mg comparing results from the powder and as-printed. Evaporation of Mg in the AlSi10Mg is known to cause pores. [7] Thus, hydrogen is suggested to be the reason for the formation of pores. As mentioned before the solubility of hydrogen in the liquid aluminium is higher than in solid by a factor of 22. The hydrogen diffuses out of solution as the aluminium solidifies creating pores. Pores are detrimental to the material strength as they can act as notches initiating micro-cracking. No other defects were found in the specimens investigated by OM and SEM.

SEM images of the RF-PS processed AlSi10Mg powder showed a spherical morphology with some irregularities. The morphology along with the particle size distribution is the most essential characteristics for SLM powder. [67, p. 54] The powder used in this study showed a superior morphology compared to powder depicted in the literature. [7][8][9]

The powder is one of the predominant factors for how a SLMed part will behave mechanically. The powder processability is determined by particle shape, particle size distribution, chemical composition, absorptivity, melting temperature and thermal conductivity. Powder to be used in an SLM process should be spherically shaped to ensure good flowability. The flowability is important to attain an even dispersion of powder on the build platform. The particle size distribution should consist of a wide range of particle sizes to ensure high density. [67, p. 54] However, if the majority of the powder is small particles, the strong Van der Waals force will cause these to conglomerate. Larger particles require more energy to

69

be completely melted because they have a larger volume. No particle size distribution were made in this thesis. The lack of defects detected by OM and SEM in the material indicates that the RF-PS AlSi10Mg powder used was adequate for SLM production.

5.3 Residual stress

The XRD data were used for calculating strain using WH and HW approach. The residual stresses at the bottom of the as-printed cube gave an incongruous value. This value was closer to what was found in the cube that had gone through stress-relief heat treatment. Residual stress values are known to be oscillating and have previously been shown to be tensile at the bottom of samples. [18] However, in the hardness test, the highest hardness numbers were found at the bottom of the vertically printed sample. Therefore, it was expected that high residual stresses would be found at the bottom of the cube. As compressive residual stress is known for increasing hardness. [68]

The sample preparation may cause the deviant value. It is suspected because the bottom of the cube was attached to the support structure which was required to be removed. During this removal of support structure, deformation may occur causing residual stress to be changed. Lower stress values after part removal have been reported in the literature. [20]

Using the Young's modulus from the AlSi10Mg data sheet (80 GPa) and the strain from the WH approach gives approximately 65 MPa in compressive stress for the as-printed cube with the exception of the bottom part. The residual stresses in the heat treated cube is approximately 30 MPa in tensile stress. All of these values are well below the yield strength.

5.4 Hardness

The results from the Vickers hardness test showed a varying hardness in the building height. For the as-printed vertical specimen, the hardness at the bottom sample was roughly 9% higher than the hardness at the top specimen. This is contrary to the results from Maamoun et al. found. [64] The sample used by Maamoun et al. was only 10 mm height, and it was suspected that the difference in hardness could arise from microstructural inhomogeneity inside each melt pool. The difference in hardness in relation to the building height was initially thought to arise from residual stresses. However, the XRD data showed residual stresses at the bottom of the as-printed cube to be similar to what was found in the heat treated cube. Therefore, additional hardness testing of the cubes was performed, which also gave values in the lower ranges. However, as the residual stress for the as-printed specimen was similar to the heat treated one, the hardness should also be significantly lower. The reason for this is unclear and need more investigation.

After heat treatment, the hardness number for the horizontally and vertically built specimen were indistinguishable. The reason for this is caused by the disruption of the fibrous Si-network. Compared to the as-printed specimens, the hardness number for the heat treated

specimens exhibited a 50% drop in hardness. As there is a strong correlation between hardness number and yield strength, there is expected to be a reduction in yield strength for the heat treated specimens.

5.5 EDS

The EDS results showed that the cell boundaries in the as-printed specimen had a composition close to the eutectic for a Al-Si alloy system. The Mg content of all of the investigated areas (powder, as-printed and heat treated specimens) was much higher than the 0.20-0.45 wt.% given in the datasheet.

The heat treated samples exhibited a similar chemical composition to the as-printed ones the the microstructure was changed. Two measurements were presented in the areas where the fibrous Si-network had been dissolved, and globular shaped particles had formed. These areas exhibited a strangely varying Si content. For Area 1 the composition was near eutectic and in Area 2 had a Si wt.% near 7, as seen in Tab. 10. Area 2 is expected to have a higher Si content meaning that some of the Si must have diffused out of the area. The EDS results from the inside the cells in the as-printed specimen and corresponding area in the heat treated specimens have a similar chemical composition.

No signs of evaporation of lighter elements were found in the EDS results. The high scanning speed prevented the temperature in the melt pool to exceed the boiling point when a high laser power. No evaporation of Mg has been reported previously in the literature. [69] This is also supported up by the fact that no laser spatter was found which only occurs when the temperature has exceeded the boiling point.

5.6 Process parameters

The received samples showed few signs of porosity. No keyhole pores were found, but some small spherical pores were found. The powder and building environments are thus suspected to have low moisture.

The low amount of observed pores is also attributed to the high laser power and high scanning speed. The high laser power transmits enough energy to break down any oxides that may have formed, and the high scanning speed prevents the keyhole mode welding. Such particles are flat and have an irregular shape but were not observed in this study. However, high laser power is a double-edged sword as laser spatter can occur. But no laser spatter was detected in the samples. The samples showed no signs of balling, shape distortions or cracking either.

The results from this study showed that the process parameters used are sufficient as there were low porosity, sufficient overlap between melt pools, acceptable residual stresses and satisfactory results from mechanical testing. However, it is recommended to perform

additional fatigue, toughness and tensile testing and density measurements to ensure the structural integrity of the material processed by SLM.

Conclusion

From this investigation of the SLMed AlSi10Mg alloy, the following conclusion may be drawn:

- After heat treatment, the fibrous Si network was dissolved and larger Si particles formed. As a result of this change in microstructure, there was a significant reduction in hardness. The heat treated specimens showed approximately half of the hardness ($\sim 68HV_{0.2}$) compared to the as-printed specimens ($\sim 131HV_{0.2}$). The vertically printed specimen exhibited a hardness number as a function of the build height and had higher hardness numbers compared to the horizontally built specimen. After heat treatment the difference in hardness from building directions were removed.

- The cells with primary α-Al had higher Al content and lowered Si content compared to the cell boundaries in the as-printed specimens. The heat treated specimens had primary α-Al matrix dispersed with Si particles. No signs of any evaporation were found.

- No signs of β'' or β' were found. However, there were indications of dislocations pinned by the equilibrium phase β, Mg_2Si, in the heat treated specimen. There were also some indications of the early stages of clusters in the as-printed specimen. Therefore, it is believed that some of the alloying elements go into solution because of the repeatedly heat cycles inherently from the SLM process.

- The stress-relief heat treatment successfully reduced the residual stresses in the specimens. The as-printed specimens were in a state of compression, and after heat treatment, they were in tension. The residual stresses were found to be well below the yield strength.

- The process parameters used for building the specimens gave an energy input per unit length much higher than what is recommended in the literature. However, the results showed that the process parameters used in this study are satisfactory as there were low porosity, sufficient overlap between melt pools, acceptable residual stresses and satisfactory results from mechanical testing.

References

[1] L. Yang, K. Hsu, B. Baughman, D. Godfrey, F. Medina, M. Menon, and S. Wiener, *Additive Manufacturing of Metals: The Technology, Materials, Design and Production (Springer Series in Advanced Manufacturing).* Springer, 2017.

[2] M. Karolus, J. Maszybrocka, A. Stwora, and G. Skrabalak, "Residual stresses of alsi10mg fabricated by selective laser melting (slm)," 2019.

[3] N. T. Aboulkhair, M. Simonelli, L. Parry, I. Ashcroft, C. Tuck, and R. Hague, "3d printing of aluminium alloys: Additive manufacturing of aluminium alloys using selective laser melting," *Progress in Materials Science*, vol. 106, p. 100578, Dec. 2019.

[4] L. Ardila, F. Garciandia, J. González-Díaz, P. Álvarez, A. Echeverria, M. Petite, R. Deffley, and J. Ochoa, "Effect of IN718 recycled powder reuse on properties of parts manufactured by means of selective laser melting," *Physics Procedia*, vol. 56, pp. 99–107, 2014.

[5] L. Hieu, E. Bohez, J. V. Sloten, H. Phien, E. Vatcharaporn, P. Binh, P. An, and P. Oris, "Design for medical rapid prototyping of cranioplasty implants," *Rapid Prototyping Journal*, vol. 9, pp. 175–186, Aug. 2003.

[6] B. Sanghera, S. Naique, Y. Papaharilaou, and A. Amis, "Preliminary study of rapid prototype medical models," *Rapid Prototyping Journal*, vol. 7, pp. 275–284, Dec. 2001.

[7] K. Kempen, L. Thijs, J. V. Humbeeck, and J.-P. Kruth, "Processing AlSi10mg by selective laser melting: parameter optimisation and material characterisation," *Materials Science and Technology*, vol. 31, pp. 917–923, Nov. 2014.

[8] N. T. Aboulkhair, N. M. Everitt, I. Ashcroft, and C. Tuck, "Reducing porosity in AlSi10mg parts processed by selective laser melting," *Additive Manufacturing*, vol. 1-4, pp. 77–86, Oct. 2014.

[9] N. Read, W. Wang, K. Essa, and M. M. Attallah, "Selective laser melting of AlSi10mg alloy: Process optimisation and mechanical properties development," *Materials & Design (1980-2015)*, vol. 65, pp. 417–424, Jan. 2015.

[10] J. Wu, X. Wang, W. Wang, M. Attallah, and M. Loretto, "Microstructure and strength of selectively laser melted AlSi10mg," *Acta Materialia*, vol. 117, pp. 311–320, Sept. 2016.

[11] M. Tang and P. C. Pistorius, "Oxides, porosity and fatigue performance of AlSi10mg parts produced by selective laser melting," *International Journal of Fatigue*, vol. 94, pp. 192–201, Jan. 2017.

[12] N. T. Aboulkhair, I. Maskery, C. Tuck, I. Ashcroft, and N. M. Everitt, "The microstructure and mechanical properties of selectively laser melted AlSi10mg: The effect of a conventional t6-like heat treatment," *Materials Science and Engineering: A*, vol. 667, pp. 139–146, June 2016.

[13] I. Rosenthal, A. Stern, and N. Frage, "Microstructure and mechanical properties of AlSi10mg parts produced by the laser beam additive manufacturing (AM) technology," *Metallography, Microstructure, and Analysis*, vol. 3, pp. 448–453, Oct. 2014.

[14] L. Zhou, A. Mehta, E. Schulz, B. McWilliams, K. Cho, and Y. Sohn, "Microstructure, precipitates and hardness of selectively laser melted AlSi10mg alloy before and after heat treatment," *Materials Characterization*, vol. 143, pp. 5–17, Sept. 2018.

[15] M. Tiryakioğlu, J. Robinson, M. Salazar-Guapuriche, Y. Zhao, and P. Eason, "Hardness–strength relationships in the aluminum alloy 7010," *Materials Science and Engineering: A*, vol. 631, pp. 196–200, Apr. 2015.

[16] A. P. Sekhar, S. Nandy, K. K. Ray, and D. Das, "Hardness - yield strength relation of al-mg-si alloys," *IOP Conference Series: Materials Science and Engineering*, vol. 338, p. 012011, Mar. 2018.

[17] L. Wang, X. Jiang, Y. Zhu, Z. Ding, X. Zhu, J. Sun, and B. Yan, "Investigation of performance and residual stress generation of AlSi10mg processed by selective laser melting," *Advances in Materials Science and Engineering*, vol. 2018, pp. 1–12, 2018.

[18] A. Salmi, E. Atzeni, L. Iuliano, and M. Galati, "Experimental analysis of residual stresses on AlSi10mg parts produced by means of selective laser melting (SLM)," *Procedia CIRP*, vol. 62, pp. 458–463, 2017.

[19] B. Vrancken, R. Wauthlé, J.-P. Kruth, and J. Van Humbeeck, "Study of the influence of material properties on residual stress in selective laser melting," in *Proceedings of the solid freeform fabrication symposium*, pp. 393–407, 2013.

[20] P. Mercelis and J.-P. Kruth, "Residual stresses in selective laser sintering and selective laser melting," *Rapid Prototyping Journal*, vol. 12, pp. 254–265, Oct. 2006.

[21] C. Colombo, C. A. Biffi, J. Fiocchi, A. Tuissi, and L. Vergani, "Effect of optimized heat treatments on the tensile behavior and residual stresses of selective laser melted AlSi10mg samples," *Key Engineering Materials*, vol. 813, pp. 364–369, July 2019.

[22] E. Brandl, U. Heckenberger, V. Holzinger, and D. Buchbinder, "Additive manufactured AlSi10mg samples using selective laser melting (SLM): Microstructure, high cycle fatigue, and fracture behavior," *Materials & Design*, vol. 34, pp. 159–169, Feb. 2012.

[23] K. Kempen, L. Thijs, J. V. Humbeeck, and J.-P. Kruth, "Mechanical properties of AlSi10mg produced by selective laser melting," *Physics Procedia*, vol. 39, pp. 439–446, 2012.

[24] SLM Solutions Group AG, *Material data sheet Al-Alloy AlSi10Mg*, 2018.

[25] E. Louvis, P. Fox, and C. J. Sutcliffe, "Selective laser melting of aluminium components," *Journal of Materials Processing Technology*, vol. 211, pp. 275–284, Feb. 2011.

[26] L. Löber, S. Biamino, U. Ackelid, S. Sabbadini, P. Epicoco, P. Fino, and J. Eckert, "Comparison of selective laser and electron beam melted titanium aluminides," in *Conference paper of 22nd International symposium "Solid freeform fabrication proceedings", University of Texas, Austin*, pp. 547–556, 2011.

[27] L. Thijs, K. Kempen, J.-P. Kruth, and J. V. Humbeeck, "Fine-structured aluminium products with controllable texture by selective laser melting of pre-alloyed AlSi10mg powder," *Acta Materialia*, vol. 61, pp. 1809–1819, Mar. 2013.

[28] A. Mouritz, *Introduction to aerospace materials.* Reston, VA Cambridge, UK: American Institute of Aeronautics and Astronautics Woodhead Pub, 2012.

[29] I. Yadroitsev, A. Gusarov, I. Yadroitsava, and I. Smurov, "Single track formation in selective laser melting of metal powders," *Journal of Materials Processing Technology*, vol. 210, pp. 1624–1631, Sept. 2010.

[30] J. Sánchez-Amaya, T. Pasang, M. Amaya-Vazquez, J. Lopez-Castro, C. Churiaque, Y. Tao, and F. B. Pedemonte, "Microstructure and mechanical properties of Ti5553 butt welds performed by LBW under conduction regime," *Metals*, vol. 7, p. 269, July 2017.

[31] S. Kou, *Welding metallurgy.* Wiley-Interscience, 2nd ed ed., 2003.

[32] M. Boulos, "Powder densification and spheroidization using induction plasma technology," *Metal Powder Rep*, vol. 59, pp. 16–21, 2004.

[33] L. Wang, Y. Liu, and S. Chang, "Fabrication of spherical AlSi10mg powders by radio frequency plasma spheroidization," *Metallurgical and Materials Transactions A*, vol. 47, pp. 2444–2453, Feb. 2016.

[34] X. Zi, C. Chen, X. Wang, P. Wang, X. Zhang, and K. Zhou, "Spheroidisation of tungsten powder by radio frequency plasma for selective laser melting," *Materials Science and Technology*, vol. 34, pp. 735–742, Dec. 2017.

[35] N. T. Aboulkhair, I. Maskery, I. Ashcroft, C. Tuck, and N. M. Everitt, "The role of powder properties on the processability of aluminium alloys in selective laser melting," in *22nd World of Photonics Congress: Lasers in Manufacturing conference*, 2015.

[36] R. O'Leary, R. Setchi, P. Prickett, and G. Hankins, "An investigation into the recycling of ti-6al-4v powder used within slm to improve sustainability," *InImpact: The Journal of Innovation Impact*, vol. 8, no. 2, p. 377, 2016.

[37] T. Brown, N. Idoine, C. Wrighton, E. Raycraft, S. Hobbs, R. Shaw, P. Everett, C. Kresse, E. Deady, and T. Bide, "World mineral production 2014–18," 2020.

[38] Nærings- og fiskeridepartementet, *Nærings- og fiskeridepartementet*, 2000 (accessed March 4, 2020). https://www.regjeringen.no/no/dokumenter/norsk-naringsvirksomhet---metallindustri/id87574/.

[39] The Aluminum Association, *Primary Production*, 2020 (accessed April 5, 2020). https://www.aluminum.org/industries/production/primary-production.

[40] Henning Johansen, *Materiallære: Aluminium-kompendium*, 2012.

[41] G. Mathers, *The welding of aluminium and its alloys*. Boca Raton, Fla. Cambridge, England: CRC Press Woodhead Pub, 2002.

[42] *ASM Handbook: Properties and Selection: Nonferrous Alloys and Special-Purpose Materials*, vol. 2. ASM International, 1990.

[43] M. Tiryakioğlu, "The effect of hydrogen on pore formation in aluminum alloy castings: Myth versus reality," *Metals*, vol. 10, p. 368, Mar. 2020.

[44] C. Weingarten, D. Buchbinder, N. Pirch, W. Meiners, K. Wissenbach, and R. Poprawe, "Formation and reduction of hydrogen porosity during selective laser melting of AlSi10mg," *Journal of Materials Processing Technology*, vol. 221, pp. 112–120, July 2015.

[45] H.-S. Park and D.-S. Nguyen, "Study on flaking behavior in selective laser melting process," *Procedia CIRP*, vol. 63, pp. 569–572, 2017.

[46] D. Buchbinder, W. Meiners, N. Pirch, K. Wissenbach, and J. Schrage, "Investigation on reducing distortion by preheating during manufacture of aluminum components using selective laser melting," *Journal of Laser Applications*, vol. 26, p. 012004, Feb. 2014.

[47] M. L. Montero-Sistiaga, R. Mertens, B. Vrancken, X. Wang, B. V. Hooreweder, J.-P. Kruth, and J. V. Humbeeck, "Changing the alloy composition of al7075 for better processability by selective laser melting," *Journal of Materials Processing Technology*, vol. 238, pp. 437–445, Dec. 2016.

[48] N. Kaufmann, M. Imran, T. Wischeropp, C. Emmelmann, S. Siddique, and F. Walther, "Influence of process parameters on the quality of aluminium alloy EN AW 7075 using selective laser melting (SLM)," *Physics Procedia*, vol. 83, pp. 918–926, 2016.

[49] W. Callister, *Materials science and engineering : an introduction*. Hoboken, NJ: John Wiley & Sons, 2010.

[50] R. E. Smallman, *Physical metallurgy and advanced materials*. Amsterdam Boston: Butterworth Heinemann, 2007.

[51] NASA., *Proceedings of AF-SD/Industry/NASA Conference and Workshops on Mission Assurance: Hyatt House-Airport*, June 1983.

[52] A. Mohamed and F. Samuel, ""a review on the heat treatment of al-si-cu/mg casting alloys", in heat treatment - conventional and novel applications, f. czerwinski, ed," *Intech*, pp. 54–72, 01 2012.

[53] D. Maisonnette, M. Suery, D. Nelias, P. Chaudet, and T. Epicier, "Effects of heat treatments on the microstructure and mechanical properties of a 6061 aluminium alloy," *Materials Science and Engineering: A*, vol. 528, pp. 2718–2724, Mar. 2011.

[54] O. R. Myhr, Ø. Grong, and K. O. Pedersen, "A combined precipitation, yield strength, and work hardening model for al-mg-si alloys," *Metallurgical and Materials Transactions A*, vol. 41, pp. 2276–2289, June 2010.

[55] G. Edwards, K. Stiller, G. Dunlop, and M. Couper, "The precipitation sequence in al–mg–si alloys," *Acta materialia*, vol. 46, no. 11, pp. 3893–3904, 1998.

[56] S. Andersen, H. Zandbergen, J. Jansen, C. Traeholt, U. Tundal, and O. Reiso, "The crystal structure of the β phase in al–mg–si alloys," *Acta Materialia*, vol. 46, no. 9, pp. 3283–3298, 1998.

[57] T. H. Courtney, *Mechanical behavior of materials*. Waveland Press, 2005.

[58] The Welding Institute, *What is residual stress?*, (accessed: 28.03.2020). https://www.twi-global.com/technical-knowledge/faqs/residual-stress.

[59] Stress Map, *X-ray diffraction for residual stress measurement*, 2020 (accessed May 19, 2020). https://www.stressmap.co.uk/x-ray-diffraction-for-measuring-residual-stress/.

[60] University College, London (UCL), *Crystallite Size and Strain*, 2004 (accessed April 28, 2020). http://pd.chem.ucl.ac.uk/pdnn/peaks/size.htm.

[61] D. Nath, F. Singh, and R. Das, "X-ray diffraction analysis by williamson-hall, halder-wagner and size-strain plot methods of CdSe nanoparticles- a comparative study," *Materials Chemistry and Physics*, vol. 239, p. 122021, Jan. 2020.

[62] F. Izumi, T. Ikeda, *et al.*, "Implementation of the williamson-hall and halder-wagner methods into rietan-fp," 2015.

[63] Tekna Advanced Materials Inc., *Safety Data Sheet AlSi10Mg*, Jan. 2020. Rev. 2.1.0.

[64] A. H. Maamoun, M. Elbestawi, G. K. Dosbaeva, and S. C. Veldhuis, "Thermal post-processing of AlSi10mg parts produced by selective laser melting using recycled powder," *Additive Manufacturing*, vol. 21, pp. 234–247, May 2018.

[65] X. Liu, C. Zhao, X. Zhou, Z. Shen, and W. Liu, "Microstructure of selective laser melted AlSi10mg alloy," *Materials & Design*, vol. 168, p. 107677, Apr. 2019.

[66] A. Hadadzadeh, B. S. Amirkhiz, and M. Mohammadi, "Contribution of mg2si precipitates to the strength of direct metal laser sintered AlSi10mg," *Materials Science and Engineering: A*, vol. 739, pp. 295–300, Jan. 2019.

[67] R. Lumley, *Fundamentals of aluminium metallurgy: recent advances*. Woodhead Publishing, 2018.

[68] K. Tosha, "Influence of residual stresses on the hardness number in the affected layer produced by shot peening," in *2nd Asia-Pacific Forum on Precision Surface Finishing and Deburring Technik, Seoul*, pp. 48–54, 2002.

[69] A. Iturrioz, E. Gil, M. M. Petite, F. Garciandia, A. M. Mancisidor, and M. S. Sebastian, "Selective laser melting of AlSi10mg alloy: influence of heat treatment condition on mechanical properties and microstructure," *Welding in the World*, vol. 62, pp. 885–892, Apr. 2018.